Universiteit Antwerpen

Master thesis 2015-2016

Optical transport in the SoLi∂ detector

Author:
Maja Verstraeten

Promotor:
Prof. Dr. Nick Van Remortel

Thesis in order to obtain the degree of Master in Science

in the

Department of Physics
High Energy Physics

May 23, 2016

University of Antwerp

Abstract

Department of Physics, High Energy Physics

Master of Science in Physics
Maja Verstraeten

The SoLi∂-detector is a compact and highly segmented neutrino detector with a suitable position -and energy resolution. It will be installed at very close proximity (5-10m) to the core of the BR2 research reactor of the SCK·CEN research center in Mol. With accurate measurements of the $\bar{\nu}_e$-flux, it will investigate the reactor neutrino anomaly within the framework of neutrino oscillations. This master's thesis is dedicated to the photon transport within the SoLi∂ detector. To this end, an experimental testbench is constructed and an accurate simulation is developed. The influence of the different optical components is investigated. The simulation parameters are tuned to meet the experimental results, such that the simulation can explain and enhance the experiment. It will be determined that especially the tyvek can enhance the light yield. And to reach single photon sensitivity, the interfering dark counts can only be avoided by cooling the full-scale detector down.

Universiteit Antwerpen

Nederlands Abstract (Vulgariserend)

Departement Fysica, Hoge Energie Fysica

Master in de Fysica
Maja Verstraeten

Binnen het domein van elementaire deeltes fysica, zijn neutrinos bijzonder fascinerend. Neutrinos interageren amper met materie. Ookal weten we dat ze miljoenen keren lichter moeten zijn dan het elektron, toch is hun precieze massa nog steeds onbekend. Dat ze *ü*berhaupt een massa hebben, werd slechts 15 jaar geleden ontdekt. De drie soorten van neutrinos bleken in elkaar te oscilleren, wat enkel mogelijk is indien ze massief zijn. Recente, onverwachte metingen tonen aan dat we nog niet alles begrijpen van de neutrino-oscillaties. Er lijken neutrinos te verdwijnen. Eventueel oscilleren ze in een nieuw soort neutrino, dat nog niet ontdekt is.
De SoLi∂-samenwerking zal de neutrinos onderzoeken die afkomstig zijn van de kernreactor in het SCK·CEN te Mol, Belgi*ë*. Het zal de neutrino-oscillatie onderzoeken op korte afstand van de reactor. Deze masterthesis is er op toegelegd om het transport van de fotonen in de detector te onderzoeken. Hiervoor zullen experimenten worden uitgevoerd en zal een computersimulatie worden opgesteld. De resultaten van beide worden in overeenstemming gebracht, zodat men aan de hand van de simulatie de experimentele resultaten kan interpreteren en nieuwe voorspellingen kan maken.

Preface

In retrospect of last summer, when I was still trying to understand the first neutrino papers and struggling to get the simulation running, I can only imagine how much I have learned in the past year.
During my previous physics education, I have been more involved with theoretical physics. As the end of my university education approached, I came to understand that I would rather work in the experimental field; I'm more convinced by the deductive way of working, starting from experimental observations to derive laws of nature. I'm convinced that my broad theoretic foundation allows to interpret novel observations more accurately. My desire to perform fundamental research and be involved in the analysis of observations, led me to the Soli∂ project.
In addition, we have at present such a powerful tool at our disposal, under the form of computer simulations, that I eagerly wanted to master this better. I had experience in working with matlab and I had shown to have an aptitude for programming, but I had little experience in programming with C++, let alone in the GEANT4 library. In the context of this thesis I became part of a more complex software development effort, which resulted in a steep learning curve.

I wish to express my gratitude to professor Nick Van Remortel for introducing me to the interesting world of neutrino physics. Thank you for getting me involved in the SoLi∂ experiment and for lending me the opportunity to attend the collaboration meeting of the international SoLi∂ collaboration.

With regard to the programming, I wish to thank Ibrahin Piñera who helped me find my way in the elaborate simulation. My gratitude also goes out to my colleague students Matthias Verstappen and Brent Van Bladel for patiently searching a solution when my computer, operating system and GEANT4 turned out not to be compatible.

Finally, I wish to address my gratitude to my family for lending me all of their support and faith. And special thanks to Jef Van den Bergh for his love and support.

Enjoy the reading,

Maja Verstraeten

CONTENTS

INTRODUCTION

Research groups of transnational universities have joined forces to face a persisting anomaly in neutrino physics. Three independent experiments found deviating results with respect to the known physics of elementary particles. They support the hypothesis of the existence of a new neutrino family. Nature may contain more than three neutrino mass eigenstates with mass splittings that can be significantly larger than the currently measured values of Δm^2_{21} and Δm^2_{31}. If the existence of the so called sterile neutrino would be proven, it would be a major breakthrough in both particle physics and cosmology. However, as the name suggests, the sterile neutrino is hard to probe experimentally, if it so much as exists at all.

The SoLi∂ collaboration, short for **S**earch for **O**scillations with a **Li**thium-**6** detector, is a new short-baseline neutrino experiment with as principle goal to resolve some of the short-baseline neutrino anomalies. The collaboration will perform a $\bar{\nu}_e$-oscillation measurement at close proximity to the core of the Belgian BR2 research reactor. To evade the challenging task of predicting theoretically the neutrino flux and the neutrino energy spectrum, the SoLi∂ experiment will perform an oscillometric analysis by using a position sensitive detector with a good energy resolution, sufficient detection efficiency, and with as little as possible theoretical model dependence.

A detailed simulation of the full-scale SoLi∂ experiment is required. All steps in the chain of the production-, interaction- and detection of the neutrinos have to be modelled accurately. For my master's thesis, I am working on the simulation of the optical processes, using the GEANT4 library. The optical simulation has to model the propagation of photons, that originate in the scintillation process of PVT cubes and are transported through WLS fibers to the detection mechanism. Ultimately, the simulation must be able to reproduce the experimental results for the basic setup. The simulation then allows to interpret the experimental outcome in the context of the optical processes within the different components of the setup.

The contents of this thesis are structured in several chapters.
Chapter 1 is devoted to the history of neutrino physics. This chapter sets out the main discoveries about neutrinos, based on the corresponding papers. Special interest goes out to the neutrino oscillations. The different neutrino detectors will be discussed as well.
Chapter 2 focuses on the SoLi∂ detector. The detector's working principle to investigate neutrino oscillations will be covered, as well as the obstacles it has to face. The optical components of the SoLi∂ detector will be discussed in detail in chapter 3.
Chapter 4 describes the experimental measurements and analysis.

Different properties for the optical components will be tested to obtain an optimal light yield for the final SoLi∂ detector.
Chapter 5 will specify the optical simulation. The different parameters that are incorporated in the simulation, will be studied for their influence on the light yield. Thereafter, these parameters will be tuned such that the simulation meets the experimental results. This will be done methodologically with the information that can be extracted from the experiments.

Finally, I would like to point out that the size of the text body is intentionally shaped like it is. It supports both legibility and allows a reasonable amount of information to be on a page. I hope you enjoy the reading.

1 INTRODUCTION ON NEUTRINOS

1.1 NEUTRINOS IN THE STANDARD MODEL

Neutrinos are as mysterious as they are abundant; billions of them are passing harmlessly through every inch of the earth's surface right now. However, neutrinos pass through most matter unnoticed, travelling through our globe without a single collision. Neutrinos interact only via the weak force, which leaves them hard to detect experimentally and makes them the least understood particles of the Standard Model (SM) of Particle Physics. For example, neutrinos have extremely low masses,[1] and the origin of this mass has, most probably, a different connection with the Brout-Englert-Higgs mechanism than the other SM particles.[2] Despite enormous experimental progress, the nature and the fundamental properties of neutrinos remain unknown: possible CP violation, absolute mass scale, mass hierarchy, other flavors...

The neutrino was first proposed by Wolfgang Pauli in 1930 to solve a tremendous problem regarding nuclear beta decay.[3] A radioactive nucleus can emit an electron (a beta ray) and decrease its positive charge by one unit to become the nucleus of another element. In 1914 James Chadwick showed that the electrons, that are emitted in beta decay, are distributed over a continuous spectrum of energies,[4] see figure 1.1 left. When the electron energy was not at its maximum, the energies before and after the reaction were different. Some of the energy released in the decay process was lost, putting the esteemed law of energy conservation on the verge. Pauli's solution to the problem was that a yet-to-be-discovered particle carried away the missing energy. The particle should be an electrically neutral, spin 1/2-fermion with a mass no larger than that of the electron.

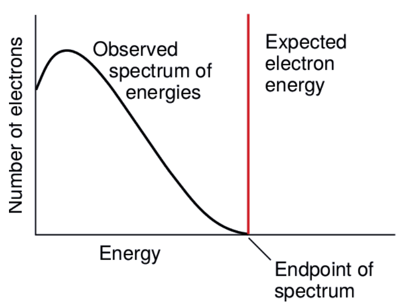

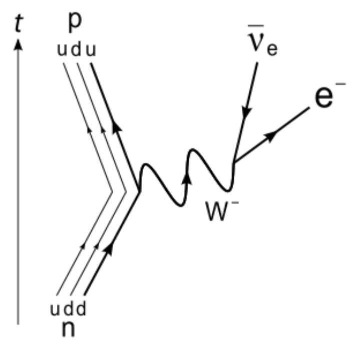

Figure 1.1: Left: Expected and observed energy spectrum of electrons emitted in beta decay. Image: Los Alamos Science.
Right: Beta decay of a proton, including the new particle $\bar{\nu}_e$. Image: public domain.

Four years later Enrico Fermi formulated a brilliant theory that included the neutrino.[5] In this weak theory, the beta decay is an interaction between two currents that carry a weak charge. A W^- boson exchanges a negative weak charge between the currents, converting the down quark into an up quark and the electron in an anti electron neutrino, $\bar{\nu}_e$. See figure 1.1 on the right.

As soon as Fermi had proposed his theory, it became clear that neutrinos would be nearly impossible to detect. Due to the large mass of the W boson (approximately 90 GeV/c^2) [6] these carrier particles are very short-lived. They have a lifetime of under 10^{-24} seconds and their range is only around $10^{-17} - 10^{-16}$ m. Moreover, the weak boson has a low interaction strength. Its coupling constant is between 10^{-7} and 10^{-6}, which is weak in comparison with the strong interaction coupling constant of 1 and the electromagnetic coupling constant of $\sim 10^{-2}$.[7] Consequently, the probability for a detectable interaction of neutrinos with matter is close to zero.
But in 1956 Fred Reines and Clyde Cowan succeeded in establishing the neutrino experimentally at the Savannah River nuclear reactor in South Carolina. They achieved to detect anti neutrinos that were produced in the reactor, by observing the products of the inverse beta decay that the anti neutrino induced in the detector medium (more on this decay later, in section 2.2 on page 25).[8] This was the long awaited unambiguous proof of the existence of the neutrino.

The neutrinos were incorporated in the Standard Model of particle physics from Glashow, Weinberg and Salam in the 1970s . Neutrinos come in three flavours (ν_e, ν_μ, ν_τ), which are linked to their leptonic partners (electron e, muon μ and tauon τ) via the weak nuclear force (see figure 1.2).

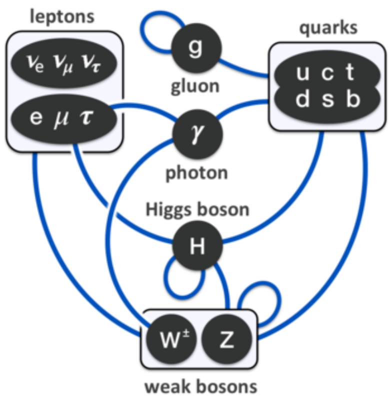

Figure 1.2: Diagram summarizing the interactions between elementary particles according to the Standard Model. Vertices represent types of particles, edges represent interactions between them. Multiple generations of types of particles share an oval. Image: Eric Drexler

The neutrinos ν have corresponding antimatter particles, which have the same mass but the opposite charge: the anti neutrinos $\bar{\nu}$. As opposed to electrons and positrons, neutrinos carry no electric charge, so a new quantum number was introduced to make the distinction.[11] Particles like e, μ and ν possess a lepton number $L = +1$, whereas their antiparticles e^+,μ^+ and $\bar{\nu}$ have $L = -1$. All other particles have $L = 0$.

The Standard Model further incorporates the fact that weak interactions violate parity by only allowing left-handed neutrinos (and right-handed anti-neutrinos) to participate in weak interactions. The handedness (chirality) of the neutrino is consistent with the measured neutrino helicity, $h = 1$, within the experimental uncertainties, as expected for a massless particle.[12]

The Standard Model of particle physics has proven to be an extremely successful description of matter, forces and its interactions. The predictions of the Standard Model have been verified in precision experiments, most notably at the Large Electron Positron Collider LEP at CERN. Based on the measurement of the invisible Z^0 width, these experiments established the number of light neutrinos to be three - consistent with the effective number of relativistic degrees of freedom determined in cosmology.[13]

In the last few decades, several experimental results have established that neutrinos oscillate from one flavor to another. This surprising fact represents a revolution in physics - the first known particle interactions that indicate physics beyond the extremely successful Standard Model. The oscillation mechanism gives indirect evidence that neutrinos have a non-zero mass, since the frequency of the oscillations depends on the mass difference among the neutrino types. This was not included as part of the original Standard Model.[9] [10]

Neutrino physics has entered an era of precision measurements of the oscillation parameters. But, as the picture becomes clearer, a subset of the oscillation data from different experiments seems to deviate from the simplest hypothesis of the oscillation between three neutrino flavors. Recently, three independent anomalies (LSND/MiniBooNE-, Gallium- and reactor anomaly) support the hypothesis of the existence of a new neutrino family. These neutrinos are called sterile because they do not interact via the known forces.

1.2 Neutrino oscillations

1.2.1 *The solar neutrino problem*

The Sun is a natural, nuclear fusion reactor. In the process to convert hydrogen nuclei into helium, loads of neutrinos, positrons and energy are created. The neutrinos travel from the Sun's core to the Earth's

surface without any significant absorption by the Sun's outer layers. As neutrino detectors became sensitive enough to measure the flow of neutrinos from the Sun, it became clear that the number detected was lower than that predicted by models of the solar interior.[14] In various experiments, the number of detected neutrinos was between one third and one half of the predicted number. This came to be known as the solar neutrino problem.
According to the Standard Model, as stated in the 1970s, neutrinos should be massless. This implies that the type of neutrino is fixed upon production. The Sun should emit only electron neutrinos, since they are produced in the fusion cycle.
A possible solution to the solar neutrino problem came from Bruno Pontecorvo. Already in 1957, he suggested that the neutrinos oscillate into different states along their journey to the earth.[15] These neutrino oscillations could explain the anomalously low neutrino detection rate but it would also require neutrinos to have mass.

1.2.2 *Neutrino eigenstates and the PMNS matrix*

The neutrino flavors that are detected experimentally are the *flavor*-eigenstates of the neutrino, namely ν_e, ν_μ and ν_τ.[16] [17] These three eigenstates of the weak interaction form a complete, orthonormal basis for the Standard Model neutrino. The flavor-eigenstates are superpositions of the *mass*-eigenstates of the neutrino, ν_1, ν_2 and ν_3. Similarly, one can construct an eigenbasis out of these states of definite mass. This basis will diagonalize the neutrino's free-particle Hamiltonian. The unitary transformation between the two eigenstates is given by

$$\begin{pmatrix} \nu_e \\ \nu_\mu \\ \nu_\tau \end{pmatrix} = \begin{pmatrix} U_{e1} & U_{e2} & U_{e3} \\ U_{\mu 1} & U_{\mu 2} & U_{\mu 3} \\ U_{\tau 1} & U_{\tau 2} & U_{\tau 3} \end{pmatrix} \begin{pmatrix} \nu_1 \\ \nu_2 \\ \nu_3 \end{pmatrix}, \tag{1.1}$$

where each ν_a, $a \in \{e, \mu, \tau\}$ and each ν_i, $i \in \{1, 2, 3\}$ is a multi-component object (whether it is a Dirac-, Weyl- or Majorana fermion is still to be determined). A neutrino of a given flavor a is thus a "mixed" state of neutrinos with different mass. In Einstein-summation convention we can write this as

$$|\nu_a\rangle = U_{ai} |\nu_i\rangle . \tag{1.2}$$

In general, the matrix U_{ai} is a $n \times n$, unitary matrix. It is called the Pontecorvo-Maki-Nakagawa-Sakata (PMNS) matrix to honor the pioneers whose work resulted in the discovery of neutrino oscillations. The unitarity of the matrix preserves the total probability to be one; the PMNS matrix appears as a factor in the time evolution operation for neutrino mixing, and the neutrino must definitely be in one of the possible states. In the case of three neutrino flavors, the PMNS matrix becomes (with $c_{ij} = \cos\theta_{ij}$ and $s_{ij} = \sin\theta_{ij}$),

$$U = \begin{pmatrix} 1 & 0 & 0 \\ 0 & c_{23} & s_{23} \\ 0 & -s_{23} & c_{23} \end{pmatrix} \begin{pmatrix} c_{13} & 0 & s_{13}e^{-i\delta} \\ 0 & 1 & 0 \\ -s_{13}e^{i\delta} & 0 & c_{13} \end{pmatrix} \begin{pmatrix} c_{12} & s_{12} & 0 \\ -s_{12} & c_{12} & 0 \\ 0 & 0 & 1 \end{pmatrix} \begin{pmatrix} e^{\frac{i\alpha_1}{2}} & 0 & 0 \\ 0 & e^{\frac{i\alpha_2}{2}} & 0 \\ 0 & 0 & 1 \end{pmatrix}. \tag{1.3}$$

This matrix has four degrees of freedom (there are 9 degrees of freedom for a 3×3 matrix but the squares of rows and collumns must equal 1 to render complete probabilities). In the standard parametrization, which is used in equation 1.3, there are three mixing angles θ_{ij} and a phase δ, which is related to charge-parity violations. In case the neutrinos are Majorana fermions, two extra complex phases, α_1 and α_2 are needed, since the phase of the Majorana fields cannot be redefined freely due to the constraint of the reality-condition that Majorana spinors are subject to.
If experiments show that this 3×3 matrix is not unitary, a sterile neutrino or some other new physics is required.

1.2.3 *The oscillation mechanism*

The mass-eigenstates of the neutrino, $|\nu_i\rangle$, form an orthonormal eigenbasis that diagonalises the neutrino's free-particle Hamiltonian.[18] The eigenstates have definite energies $E_i = \sqrt{p^2 + m_i^2}$ corresponding to slightly different masses m_i. The propagation of the mass-eigenstates can be described by plane wave solutions of the form

$$|\nu_i(t)\rangle = e^{-iE_i t} |\nu_i(0)\rangle \tag{1.4}$$

where t is the time from the start of the propagation. The quantities are expressed in natural units ($c = 1$, $\hbar = 1$). For a general state $\psi(t)$, that is a superposition of eigenstates, we get

$$\psi(t) = \sum_i c_i |\nu_i(t)\rangle = \sum_i c_i e^{-iE_i t} |\nu_i(0)\rangle . \tag{1.5}$$

Mass-eigenstates with different masses propagate at different speeds. Since the flavor-eigenstates are combinations of mass-eigenstates, this difference in speed causes interference between the corresponding flavor components (see figure 1.3). Constructive interference makes it possible to observe a neutrino, created with a given flavor, to change its flavor during its propagation. The probability that a neutrino originally of flavor a will later be observed as having flavor b is

$$P_{a\to b} = |\langle \nu_b | \nu_a(t) \rangle|^2 = \left| \sum_i U_{ai}^* U_{bi} e^{-iE_i t} \right|^2 . \tag{1.6}$$

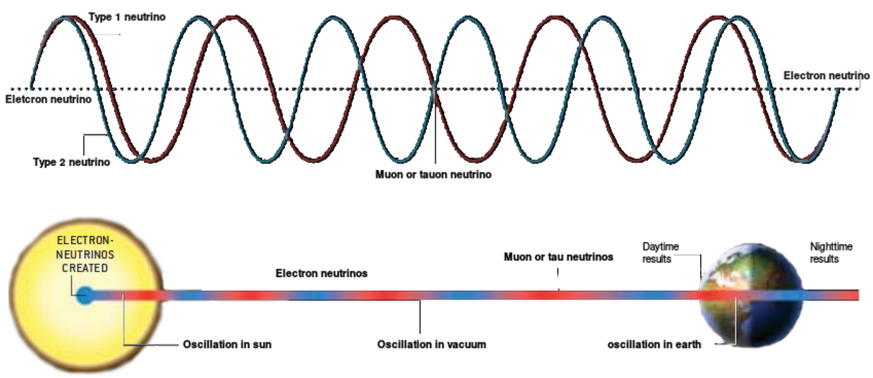

Figure 1.3: oscillations of solar electron neutrinos in the neutrino mass basis. The oscillation is dependent on the phase parameters such as the mass difference and mixing angle. Image: SNO collaboration.[20]

Let's calculate this in the case $n = 2$ with two possible flavor-eigenstates, say e and μ. Written as superpositions of mass-eigenstates on time $t = 0$, the neutrinos are

$$\begin{aligned} |\nu_e\rangle &= \quad \cos\theta\,|\nu_1\rangle + \sin\theta\,|\nu_2\rangle & (1.7) \\ |\nu_\mu\rangle &= -\sin\theta\,|\nu_1\rangle + \cos\theta\,|\nu_2\rangle\,. & (1.8) \end{aligned}$$

After a time t, the electron neutrino will be evolved into the state

$$|\nu_e, t\rangle = \cos\theta e^{-iE_1 t}\,|\nu_1\rangle + \sin\theta e^{-iE_2 t}\,|\nu_2\rangle\,. \tag{1.9}$$

Filling in the reverse relations

$$\begin{aligned} |\nu_1\rangle &= \cos\theta\,|\nu_e\rangle - \sin\theta\,|\nu_\mu\rangle & (1.10) \\ |\nu_2\rangle &= \sin\theta\,|\nu_e\rangle + \cos\theta\,|\nu_\mu\rangle\,, & (1.11) \end{aligned}$$

the evolved electron neutrino is

$$|\nu_e, t\rangle = (\cos^2\theta e^{-iE_1 t} + \sin^2\theta e^{-iE_2 t})\,|\nu_e\rangle + \cos\theta\sin\theta(e^{-iE_2 t} - e^{-iE_1 t})\,|\nu_\mu\rangle\,. \tag{1.12}$$

When this neutrino is detected after time t, it will be found in one of its flavor-eigenstates. The probability to find it in the μ flavor state is

$$\begin{aligned} P_{\nu_e\to\nu_\mu} &= \left|\langle\nu_\mu|\nu_e(t)\rangle\right|^2 = \left|\cos\theta\sin\theta(e^{-iE_2 t} - e^{-iE_1 t})\right|^2 & (1.13) \\ &= \cos\theta^2\sin\theta^2\left(2 - e^{-i(E_2-E_1)t} - e^{-i(E_1-E_2)t}\right) & (1.14) \\ &= \frac{1}{2}\sin(2\theta)^2(1 - \cos((E_2 - E_1)t)) & (1.15) \\ &= \sin(2\theta)^2\sin\left(\frac{E2 - E1}{2}t\right)^2 & (1.16) \end{aligned}$$

Where we have used some goniometric equalities. Since for the neutrino $m_\nu \ll \vec{p}_\nu$ its energy can be approximated by $E_i = \sqrt{p^2 + m_i^2} \approx p_i + \frac{m_i^2}{2p_i}$, such that

$$E_2 - E_1 = \frac{1}{2}\frac{m_2^2 - m_1^2}{|\vec{p}|} \approx \frac{1}{2}\frac{m_2^2 - m_1^2}{E}. \tag{1.17}$$

Using this approximation and the fact that $t = L$ in natural units for a particle that travels near the speed of light, the probability becomes

$$P_{\nu_e\to\nu_\mu} = \sin(2\theta)^2\sin\left(\frac{m_2^2 - m_1^2}{4E}L\right)^2. \tag{1.18}$$

Restoring SI units

$$\begin{aligned} P_{\nu_e\to\nu_\mu} &= \sin^2(2\theta)\sin^2\left(\frac{\Delta m^2\,c^3\,L}{4\hbar E}\right) & (1.19) \\ &\approx sin^2(2\theta)\sin^2\left(1.27 \times \frac{\Delta m^2}{\mathrm{eV}^2}\frac{L}{\mathrm{km}}\frac{\mathrm{GeV}}{E}\right). & (1.20) \end{aligned}$$

The phase that is responsible for the oscillation includes the following oscillation parameters:
– The mass differences, Δm^2
– The oscillation length, L
– The neutrino energies, E

For a specific mass squared difference, the **electron** anti-neutrinos survival probability is maximal at the distances L for which the following holds,

$$\frac{\Delta m^2 L}{4E} = n\pi, \tag{1.21}$$

with $n \in \mathbb{N}$. Therefore, the number of $\bar{\nu}_e$ oscillates over the travelled distance L. By tuning the oscillation length and the neutrino energies, experimentalists can gain information on the mass differences and the mixing angles between the neutrino flavors.

For a neutrino with a typical energy of 1 GeV and a mass squared difference of $\Delta m^2 = (0,05eV)^2$, the wavelength of the oscillation can be calculated as

$$L = \frac{4\pi\ 10^9}{0,05^2}\ \frac{eV}{eV^2} \quad \approx 5,024.\ 10^2\ \frac{\hbar c}{eV} \tag{1.22}$$

$$= 991\ 370\ m \quad \approx 1000\ km, \tag{1.23}$$

where SI-units have been restored using

$$\frac{\hbar c}{eV} = 1,97327.\ 10^{-7} m. \tag{1.24}$$

The oscillation mechanism would imply directly that some of the neutrinos are massive; without mass differences between the neutrinos, the driving phase of the oscillation would become zero. Nevertheless, it is not ruled out that one of the neutrinos is indeed massless. The mechanism which generates neutrino masses is still unknown, and the Standard Model must be extended for this 'new physics'. This might be Majorana fermions (i.e. particles that are their own anti-particles) and the see-saw mechanism or heavy sterile neutrinos or additional Higgs particles - none of which has so far been observed.

That neutrinos are massive, would have pervasive implications for the handedness of neutrinos. Experimental results show, within the margin of error, that all produced and observed neutrinos have left-handed helicities (spins antiparallel to momenta), and all antineutrinos have right-handed helicities (spins parallel to momenta) (see section 1.1. In the massless limit, this means that only one of two possible chiralities is observed for the particles (chirality is a fundamental property of particles and is relativistic invariant: it is the same regardless of the particle's speed and mass in every reference frame). These are the only helicities and chiralities that are included in the Standard Model of particle interactions.
In the case that neutrinos are massive, they do not move at the speed of light. It is possible for an observer to move faster than the neutrino and detect an opposite helicity. This leaves the possibility for neutrinos to have a right-handed helicity and antineutrinos to have a left-handed helicity. The question thus remains whether right-handed neutrinos and left-handed antineutrinos exist as separate particles.

1.2.4 *Detection of neutrino oscillations*

It was only around the turn of the millennium that two convincing discoveries validated the actual existence of neutrino oscillations. in 1998, the Super-Kamiokande Collaboration presented data showing the disappearance of atmospheric muon-neutrinos, that are produced in the upper atmosphere by cosmic rays, as they travel from their point of creation to the detector.[19]

In 2001, the Sudbury Neutrino Observatory (SNO) Collaboration showed clear evidence for conversion of solar electron-neutrinos into muon- or tau-neutrinos.[20] After extensive statistical analysis, it was found that about 35% of the arriving solar neutrinos are electron-neutrinos. The others being muon- or tau-neutrinos. The total number of detected neutrinos agreed quite well with the earlier predictions on the fusion reactions inside the Sun. The limits that they found for the oscillation parameters are presented in figure 1.4.

These discoveries are of fundamental importance and constitute a major breakthrough. Neutrino oscillations and the connected issues of the nature of the neutrino, neutrino masses and possible CP violation among leptons are today major research topics in particle physics.

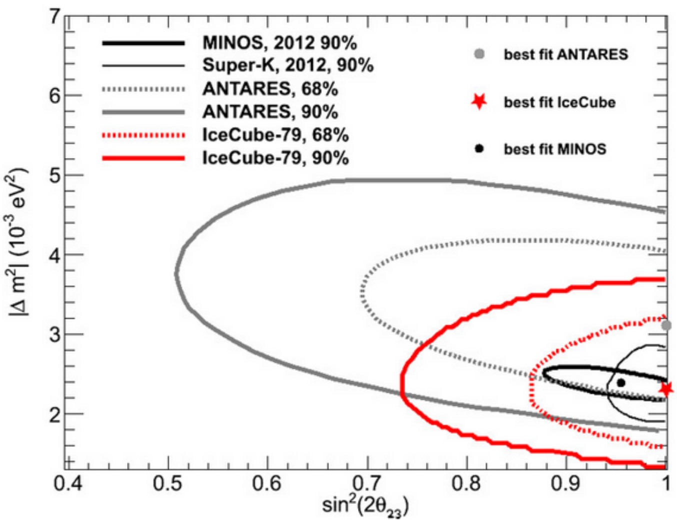

Figure 1.4: Significance contours for the IceCube+DeepCore atmospheric neutrino oscillation analysis, compared with the results of ANTARES, MINOS and SuperKamiokande. Image: IceCube Collaboration.[21]

1.3 DETECTING NEUTRINOS

1.3.1 *The cross section of neutrino interactions*

The Weak interaction is called weak for good reason. Neutrinos are the only Standard Model fermions to interact solely via the weak interaction, making them challenging to probe. In order to detect a neutrino signal, the neutrino must engage in an interaction with a substantial cross section within the detector medium. The number of neutrino interactions expected to be collected is

$$N_\nu(E) \sim \Phi_\nu(E) \times \sigma_\nu(E) \times target, \tag{1.25}$$

with $\Phi_\nu(E)$ the neutrino flux, dependent on the source, $\sigma_\nu(E)$ the cross section that represents the probability for the neutrino to interact, and with *target* the number of target particles that the neutrino can interact with. The target and the flux can be chosen to be large by operating enormous detectors in the path of solar-, cosmic- or reactor neutrinos. That leaves the neutrino cross section to determine the interaction rate.

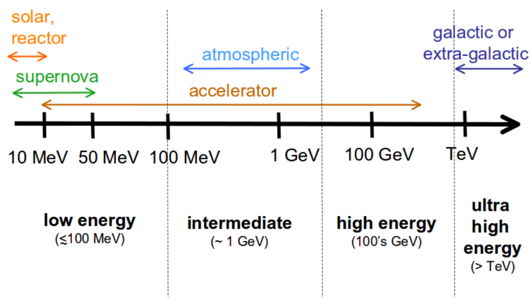

Figure 1.5: Energy range of neutrinos with different origins. Image: Los Alamos, Sam Zeller

The neutrino cross section is dependent on the energy of the neutrino, which varies over a broad spectrum for neutrinos of different origin (see figure 1.5). It is important to know which interaction is dominant for a neutrino experiment that operates in a specific energy range.
Neutrino interactions fall in two classes, namely charged current- and neutral current interactions.[22] In the former case, a $W^{\pm}$boson mediates a charge between the reaction products (see figure 1.6 left). Charge conservation requires that a charged lepton exits the interaction. The flavor of the outgoing lepton tags the flavor of the incoming neutrino.

Figure 1.6: example of neutrino interactions with a charged- and a neutral current respectively. Image: open domain.

In the case of a neutral current interaction, a neutral Z^0 boson is emitted (see figure 1.6 right). The neutrino cannot change its flavor and will exit the interaction. If there is no energy transfer, the interaction is *elastic*. Otherwise, the reaction is called *inelastic*. The charged-current-analogue of an inelastic interaction is called *quasi-elastic* scattering: the exchange of the W causes the incoming lepton and the target to change flavors, but the target does not go into an excited state or break apart. *Deep Inelastic Scattering* (DIS) is the case where there is very large 4-momentum exchange. Finally, *Single pion production* occurs when the target becomes a resonance (RES) which decays into a pion.
The total neutrino cross section is dominated by different interactions for different energy ranges (see fig 1.7).[23] In the low energy range ($E_\nu < 100 MeV$), the cross section is rising rapidly, dominated by Quasi-elastic scattering (QE). The inverse beta decay process, $\bar{\nu}_e p \rightarrow e^+ n$, is an example of such a scattering. This process was observed by Reines and Cowan as they first detected a neutrino signal (see section 1.1). The SoLi∂ detector, which is the center topic of this essay, probes this specific channel (see chapter 2).

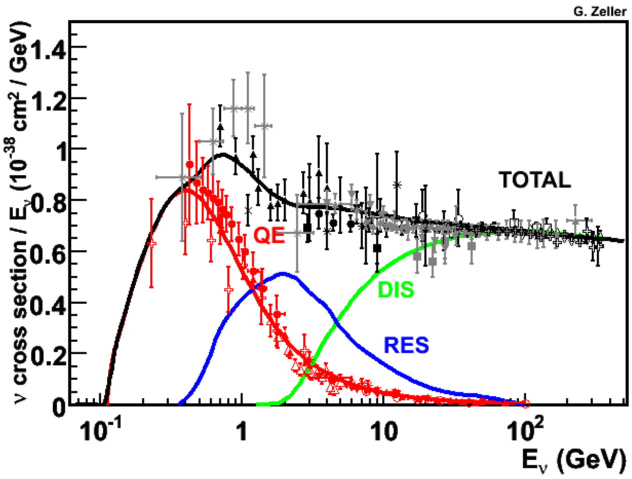

Figure 1.7: Neutrino cross sections for different interactions over a broad energy range. Image: J. Formaggio and G. Zeller, Rev. Mod. Phys.[23]

The cross section for quasi-elastic scattering is given by

$$d\sigma = \frac{G_F^2 \cos^2\theta_c}{2} 2\pi L^{\mu\nu} W_{\mu\nu} \frac{d^3k}{(2\pi)^3}, \tag{1.26}$$

with G_F the Fermi constant, θ_C the Cabibbo angle, $L^{\mu\nu}$ leptonic structure functions and $W_{\mu\nu}$ hadronic structure functions. This cross section can be accurately computed with an uncertainty of less than 0.5% for low energies. However, measurements show that the σ_{QE} is very small - around $10^{-41}cm^2$ (see figure 1.8 - The top line represents the σ_{IBD}).

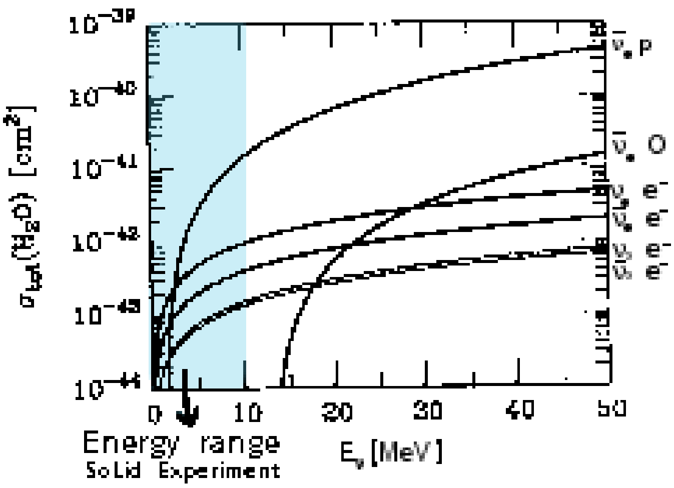

Figure 1.8: neutrino cross section for Quasi-elastic scattering, in the low energy range. Image: K. Zuber,Neutrino Physics, IOP

Another energy range encloses the intermediate energies that lie around $\sim 1 GeV$. In this range, the total cross section gets more complicated as multiple processes contribute. The Quasi-elastic process becomes less important (and its σ_{QE} becomes more complicated as nuclear effects and the Q^2-dependence of the formfactor have to be taken into account). If the neutrino has enough energy, it can excite the nucleon to a baryonic resonance, leading to a single pion production (RES). This process is an important background for oscillation experiments. The cross section at intermediate energies is typically only known to $20-40\%$. However, this is an important regime, as many experiments like MiniBooNE, SciBooNE, MINOS and MINERνA operate in this range.

At high energies of $100'sGeV$, we enter the deep inelastic scattering (DIS) regime. Whereas for QE the nucleon stayed intact, and for RES the nucleon went to an excited state, for DIS the nucleon breaks up in fragments. This results in hadronic showers (See figure 1.9, left).

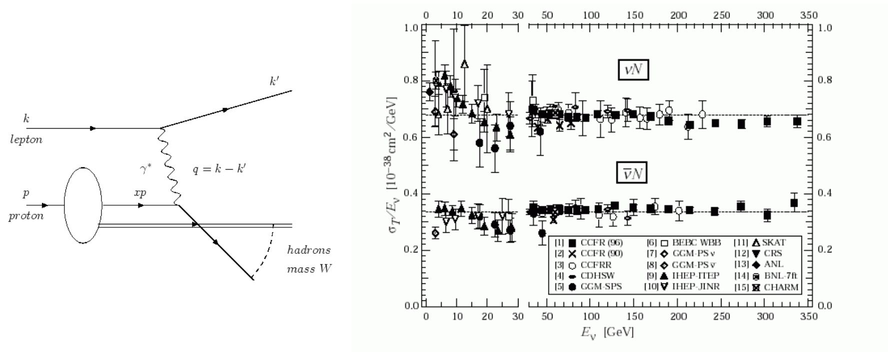

Figure 1.9: Left: Deep Inelastic Scattering of a lepton on a hadron, at leading order in perturbative expansion. Image: public domain. Right: Measured ν_μ and $\bar{\nu}_\mu$ total cross sections as a function of neutrino energy. Image: K. Hagiwara et al., Phys. Rev. D 66

The DIS cross section is written in its simplest form as

$$\frac{d^2\sigma_{\nu,\bar{\nu}}}{dx\,dy} = \frac{G_F^2 y}{16\pi}\frac{1}{(1+Q^2/M_{W,Z}^2)^2} L_{\mu\nu}W^{\mu\nu}, \tag{1.27}$$

with in the second factor the vector boson propagator and in the last factor the structure functions. The total σ_{DIS}, including nuclear effects, has been measured to 2% accuracy (see figure 1.9, right).

We conclude that neutrino cross sections are small over a wide energy range. Multiple processes contribute to it. The knowledge of the σ_ν is critical to determine the rate of interactions to expect and what the interaction will look like in its final state.

With regard to the SoLi∂ experiment, in the scope of which this thesis is written, the neutrinos under investigation are originated from a fission reactor. The energy spectrum of the $\bar{\nu}_e$-flux from the fission reactor is a superposition of the spectra from different fissile isotopes (see figure 1.10).[24] The neutrino energy spectrum varies in time, as ^{235}U decays into other isotopes which emit neutrinos with slightly different energies. The weights to obtain the correct superposition, depend on the initial composition of the fuel rods, the positions of the moderators in the reactor, that enhance the reaction speed, and the time. The determination of the exact spectrum is a highly specialised and, moreover, classified affair.
Nevertheless, it is apparent that the neutrino energies will fall in the low energy range of $\mathcal{O}$(MeV), where reactor neutrinos are typically situated (see

figure 1.5). The range of the SoLi∂ detector is indicated in figure 1.8. The dominant mechanism in this range is the inverse beta decay, which is indeed the channel that the experiment will investigate.

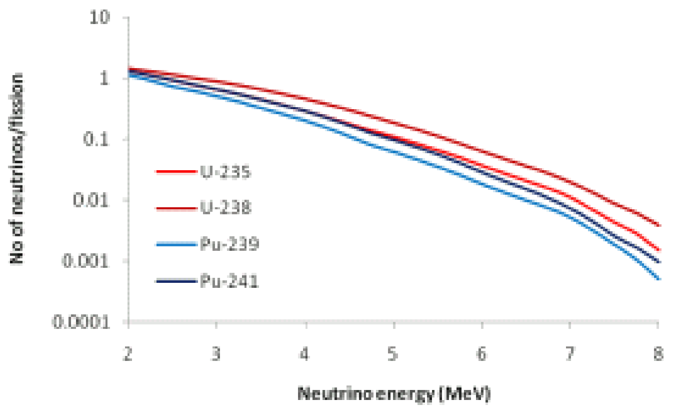

Figure 1.10: Neutrino spectra from fission reactions. Image: T2K Collaboration

1.3.2 *Neutrino detectors*

Neutrinos interact very weakly which limits the options for detector designs to massive scales. The presently used detectors can be divided in several general types:[22]

(1) Unsegmeted scintillator detectors, used in for example Chooz, KamLAND an LSND. These detectors are typically used for low energy antineutrino experiments and consist of large tanks of liquid scintillator surrounded by phototubes. The protons in the scintillator provide a target for the inverse beta decay reaction. The most important issue for low energy experiments are the environmental backgrounds, coming mainly from naturally occurring radioactivity and muon-induced backgrounds.

(2) Unsegmented Cerenkov detectors, as used by for example MiniBooNE, Super K and AMANDA. These detectors consist of a large volume of a clear medium (like ice in the case of AMANDA and its successor ICECUBE), surrounded by phototubes. The Cerenkov cone that is projected on the detector is used as particle identification.

(3) Segmented scintillator-and-iron calorimeters, used in for example MINOS and NuTeV. These detectors are used to detect muon-neutrinos in the range of 1 GeV and higher. The iron is used as target while the scintillator provides information on energy deposition. This design allows discrimination between electromagnetic- and hadronic showers.

(4) Segmented scintillator trackers are used in for example SciBooNE, MINERνA and the recent NOνA experiment. This technology allows track reconstruction for low energy, low multiplicity events, by using scintillator strips without interspersing iron.

1.4 NEUTRINO ANOMALY

Neutrino oscillation experiments have established a picture of neutrino mixing and masses that explains the results of solar, atmospheric and reactor neutrino experiments. In the eighties and nineties, experiments were performed at a few tens of meters from nuclear reactor cores at ILL, Goesgen, Rovno, Krasnoyarsk, Bugey and Savannah River.[25] From the late nineties, middle- and long-baseline experiments were performed at CHOOZ[26] and KamLAND [27]. These experiments are consistent with the mixing of ν_e , ν_μ and ν_τ with three mass eigenstates, ν_1, ν_2 and ν_3. In particular, the mass differences are required to be $|\Delta m^2_{31}| \simeq 2.4 \times 10^{-3} eV^2$ and $\Delta m^2_{21} / |\Delta m^2_{31}| \simeq 0.032$.

Recently, in 2010, the specific reactor antineutrino flux per fission was reevaluated.[28] The electron to antineutrino data conversion got improved, relying on detailed knowledge of the decays of thousands of fission products, while the previous conversion procedure used a phenomenological model based on 30 effective beta-branches. The new calculation resulted in an increase of $3,5\%$ in the $\bar{\nu}$-flux. This increases the rate at which IBD reactions should be detected.

The above mentioned reactor neutrino experiments were examined, using the new value of the cross section per fission. The ratios of observed event rates to predicted event rates, $R = N_{obs}/N_{pred}$, are summarized in table 1.1. We observe a general systematic shift below unity. These reevaluations unveil a reactor antineutrino anomaly, which is still waiting for an explanation.

The increase in flux results in a deficit in observed neutrinos of $\sim 5,7\%$, at $0,943 \pm 0,023$. This deficit is known as the reactor antineutrino anomaly and is significant at the level of $98,6\%$ C.L.. The anomaly is consistent with being independent from the distance to the reactor core at distances $\mathcal{O}$(10m).

Table 1.1: For different neutrino experiments - with indicated properties about detector type, fissile composition and base line distance - the ratios N_{obs}/N_{pred} shown for the new calculated spectra. The *err* column is the total error published by the collaborations. Table: G. Mention et al., Reactor antineutrino anomaly.[28]

#	result	Det. type	^{235}U	^{239}Pu	^{238}U	^{241}Pu	L(m)	N_{obs}/N_{pred}	err(%)
1	Bugey-4	^{3}He + H_2O	0.538	0.328	0.078	0.056	15	0.942	3.0
2	ROVNO91	^{3}He + H_2O	0.614	0.274	0.074	0.038	18	0.940	3.9
3	Bugey-3-I	^{6}Li − LS	0.538	0.328	0.078	0.056	15	0.946	4.8
4	Bugey-3-II	^{6}Li − LS	0.538	0.328	0.078	0.056	40	0.952	4.9
5	Bugey-3-III	^{6}Li − LS	0.538	0.328	0.078	0.056	95	0.876	14.1
6	Goesgen-I	^{3}He + LS	0.620	0.274	0.074	0.042	38	0.966	6.5
7	Goesgen-II	^{3}He + LS	0.584	0.298	0.068	0.050	45	0.992	6.5
8	Goesgen-II	^{3}He + LS	0.543	0.329	0.070	0.058	65	0.925	7.6
9	ILL	^{3}He + LS	≃ 1	—	—	—	9	0.802	9.5
10	Krasn. I	^{3}He + PE	≃ 1	—	—	—	33	0.936	5.8
11	Krasn. II	^{3}He + PE	≃ 1	—	—	—	92	0.953	20.3
12	Krasn. III	^{3}He + PE	≃ 1	—	—	—	57	0.947	4.9
13	SRP I	Gd-LS	≃ 1	—	—	—	18	0.952	3.7
14	SRP II	Gd-LS	≃ 1	—	—	—	24	1.018	3.8
15	ROVNO88-1I	^{3}He + PE	0.607	0.277	0.074	0.042	18	0.917	6.9
16	ROVNO88-2I	^{3}He + PE	0.603	0.276	0.076	0.045	18	0.948	6.9
17	ROVNO88-1S	Gd-LS	0.606	0.277	0.074	0.043	18	0.972	7.8
18	ROVNO88-2S	Gd-LS	0.557	0.313	0.076	0.054	25	0.959	7.8
19	ROVNO88-3S	Gd-LS	0.606	0.274	0.074	0.046	18	0.938	7.2

The question arises whether the origin of this deviation from unity is an erroneous prediction of the anti- neutrino flux from the reactors, or a correlated artefact in the experiments, or a real physical effect.

Assuming the correctness of the new predicted cross section, the anomaly could be explained by a common bias in all reactor neutrino experiments. The experiments used different detection techniques, discussed in section 1.3.2. Some experiments looked only for the neutrons from the reaction, others included the positron signal as well. Neutrons were tagged either by their capture in metal loaded scintillators, or in proportional counters, thus leading to two distinct systematics. For the neutron detection efficiency calibration, we note that different types of radioactive sources emitting MeV or sub-MeV neutrons were used. The nuclear reactors operated with mixed fuels of ^{235}U, ^{239}Pu, ^{241}Pu and ^{238}U, which states that the anomaly cannot be associated with a single fissile isotope.
All the elements listed above argue against a trivial bias in the experiments, but a detailed analysis of the most sensitive of them would improve the quantification of the anomaly.

Another possible explanation for the anomaly is based on a real physical effect. If this deficit is due to neutrino mixing, it could be explained by an energy-independent suppression of the $\bar{\nu}_e$ flux at distances of $\mathcal{O}$(10m). The $\bar{\nu}_e$ could oscillate into yet another neutrino family. This new neutrino would require a $|\Delta m^2| \gtrsim 1eV^2$. The mixing amplitude with the $\bar{\nu}_e$ must be $\sin^2(2\theta_{new}) \sim 0.115$. The required $|\Delta m^2|$ is significantly larger than those required by solar and atmospheric experiments. The 3+1 neutrino scenario can be fitted on the measurement rates of short baseline reactor experiments, as a function of the distance to the reactor core (see figure 1.11). This produces a measurement of allowed regions of the Δm^2_{14} versus $\sin^2(\theta_{14})$.

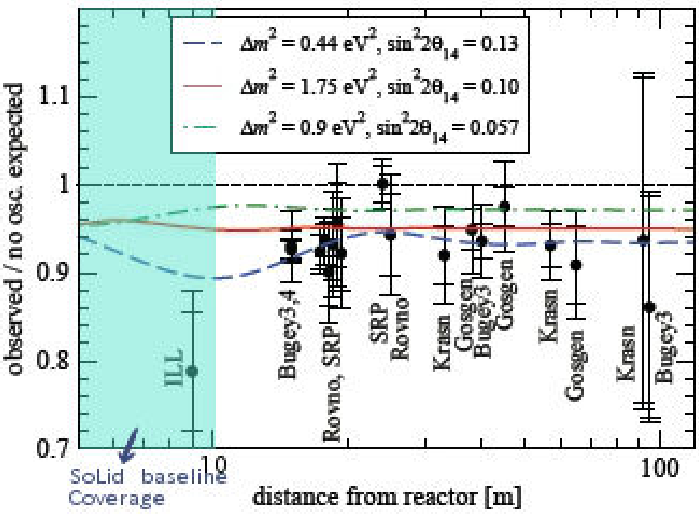

Figure 1.11: Measurement rate of $\bar{\nu}_e$ for different experiments in function of distance to the reactor core. The baseline coverage of the SoLi∂ detector is indicated in light blue. Image: W. Seligman and M. Shaevitz, Columbia University (2011)

If the neutrino mixing hypothesis is the correct explanation, this implies the existence of a fourth neutrino, beyond the standard model. Such particles would have zero electric charge, zero weak hypercharge, zero weak isospin, and no color and therefore belong to a singlet representation with respect to the strong interaction and the electroweak interaction. Due to the lack of charge, sterile neutrinos would not interact electromagnetically, weakly, or strongly, making them extremely difficult to detect. They have Yukawa interactions with ordinary leptons and Higgs bosons, which via the Higgs mechanism leads to mixing with ordinary neutrinos. In experiments involving energies larger than their mass they would participate in all processes in which ordinary neutrinos take part, but with a quantum mechanical probability that is suppressed by the small mixing angle. However, they would interact gravitationally due to their mass, and if they are heavy enough, they could explain dark matter.

I would like to stress that the other explanations are still possible, such as a correlated artefact in the experiments, or an erroneous prediction of the antineutrino flux from nuclear reactor cores.

The possibility of the existence of a reactor antineutrino anomaly is reinforced by its compatibility with the gallium anomaly; a similar deficit in the measured ν_e flux was found when intense ^{51}Cr and ^{37}Ar radioactive sources were used to calibrate the SAGE[29] and GALLEX[30] solar neutrino experiments. The deficit is known as the Gallium anomaly, since the experiments use radiochemical gallium-targets to study solar neutrinos.
The GALLEX (G) -and SAGE (S) experiments indicate respectively a ratio R of measured and predicted event rates which is smaller than unity:

$$R_{G1} = 0,953 \pm 0,11, \tag{1.28}$$

$$R_{G2} = 0,812^{+0,10}_{-0,11}, \tag{1.29}$$

$$R_{S1} = 0,95 \pm 0,12, \tag{1.30}$$

$$R_{S2} = 0,791^{+0,084}_{-0,078}. \tag{1.31}$$

The uncertainty on the deficit was estimated, taking into account the uncertainty of the detection cross section. The statistical significance of the anomaly was calculated to be $\sim 3,0\sigma$.[31] A fit of the data in terms of neutrino oscillations favours at $\sim 2,7\sigma$ a short-baseline electron neutrino disappearance with respect to the null hypothesis of no oscillations.

These reactor anomalies point out that new experimental constraints are needed. All anomalies appeared at a similar energy to distance ratio (L/E) and could be the result of an oscillation into a sterile neutrino (if the sterile neutrino has a mass of ~1 eV). Unfortunately, all anomalous results are close to the limit of sensitivity or do not provide information about the energy dependence of the phenomenon: sterile neutrinos have yet to be experimentally established or ruled out.

Nearly all prior experiments on the neutrino anomaly rely on the measurement of an integrated neutrino flux, measured at a fixed distance from the neutrino source. However, the theoretical predictions of the neutrino flux -and the neutrino energy spectrum are in itself very challenging tasks. The new generation of experiments should therefore perform an oscillometric analysis by using a position sensitive detector with a good energy resolution, sufficient detection efficiency, and with as little as possible theoretical model dependence. The SoLi∂ experiment aims to do just that.

2 THE SOLI∂ DETECTOR

2.1 OBJECTIVE

The Standard Model neutrinos are known to oscillate from one flavor to another. But recently, oscillation data from different experiments seem to deviate from the paradigm of an oscillation between three neutrino flavors. These so-called neutrino anomalies support the hypothesis of the existence of a new sterile neutrino family. In this context, new experimental constraints are needed to clarify the reactor anomaly. The SoLi∂ project proposes to confirm or refute the reactor anomaly and test ultimately the fourth sterile flavor.

In section 1.2.3, we derived for a simple 2 phase scenario the probability that an initial ν_e changes in the μ-flavor state during its oscillation, after travelling a distance L at nearly the speed of light. We found equation 1.19 that says

$$P_{\nu_e \to \nu_\mu} \approx sin^2(2\theta)\,\sin^2\left(1,27 \times \frac{\Delta m^2}{\mathrm{eV}^2}\frac{L}{\mathrm{km}}\frac{\mathrm{GeV}}{E}\right). \tag{2.1}$$

We see that neutrino oscillation is an energy- and distance dependent phenomenon. The most effective way to address the neutrino anomaly is to measure a deficit of events as a function of anti-neutrino energy and distance. Recalling equation 1.21 that describes the oscillation length as

$$L = \frac{4\pi\ E}{\Delta m^2}, \tag{2.2}$$

we can estimate the oscillation length of sterile neutrinos. The average $\bar{\nu}_e$ has an energy of 2 MeV (see figure 1.10 on page 20). In case the sterile neutrino has a mass of about $\sim$1 eV and if we take an estimate on the $\bar{\nu}_e$ mass of 0,1 eV[32] then their squared mass difference becomes Δm^2 = 0,81 eV^2. The oscillation length is in this case

$$L \approx \frac{4\pi\ 2\cdot 10^6}{0,81} 1,97327\cdot\ 10^{-7} m \tag{2.3}$$

$$\approx 3\ m. \tag{2.4}$$

For the squared mass differences that are indicated on figure 1.11, namely $0,44\mathrm{eV}^2$ and $1,75\ \mathrm{eV}^2$, the oscillation length becomes respectively 5,6m and 1,41m.

To be optimally sensitive to these oscillation lengths, the detector has to be at close stand off from the reactor core. The current experiments, despite their remarkable precision, are too far away from large reactor cores. They are only sensitive to lower mass differences. The SoLi∂ short baseline experiment will make a measurement at close proximity from the SCK·CEN BR2 reactor using the next generation detector technology with the aim to deliver unprecedented sensitivity on the search for new oscillations (see figure 1.11).[33] At the same time, it will provide one of the most precise measurements of a pure ^{235}U anti-neutrino spectrum, an essential ingredient for the improvement of the reactor flux calculation.

The analysis will use the fine segmentation of the detector to split the fiducial volume of the detector in an optimized set of distances. The analysis will compare the shape of the spectrum accumulated at various distances thereby cancelling flux normalization errors. This is what is called a shape only analysis since it relies only on the overall difference in shape and not in difference of total rate. The total detector will search for an oscillation corresponding to the mass splitting region 0,5 - 5 eV^2, probing most of the region of the neutrino anomalies and a large fraction of the low mass area currently favored by cosmological data.

2.2 THE IBD REACTION

The SoLi∂ detector measures $\bar{\nu}_e$ coming from the reactor core of the BR2 research reactor. The energy of the reactor neutrinos lies in the low range of the neutrino energy spectrum (see figure 1.5 on page 16). In this range the interaction cross section is dominated by Quasi-elastic scattering (see figure 1.7), especially by the Inverse Beta Decay (IBD, see figure 1.8). This IBD channel will be probed by the SoLi∂ collaboration. In the IBD reaction an electron antineutrino reacts with a proton in the target, releasing a thermal neutron and a low energy positron

$$\bar{\nu}_e + p \rightarrow e^+ + n(E_\nu > 1,805 MeV). \tag{2.5}$$

The positron annihilates almost immediately with an electron, producing photons of 511 keV that can be detected, resulting in a prompt signal (see figure 2.1). The energy of the positron is linearly correlated with the initial neutrino energy

$$E_\nu = E_{e^+} + \Delta + \frac{E_{e^+}(E_{e^+} + \Delta)}{M} + \frac{1}{2}\frac{(\Delta^2 - m_e^2)}{M}, \tag{2.6}$$

with $\Delta = M_n - M_p$. The positron energy therefore has key importance to be determined.
The neutron loses its energy as it makes its way through the detector medium, it thermalizes. After about 90 μs, the thermalized neutron gets captured on a target, which emits photons that make up a delayed signal.

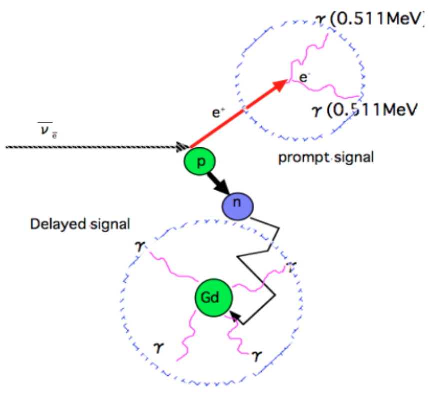

Figure 2.1: The inverse beta decay. Image: R. Fernandez, Nevis Labs

An estimation of the expected rate of interactions per tonne of fiducial volume can be calculated using the knowledge of the IBD cross-section and a model of the anti-neutrino flux. The average number of expected anti-neutrino signals is $R_{\bar{\nu}_e}$ = 1198/day/2,88t.[34]

The SoLi∂ detector is composed of two scintillation media to detect the product of the IBD interaction.[33] The first medium is made of Poly-Vinyl Toluene (PVT) in the form cubes of $5 \times 5 \times 5$ cm^3. This is an inorganic scintillator which is sensitive to charged particles and gamma rays. It also acts as the proton-rich target for antineutrino interactions. The cubes are stacked in a 3D matrix (see figure 2.2 left). Every cube is covered with a second medium to detect the neutron, namely ^{6}LiF:ZnS(Ag). The neutron is captured by the ^{6}Li to produce a tritium atom and an alpha particle;

$$n +^6 Li \rightarrow^3 H + \alpha + 4,78 MeV. \tag{2.7}$$

The alpha particle and tritium excite the surrounding grains of ZnS to the triplet state. These states have a decay time constant of about 200 ns, which is significantly slower than the organic signal of the PVT (see figure 2.2 right). The neutron signal has a sharp rising edge and a relative long tail. This signal will be used for triggering data collection.

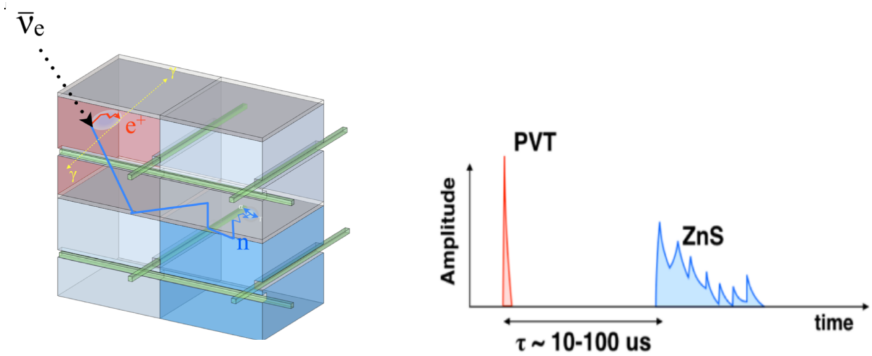

Figure 2.2: Left: the IBD reaction in basic detector elements of the SoLi∂ detector. The scintillation light (PVT or ZnS) is collected by wavelength shifting fibres with X and Y orientation. Right: Corresponding scintillation decay and coincidence times to reconstruct the IBD event. Images: SoLi∂ Collaboration.

The PVT cubes around the ^{6}LiF:ZnS(Ag) screen act as an efficient neutron reflector. Therefore, a single thermal neutron may cross the same screen multiple times. As the neutrons average kinetic energy is around 10 keV it is likely to be absorbed in a different cube than the positron, which enables some capability to reconstruct the antineutrinos direction.

2.4 SIGNAL-COLLECTION

Both the PVT and the ZnS scintillators emit optical photons around 420 nm that can be collected by $0,3 \times 0,3 \times 90$ cm^3 fibres that run through grooves in the cubes.[33] The light collection is enhanced by polishing the cubes, which maximizes the internal reflection, and by wrapping a Tyvek reflector around the cube (see figure 2.3). After the Wave Length Shifting (WLS) fiber has shifted the collected light to green wavelengths, the light is transported to the end of the fiber where it is collected by a Geiger mode avalanche photo-diode array (called MPPC). When using a configuration with at least

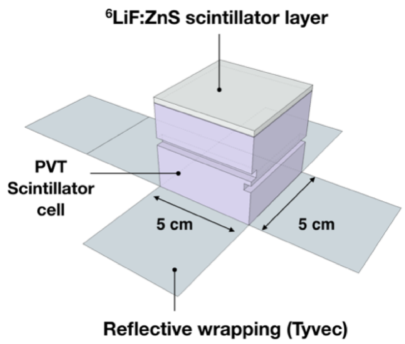

Figure 2.3: The unit scintillator cell, consisting of a PVT cube and a ^{6}LiF:ZnS(Ag) screen, wrapped in a reflective tyvek layer. Image: SoLi∂ Collaboration.

two perpendicular fibres, the position of the scintillation signal can be reconstructed. This enables a 3D reconstruction of all signals, downsized to single cubes. This leaves the possibility to construct a large target volume whilst retaining high position resolution. The choice of read out makes the design very compact around the target volume, maximizing the use of the available volume for physics.

2.5 DATA-TRIGGERING

The detection chain is set in motion by triggering on a neutron signal.[33] The neutron capture efficiency on the ^{6}LiF:ZnS(Ag) is close to 60%. ZnS is one of the brightest inorganic scintillators and it has very little quenching factor. The bright and well defined signal stands out from γ -and other electromagnetic signals, providing a robust identification for neutrons. The neutron detection efficiency is, next to the neutron capture efficiency, also dependent on the light collection. If the number of collected photons is low, the neutron signal may not trigger the data acquisition or the signal may be difficult to distinguish from electromagnetic events unambiguously. Even though a neutron capture can produce up to 160 000 optical photons, variations in the detected number of photons are very large. The distribution in figure 2.4 is far from a Gaussian-like shape, which is expected for a fixed energy and fixed resolution.

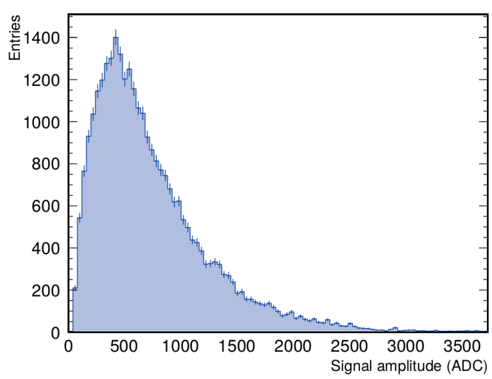

Figure 2.4: Distribution of the amplitude of neutron signals, captured by a ^{6}LiF:ZnS(Ag) screen and recorded with an MPPC. Image: SoLi∂ Collaboration.

After triggering on a neutron, a spatial cut is defined around the position of the neutron signal to look for a prompt positron signal within a specified delay time preceding the neutron event (see figure 2.7). The offline neutron identification will be improved by studying the characteristic delay time between the scintillation signals due to the annihilation of the positron and the thermalized neutron, which is now set on 200 microseconds on average.

2.6 THE BR2 RESEARCH REACTOR

The size of the oscillations we are looking for are of the order of a few meters. The size of the reactor core therefore dictates the maximum resolution on the oscillation length that the experiment can have. However, power reactors have in general large cores. The current experiments, despite their exquisite precision, are too far away from large reactor cores and are only sensitive to lower mass difference. The SoLi∂ short baseline experiment will perform measurements at 5,5 m from the BR2 reactor core.[34] The reactor is operated by the Belgian Nuclear Research Center SCK·CEN in Mol, Belgium. It has a tank-in-pool design, uses high enriched uranium fuel and is Be -and water moderated. The twisted design of the BR2 matrix provides a compact fission rate distribution, required for sensitive searches of oscillations at close distance. The SoLi∂ detector has a suitable energy resolution (15% at 1MeV) and the background conditions at BR2 are relatively low compared to other research reactors, with a stable and predictable environment over several years.

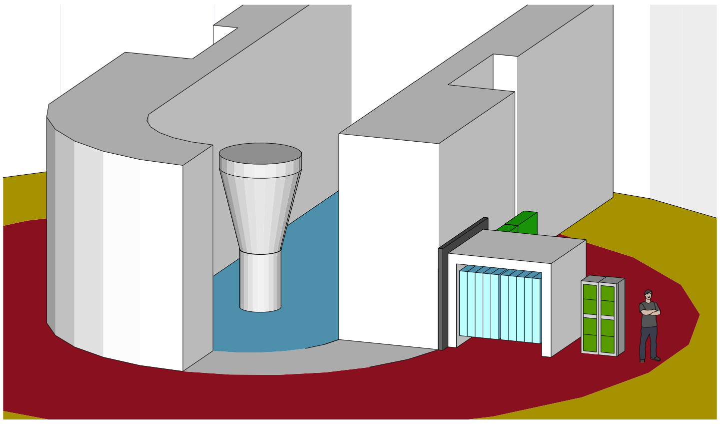

Figure 2.5: Schematic view of the SoLi∂ detector, installed at the BR2 reactor. The detector is shielded from gamma-rays by a lead wall in front of the reactor concrete wall and is surrounded by high density Polyethylene shielding for neutrons. Image: SoLi∂ Collaboration.

A 300kg test module (SM1) has been installed in 2015, on axis with the BR2 reactor core in an experiment hall of the reactor building (see figure 2.6). Analysis of the collected data allowed an optimization of some of the design parameters for the detector. By the summer of 2016, 20-30 detection planes will be installed, which will be extended to 50 detection planes in 2017, allowing time for laboratory tests and calibration.
The final detector geometry will consist of 50 layers consisting of a matrix of 16 by 16 cubes per layer, bundled in 5 sub-modules of 10 layers each. The detector will be read out by a network of 3200 WLS fibers with one MPPC connected on alternating end faces of each fiber.

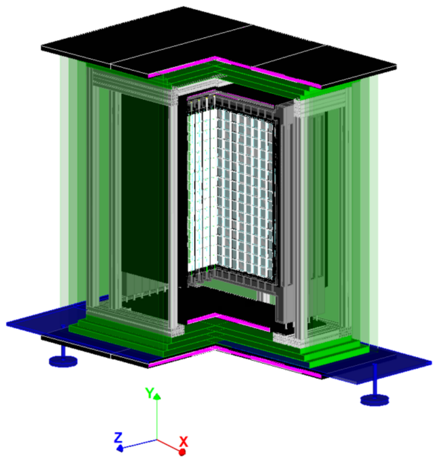

Figure 2.6: Diagram of the detector module showing 5 cm PVT cubes in a matrix of 16 by 16 cubes per layer, constructed inside aluminium frames. Image: SoLi∂ Collaboration.

2.7 BACKGROUND STUDIES

To perform the analysis, we need to measure the antineutrino interactions and control and understand the backgrounds.
During the measurement, the device triggers on the characteristic pulse shape of a thermalized neutron that is absorbed on ^{6}LiF:ZnS(Ag), which provides a very bright and robust scintillating signal that appears different in time and intensity from the background of gamma-ray interactions. At triggering, the pulse shapes of all detection cubes are buffered in a time window extending over several 100 μs. An offline selection of neutrino candidates is based on the positron signal that occurs on average 200 μs before the neutron capture; After the IBD reaction, the positron annihilates promptly into two photons, whereas the thermal neutron first slows down via inelastic scattering before it is absorbed by the Li sheet on the cubes. The neutron thermalizes typically 1-3 cubes away from the prompt positron signal. The fine spatial segmentation of the SoLi∂ detector allows to optimally select signal events based on this topologic characteristic. The specific time -and spatial separations of the detection of the positron and the neutron allow to discriminate the IBD event from the background.

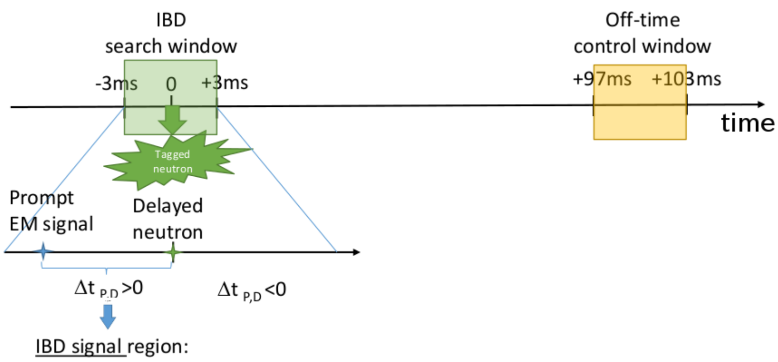

Figure 2.7: Indication of the timing of the IBD event. The off-time control window allows to eliminate the accidental background. Image: SoLi∂ Collaboration.

Measurements conducted in 2015 indicate clearly which backgrounds the experiment is facing with.
The first dominant background is the accidental measurement of gamma -and neutron signals from the reactor, where the gamma ray mimics the positron signal. The accidental background adds an in-time background with the anti-neutrino signal that is difficult to control, especially at very close distance. Since the accidental background is random in time, it can be controlled by comparing the signals in the in-time IBD window with the signals in an off-time control window (see figure 2.7).

Furthermore, The Lithium compound in the ^{6}LiF:ZnS layer is at risk of contamination by Bismuth, which is a by-product of the ^{6}Li production in reactors; The Bismuth is a radio-progeny of the uranium isotope that is used in the reactor (See figure 2.8 left). Within the ^{6}LiF:ZnS layer, the ^{214}Bi can decay to ^{212}Po. A 7,69 MeV α-particle, emitted by the ^{212}Po, could look like a neutron. If preceded by the emission of a 3,27 MeV β-electron by the Bismuth, this can fake an IBD coincidence signal with similar time scales (see figure 2.8 right). However, the prompt and delayed signal will occur in the same cube. Due to the segmentation of the SoLi∂ detector, the background can be measured and subtracted, using this geometrical information in terms of number of cubes between the neutron and the positron signal. A definite upper limit for this background will be obtained by measuring large volumes of the LiF in deep underground, low radioactovity laboratories.

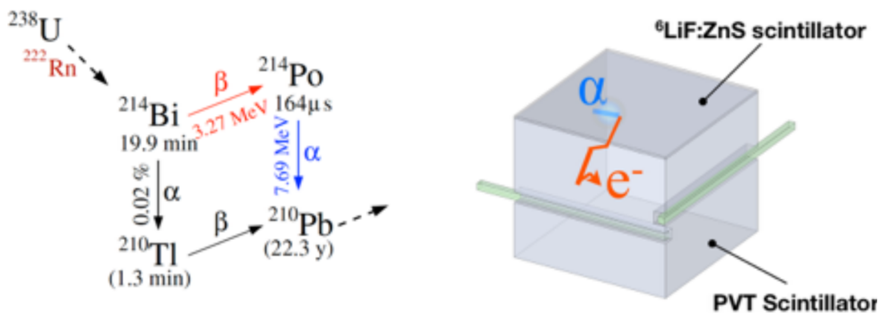

Figure 2.8: Left: In the production process of ^{6}Li within a ^{238}U reactor, the uranium can decay into Bismuth which can contaminate the ^{6}Li. The ^{214}Bi can fake an IBD signal which is located in one or two cubes (right). Image: SoLi∂ Collaboration.

The experiment also has to deal with a cosmogenic background, due to the small overburden of the experiment.
The detector is sensitive to detect fast neutrons from cosmic ray showers. These will induce a proton recoil signal, which mimics the positron signal, followed by a capture of the cosmic neutron on the Li layer. In order to reduce this background, the detector will be surrounded by a 30cm thick water shield to moderate the fast neutrons.
Cosmic muons also contribute to the background. They are clearly identified through the reconstruction of a straight track in the detector and/or by the typical very large electromagnetic energy deposition in the PVT cubes (10MeV/cube). The traversing track creates clusters of channels on the xz and yz planes (horizontal and vertical fibres) in the SM1 detector (see fig-

ure 2.9). This pair of clusters has to be correlated in time allowing the identification.

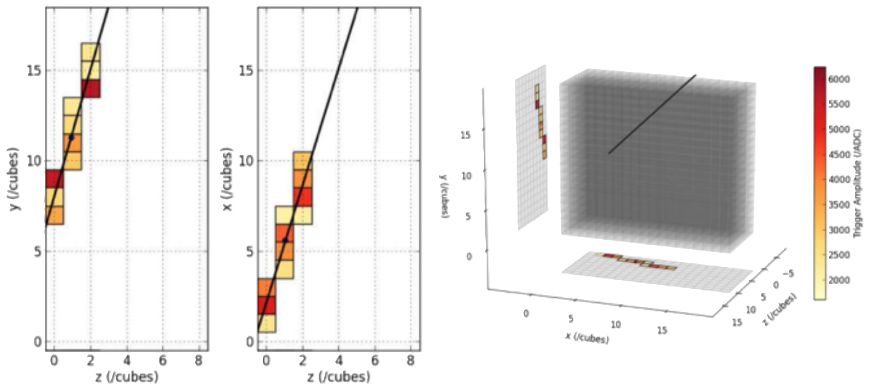

Figure 2.9: Pair of clusters (horizontal and vertical fibers) thate are created by the same muon track. Image: SoLi∂ Collaboration.

Cosmics muons also can induce spallation reactions that spontaneously emit fast neutrons, or produce excited nuclear states of carbon, lithium, etc. The muon induced backgrounds will be tagged by an active muon veto umbrella covering the top and sides of the experiment.
Other backgrounds include possible radioactive contamination of detector material, thus producing very localised energy deposition with a different time structure as IBD events.

The combination of both pulse shape, timing and topological information of the IBD event will allow for a clean detection of $\bar{\nu}_e$ candidates, in particular when a large fiducial volume of 1,5 cubic meter is deployed. Sufficient low density shielding (Polyethylene), a lead wall of 20 cm thickness allows to reduce further the accidental and correlated background rate.

The selection requirements for IBD tagging and rejection will be optimized by comparing observed events with millions of simulated events. Also, the clustering of electromagnetic energy deposition can be optimised for a better neutrino energy reconstruction and resolution. We will finally develop an oscillation analysis using the most sensitive statistical methods (Bayesian likely hood and multivariate, multimodal techniques). For this purpose a full software framework has to be developed (raw data, structure and read out, database content, analysis algorithms, reconstructtion, integration simulation in the framework and so on).

3 PHOTON TRANSPORT AND COLLECTION

The principle of the SoLi∂ detector is essentially based on the collection, transportation and detection of light. An accurate measurement of the $\bar{\nu}_e$ and a precise determination of its energy, requires good light yield and uniformity of the detector response. The light collection scheme consists of random reflections of scintillation light in a scintillator cube, capturing and wavelength shifting the light in the WLS fiber and transporting the light to an MPPC for detection. Achieving high light yield requires great care as there are many opportunities for the photon to escape detection. It is therefore important to understand and control the different parameters that contribute to the photon transport. To this end, a test bench has been set up to measure the light yield experimentally and a simulation has been developed to emulate and optimize the photon transport parameters for the full photon chain. In the upcoming sections, we start by discussing the different optical components.

3.1 OPTICAL COMPONENTS

3.1.1 *The scintillator*

A scintillator is a material that will absorb the energy of an incoming particle, to get into an excited state, and re-emit the absorbed energy in the form of light. Sometimes, the excited state is metastable; the relaxation from the excited state to a lower state is delayed (ranging from a few nanoseconds to hours depending on the material). The process corresponds to either delayed fluorescence or phosphorescence, depending on the type of transition and hence the wavelength of the emitted optical photon.

In the SoLi∂ experiment, the reaction products from the inverse beta decay between the $\bar{\nu}_e$ (that we wish to probe) and a proton (from the detectormedium) are a positron and a neutron. The photons that are created by the positron and the neutron, are the ionizing particles that excite the scintillator.
For photon measurements with scintillators, only three interaction mechanisms play a significant role.[36] All those mechanisms lead to the complete -or partial transfer of photon energy to electron energy. Meaning the abrupt change of a photon by its absorption or scattering, in contrast to slow deceleration by many simultaneous interacting absorber atoms. The three important interaction mechanisms are photoelectric absorption, compton scattering and pair production.

In the case of **photoelectric absorption** the photon gets absorbed entirely by an atom, whereby a photo electron is set free (see figure 3.1).

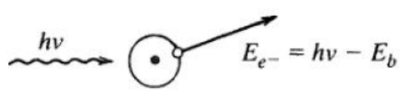

Figure 3.1: Photoelectric absorption. Image: J. Knoll

The photo electron has an energy that is equal to the photon energy E_e with the bonding energy E_b, that bound the electron to the atom, subtracted.

$$E_e = h\nu - E_b, \tag{3.1}$$

with h Planck's constant and ν the photon frequency. The photo electric absorption is the dominant mechanism for radiation of low energy. The absorption becomes more probable for a material with a high atomic number Z (see figure 3.3 left).

In **compton scattering** a photon is deflected over an angle θ under the influence of an electron (see figure 3.2). A part of the photon energy is transferred to the electron. The electron flies off and is designated as recoil electron. The detector can measure this recoil electron. All angles θ are a

Figure 3.2: Compton scattering. Image: J. Knoll.[36]

priori possible. There will be a wide range of energy transfers. In extremal events, the photon collides up front with an electron or grazes the electron. The probability for Compton scattering depends on the available electrons and therefore will be bigger for a material of high atomic number Z. (see figure 3.3 right).

Finally, **Pair production** can occur when the energy of the photon is twice as large as the rest energy of the electron. The photon disappears, creating an electron-positron pair. The remainder in photo energy goes to the kinetic energy of the pair.

$$h\nu + 2mc^2 = E_{e^-} + E_{e^+}$$

The probability for this mechanism is small. This will only occur for high energetic rays (see figure 3.3 bottom). After pair production, the formed positron will annihilate again, setting free two photons that make up the secondary result of pair production.

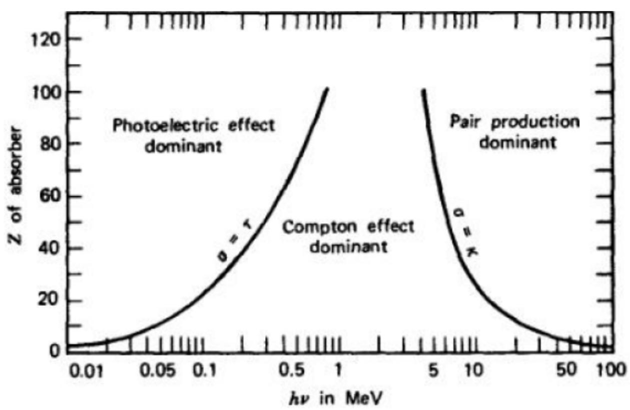

Figure 3.3: The dominant mechanisms in function of the energy deposit and the atomic number of the material. The left line indicates where the photoelectric -and comptoneffect become equally likely. The right line shows the same for the comptoneffect and pairproduction. Image: J. Knoll.[36]

In all three interaction mechanisms, electrons jump to an excited state or are set free, under influence of the ionizing particle. The left vacancy will be filled again, whereby light is emitted; the material fluoresces. The radiation is an indication for the energy that the ionizing particle deposited. The fluorescence process depends on the energy states of the material.

We will focus on the PVT scintillator and the ^{6}LiF:ZnS scintillator that are used in the SoLi∂ experiment. The former is a plastic scintillator whereas the latter is an inorganic scintillator.

The PVT scintillator

One of the scintillators that is used in the SoLi∂ experiment is a plastic scintillator, namely Poly-Vinyl Toluene (PVT). Such scintillators are built from aromatic compounds which are characterised by their carbon ring structure;[37] due to the hybridisation of the s and two p orbitals, the angles of the bondings of one carbon atom become 120° and lie in one plane (see figure 3.4 left). Hence, it is possible for the C-C bondings to arrange in a hexagonal ring structure, which is called benzene. The remaining non-hybridized p-orbitals overlap to form a molecular orbital containing delocalized electrons which contribute to the bonding of the molecule (see figure 3.4 right). Electrons in these π-orbitals can be excited by a traversing charged particle. The de-excitations to the ground state are responsible for the luminescence of this kind of materials.

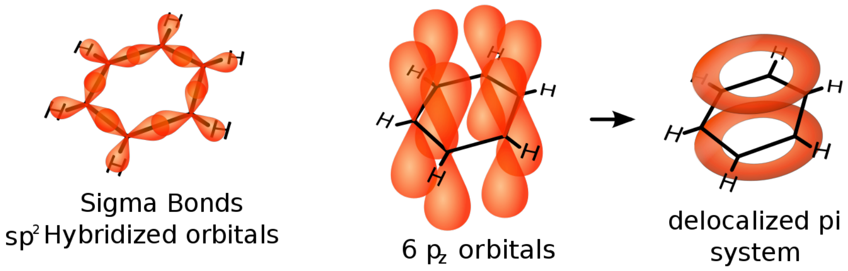

Figure 3.4: Left: Structure of σ-bonds (sp2hybridized orbitals) in the benzene molecule. Right: the non-hybridized p-orbitals (before arrow) that form a delocalized π-orbital system. Image: Vladsinger via Wikipedia.

Figure 3.5 shows a typical energy level diagram, with singlet and triplet states and small substructures caused by the excited vibrational modes of the molecule. The energy spacing of the fine structure is in the order of a few tenths of eV. After the electrons and the vibrational levels are excited by a traversing particle, the decay of the excited singlet states to S_1 takes place within picoseconds and proceeds without the emission of radiation which is known as internal degradation. From here the state decays with a high probability within a few nanoseconds to one of the S_{0j} states, emitting radiation with a wavelength corresponding to the energy difference of the states.

From the triplet state, it is prohibited to decay to the S_{0k}. However, they can decay by interaction with other excited T states

$$T_1 + T_1 \rightarrow S_1 + S_0 + phonons \tag{3.2}$$

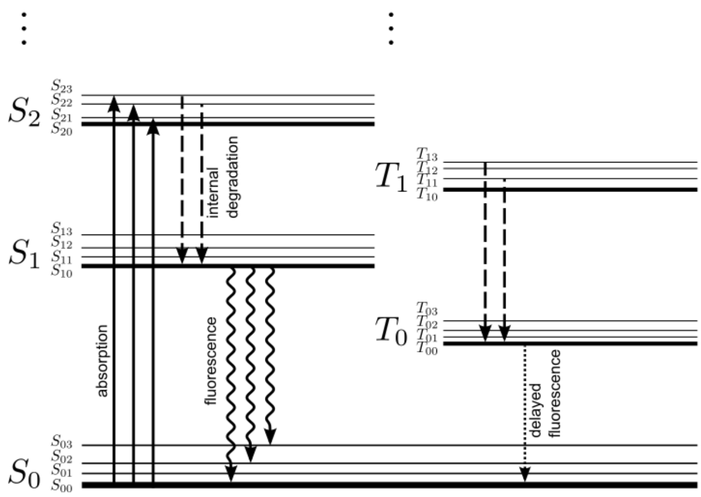

Figure 3.5: The singlet states S_{ij} and triplet states T_{ij} of a typical plastic scintillator. Image: J. Birks, The theory and practice of scintillation counting[37].

The S_1 state decays in the same way as described above, though some time later. The emitted light is now delayed with respect to the other scintillation light and is therefore called afterglow or phosphorescence. In addition, the emitted light is not within the range of visible wavelengths. To enhance the probability for the emission of visible photons and to decrease the decay time, fluorine compounds with a concentration of about 1% are mixed to the scintillating base material (see figure 3.6). Extra energy states appear, along which the electrons can de-excite to the ground state. The initial decay time that can be of the order of 15 ns or more can be reduced to a few nanoseconds. In order to decrease self-absorption, a second fluorine compound is solved in a small concentration (0.05%) that absorbs the short wavelength photons and emits them at higher wavelengths. [39]

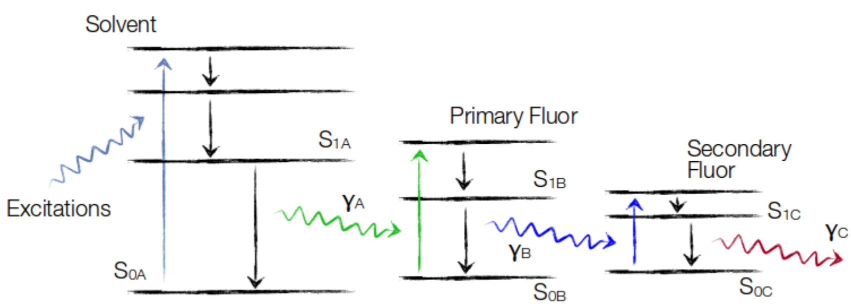

Figure 3.6: The working mechanism of a plastic scintillator: The base material gets excited by energy deposition. The absorption spectrum of the primary fluorine compound is matched to the excited states in the base material. The secondary fluor acts as wavelength shifter.[39]

The advantages of the PVT scintillators include fairly high light output (typically 25-30% of NaI(Tl)) and a relatively quick signal, with a decay time of 2,1 nanoseconds.[38] This makes the material suited for fast timing measurements. Another great advantage of the plastic scintillator is its ability to be shaped, through the use of molds or cutting.[41]

The emission spectrum of the PVT scintillator is shown in figure 3.7.

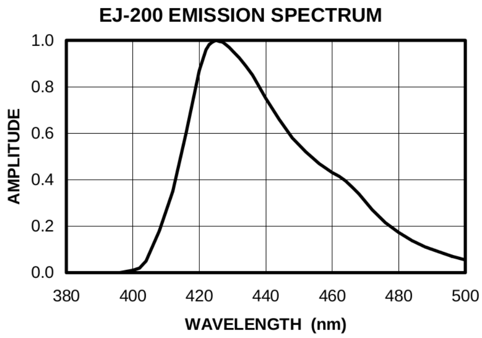

Figure 3.7: Emission spectrum of polyvinyl Toluene scintillator. Image: data sheet EljenTechnology.

The ^6LiFZnS scintillator

The second scintillator that is used in the SoLi∂ experiment is found in the ^{6}LiF:ZnS(Ag) sheet, namely the ZnS(Ag) inorganic scintillator.[40] The ^{6}LiF:ZnS(Ag) sheet is an efficient detector for thermal neutrons with a low sensitivity to gamma radiation. It has the form of a flat, white thin sheet consisting of a homogeneous matrix of fine particles of Lithium-6-Fluoride and Zinc Sulfide phosphor compactly dispersed in a colorless binder. The neutron detection process uses the nuclear reaction

$$^6Li + ^1n \rightarrow ^3H + ^4He + 4.78MeV. \tag{3.3}$$

This reaction has a cross section of 941 barns for 0,025 eV neutrons. The resulting tritium and alpha particle are detected by the ZnS(Ag) scintillator with a broad blue fluorescent spectrum (see figure 3.8).

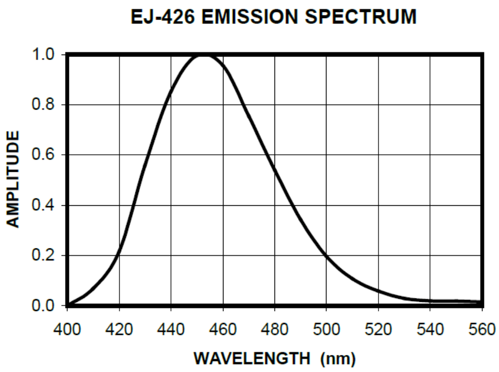

Figure 3.8: Emission spectrum of ^{6}LiF:ZnS(Ag) Image: Datasheet EljenTechnology.[40]

Other than the PVT scintillator, this is an inorganic scintillator. Its working principle is again based on the excitation of the scintillator material by an incoming particle and re-emission of the absorbed energy in the the form of light. But the excitation in inorganic materials is due to the electronic band structure found in crystals and is not molecular in nature as is the case with organic scintillators. The electron gets excited from the valence band, over the bandgap to the conduction band of ZnS. The vacancy that is left behind will be filled again, with the emission of light as consequence; the material fluoresces. However, this is not an efficient process. In addition, the light will not be visible. To increase the probability for the emission of visible photons, small impurities are added in the form of silver (Ag), so-called activators. Extra energy levels occur in the bandgap of the pure crystal, through which the electron can deexcite.

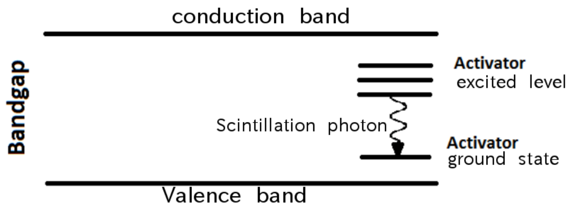

Figure 3.9: Energy levels of an inorganic scintillator crystal, doped with impurities that function as activators for deexcitation. Image: J. Knoll.[36]

The electron could also get trapped at the activator site and make an excited configuration from where a transition to the ground state is prohibited. With some extra energy, for example from thermal energy, the electron can go to a level that allows deexcitation. The emitted light is delayed with respect to the other scintillation light and is therefore called afterglow or phosphorescence (cfr. analogous to the PVT scintillator but due to other processes). The scintillation photons are emitted slowly, up to microseconds after the neutron capture on the ^{6}LiF:ZnS(Ag) screen.

The difference in decay time between the PVT scintillator and the ZnS(Ag) scintillator is very important for the SoLi∂ experiment. Because the ZnS(Ag) scintillator emits the photons slowly, its signal can easily be distinguished

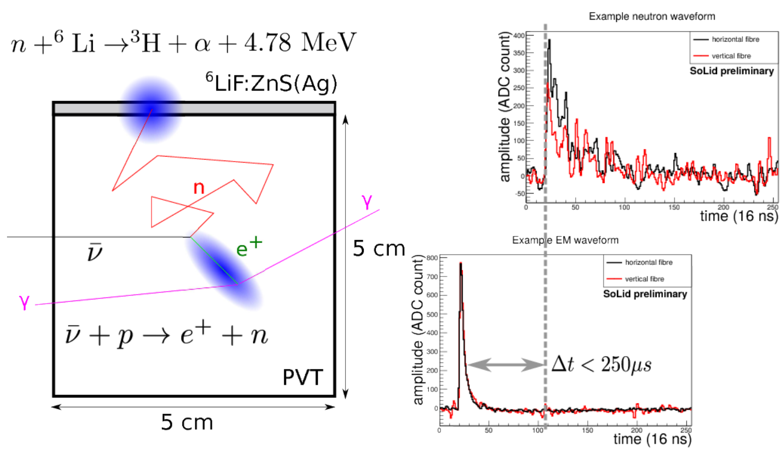

Figure 3.10: Comparison of scintillation signals from neutron capture (upper) in the ^{6}LiF:ZnS(Ag) and electromagnetic signals in the PVT scintillator (lower). Image: SoLi∂ Collaboration.

from the single light pulse from PVT scintillation. The differing time signatures for the light pulses can therefore be used to identify whether a given scintillation signal was produced in the ZnS (characteristic of a neutron capture) or in the PVT (e+/γ/μ-like).

3.1.2 *Tyvek wrapping*

To optimize reflection inside the scintillatorcubes, they are wrapped in a highly reflective material. Tyvek (DuPont registered trademark) is used because of its high reflectivity over a broad spectrum.

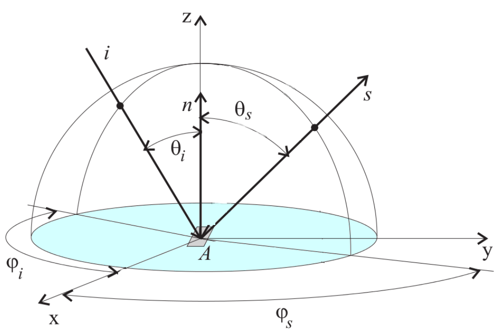

Figure 3.11: Geometry for the definition of BRDF. Image: Optical Society of America.

The exact reflection -and transmission properties of tyvek are important to determine, with regard to the optical simulation that will be dealt with in chapter 5. The reflective coefficients of tyvek were examined, by measuring the bidirectional reflectance distribution function (BRDF).[43] The BRDF fully describes the reflection scatter profile of an optical sample. It is a function of the incidence angle (θ_i, ϕ_i), the scatter angle (θ_s, ϕ_s) and the wavelength of the light λ (see figure 3.11). If Φ_i is a light flux irradiating the sample of area dA then the BRDF is given by[43]

$$f_s(\theta_i, \phi_i, \theta_s, \phi_s, \lambda) = \frac{\delta L(\theta_s, \phi_s, \lambda)}{\delta E(\theta_i, \phi_i, \lambda)} = \frac{d^2\Phi_s}{dA d\Omega_s \cos\theta_s} \frac{dA}{d\Phi_i} \cong \frac{d\Phi_s}{d\Omega_s} \frac{1}{\Phi_i \cos\theta_s}, \tag{3.4}$$

with δE the irradiance of the sample facet of area dA and δL the radiance contribution from the facet towards the observer (scatter direction) covering the solid angle $d\Omega_s$. Defining the radiant intensity of the scattered light as

$$\frac{d\Phi_s}{d\Omega_s} \equiv J((\theta_i, \theta_s, \phi_s), \tag{3.5}$$

we obtain the cosine-corrected BRDF function

$$f_{s,corr} \equiv f_s \cos\theta_s \cong \frac{1}{\Phi_i} J((\theta_i, \theta_s, \phi_s). \tag{3.6}$$

The radiant intensity $J((\theta_i, \theta_s, \phi_s)$ can be expressed as a sum of four reflection components and one transmission component (as is done in the UNIFIED model in the GEANT4 toolkit - see section 5.4 on page 69). The reflection components are governed by a series of coefficients C_n, namely the probability of specular lobe reflection around the normal of microfacets (C_{sl}), specular spike reflection around the average normal of the surface (C_{ss}), backward reflection (C_{bs}), and diffuse lobe reflection (C_{dl}).

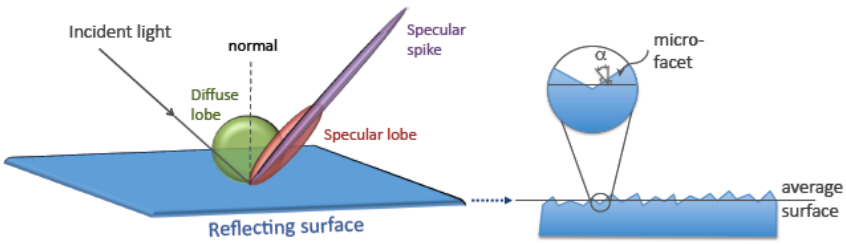

Figure 3.12: Left: Light reflection types, used in the calculation of the BRDF function and in GEANT4. Right: A ground surface is composed of micro-facets where alpha is the angle between a micro-facet normal and the average surface normal. Image: opengatecollaboration.

To describe the scatter profile of tyvek, only the specular lobe and the diffuse lobe components are taken into account. The specular spike component is relevant for surfaces with a RootMeanSquare roughness less than 1/4 of the light wavelength , i.e. polished surfaces. The backscatter spike component occurs when a light is reflected within a deep groove on very rough surfaces. Both cases do not apply to tyvek.
When, in addition, we focus on the reflection profile and leave out the transmission component, the cosine-corrected BRDF function becomes

$$f_{s,corr} \approx R(\theta_i)(C_{sl}g(\alpha, 0, \sigma_\alpha) + C_{dl}\cos\theta_s), \tag{3.7}$$

with R the surface reflectivity and $g(\alpha, 0, \sigma_\alpha)$ the Gaussian distribution of the deviation of the angle α of micro-facet normals with respect to the mean surface normal (see figure 3.12 right).

BRDF profiles are measured with a scatterometer for several angles of incidence from a 325 nm laser. The resulting BRDF functions are plotted in figure 3.13 with the corresponding fit results based on equation 3.7. The assumptions for the reflection given by the combination of Lambertian and Gaussian terms are valid for angles up to 30° and acceptable at 45°. For angles greater than 45°, the fitting deviates from the data.

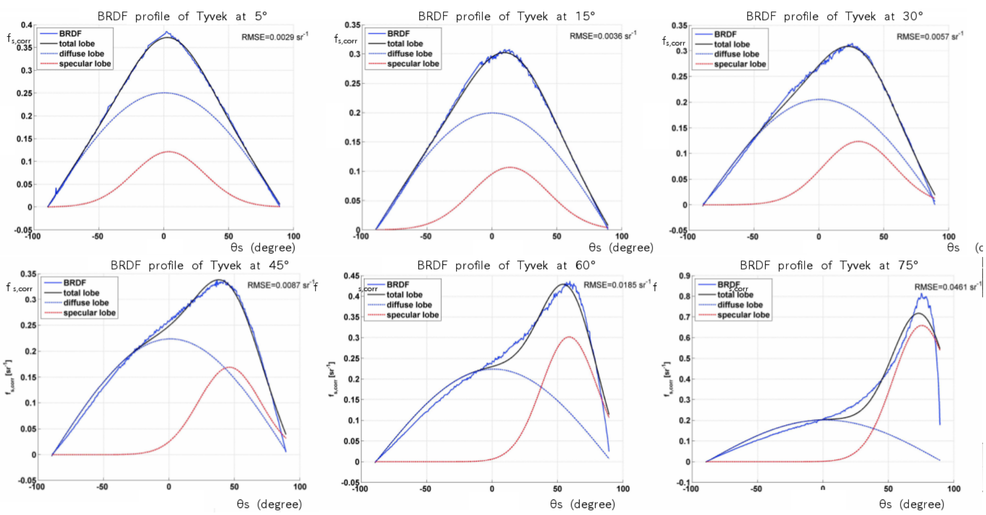

Figure 3.13: BRDF functions of Tyvek for various angles of incidence. Image: Optical Society of America..

The measurements were also performed with lasers of other wavelengths. This showed that the BRDF profiles are not dependent on the wavelength of the light source and the specular character of the reflection becomes more significant at higher incidence angles.
The mean parameters $C_{sl,corr}$, $C_{dl,corr}$ and σ_α for different wavelengths are listed in table 3.1. These values are incorporated in the GEANT4 simulation of the tyvek wrapping, within the scope of the LUT model for the modeling of boundaries (see section 5.4 on page 69).

Table 3.1: Normalized parameters for BRDF functions of Tyvek for various angles of incidence. These parameters are incorporated in the LUT-model of GEANT4. Table: Optical Society of America.[43]

θ_i [°]	$C_{dl,corr}$		$C_{sl,corr}$		σ_α [rad]	
	325 nm	633 nm	325 nm	633 nm	325 nm	633 nm
5	0.82 ± 0.05	0.83 ± 0.03	0.18 ± 0.05	0.17 ± 0.03	0.22 ± 0.02	0.22 ± 0.03
15	0.80 ± 0.03	0.78 ± 0.04	0.20 ± 0.03	0.22 ± 0.04	0.26 ± 0.02	0.27 ± 0.03
30	0.80 ± 0.02	0.80 ± 0.03	0.20 ± 0.02	0.20 ± 0.03	0.24 ± 0.02	0.24 ± 0.02
45	0.81 ± 0.02	0.79 ± 0.02	0.19 ± 0.02	0.21 ± 0.02	0.21 ± 0.02	0.20 ± 0.01
60	0.74 ± 0.02	0.73 ± 0.03	0.26 ± 0.02	0.27 ± 0.03	0.18 ± 0.02	0.17 ± 0.03
75	0.52 ± 0.04	0.57 ± 0.05	0.47 ± 0.04	0.43 ± 0.05	0.19 ± 0.02	0.15 ± 0.03

3.1.3 *WLS fibers*

To extract the photons from the scintillator cube and guide them to the readout device, wavelength shifting fibers are used.[45] These plastic bars absorb light at a given wavelength and emit it isotropically at a longer wavelength, i.e. lower energy. A portion of the re-emitted light is transmitted by total internal reflection along the WLS fiber to be read out at the ends.
Key performance parameters are good optical transmission across a broad range of wavelengths and highly polished surfaces to promote total internal reflection.

The SoLi∂ experiment uses BCF-91A WLS fibers, which consist of a polystyrene based core and are cladded with a double layer of PMMA - polymethylmethacrylate, $C_5H_8O_2$ (see figure 3.14 right). The material has a short decaytime of 12ns and a large attenuation length for its own light of $X_0 > 3,5$ m. The fiber shifts blue light to green wavelengths (see figure 3.14 left), with an emission peak at 494nm.

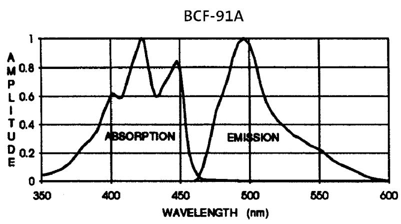

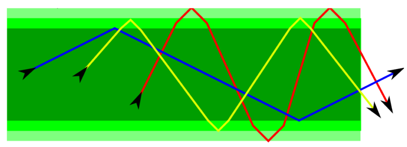

Figure 3.14: Left: Absorption- and emission spectrum of the WLS fiber, used for the SoLi∂ experiment. Image: Saint-Gobain crystals. Right: Schematic sideview of a double cladded Wavelength Shifting Fiber (WLS). The lowering refractive indices enhance the trapping efficiency. Image: SoLi∂ Collaboration.

By comparing the spectra in figure 3.14 and figure 3.7, we see that the PVT emission has its maximum in the absorptionrange of the fiber.

The scintillating core contains a combination of fluorescent dopants selected to produce the desired scintillation-, optical- and radiation-resistance characteristics. The PMMA cladding has a lower refractive index (1.49) than the core (1.59) to enhance the trapping efficiency of light inside the WLS fiber. The trapping efficiency is for the square fiber around 4% and is independent of the scintillation event's location in the fiber.
The second layer of cladding on the WLS fiber has an even lower refractive index (1.42) and, thus, permits total internal reflection at a second boundary. The additional photons guided by multi-clad fibers increase the output signal up to 60% over conventional single-clad fibers.

3.1.4 *The MPPC photodetector*

The multi-pixel photon counter, **MPPC** in short, is a photon-counting device, capable of detecting extremely low-level light.[46] The MPPC consists of multiple APD (avalanche photodiode) pixels operating in Geiger mode.[47] Geiger mode is a way of operating an APD so that it produces a fast electrical pulse of several volts amplitude in response to the detection of even a single photon (see figure 3.15 left). This pulse can trigger a digital CMOS circuit (complementary metal-oxide semiconductor) incorporated into the pixel. Single photon sensitivity and sub-nanosecond timing precision can be achieved.

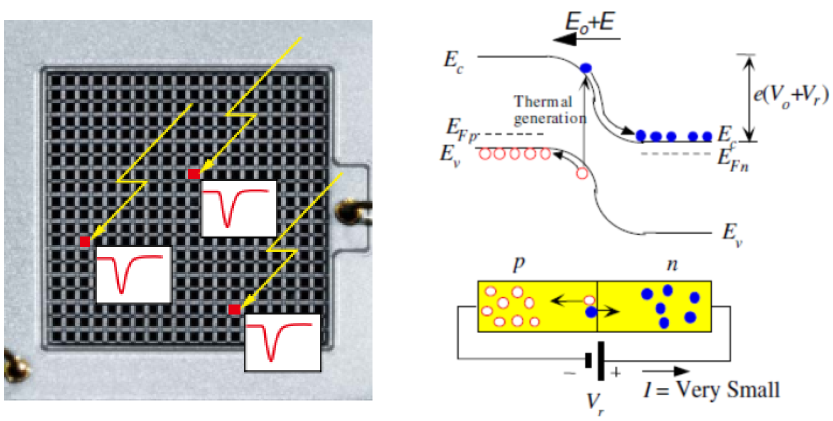

Figure 3.15: Left: principle of MPPC's photon counting. Image: HAMAMATSU.[46] Right: created electron hole pair drift in opposite direction under influence of the electric field around the reverse-biased p-n junction. The energy band diagram is also shown. Image: G. Barbarino et al.[48]

An APD is a variation of a **p-n junction photodiode**. When a p-n junction photodiode is reverse biased, an electrical field exists in the vicinity of the junction that keeps electrons confined to the *n* side and holes confined to the *p* side. When an incident photon of sufficient energy (> 1.1 eV in the case of silicon) is absorbed in the region where the field exists, an electron-hole pair is generated. Under the influence of the field the electron drifts to the *n* side and the hole drifts to the *p* side, resulting in a flow of photocurrent in the external circuit (see figure 3.15 right). The time integral of the current is one electron charge.

The number of electron-hole pairs that is generated per incident photon, i.e. the quantum efficiency, is at best unity. Losses due to reflection or absorption in zero-field regions usually lower the quantum efficiency. An electron-hole pair can also be generated thermally, resulting in the so-called **dark current** because it is present even in the absence of incident light.

Compared to the p-n junction photodiode, the **avalanche photodiode** supports high electric fields. When an electron-hole pair is generated by photon absorption, the electron can accelerate and gain sufficient energy from the field to collide with the crystal lattice and generate another electron-hole pair, losing some of its kinetic energy. This process is known as impact ionization. The electron can accelerate again, as can the secondary electron or hole, and create more electron-hole pairs, hence the term avalanche. After a few transit times, a competition develops between the rate at which electron-hole pairs are being generated by impact ionization and the rate at which they exit the high-field region and are collected.

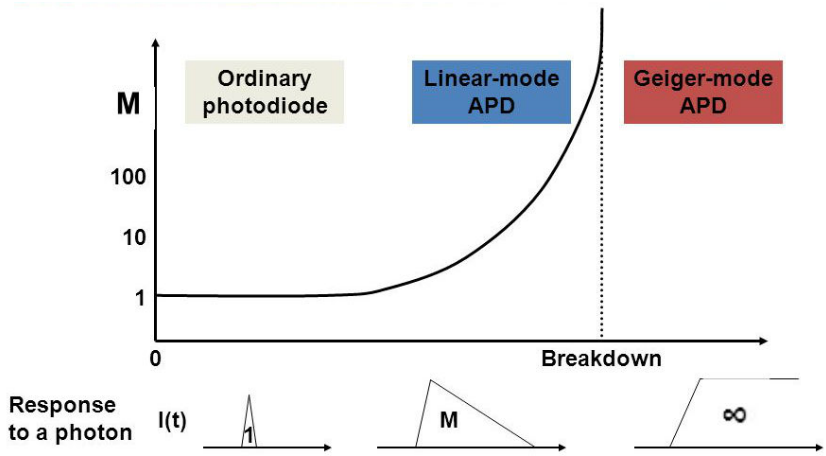

Figure 3.16: Gain of an ordinary APD, a Linear-mode APD and a Geiger-mode APD, and the corresponding responses to a single photon. Image: MIT Lincoln Laboratory.

If the magnitude of the reverse-bias voltage is below a value known as the breakdown voltage, collection wins the competition, causing the population of electrons and holes to decline (see figure 3.16 middle). The average number of electron-holes that is created by an absorbed photon, the gain, is typically tens or hundreds. Because the average photocurrent is strictly proportional to the incident optical flux, this mode of operation is known as **linear mode**.

When the reverse bias exceeds the breakdown voltage, the electrons and holes multiply by impact ionization faster, on average, than they can be extracted. This mode of operation is known as **Geiger mode** (see figure 3.16 right). The population of electrons and holes in the high-field region and the associated photocurrent grow exponentially in time. The Geiger mode allows obtaining a large output by means of the discharge even when detecting a single photon. Once the Geiger discharge begins, it continues as long as the electric field in the APD is maintained.
If there is series resistance in the diode, the rate of growth of the avalanche slows down. Ultimately, a steady-state condition is reached, where the generation and extraction rates balance. At this point the current neither grows nor decays. The avalanche causes the diode current to grow to some

resistance-limited value. Shutting off the avalanche current is called quenching; the capacitance is discharged until it is no longer above the breakdown voltage, at which point the avalanche dies out.

There are two main **differences between linear and Geiger mode**. In linear mode, the gain fluctuates because the impact ionization is a statistical process. This fluctuation produces multiplication noise which gets progressively worse as the average gain of a particular diode is increased by raising the reverse bias. In Geigermode the concept of multiplication noise does not apply. The total number of electron-hole pairs produced is fixed by the external circuit, not by the statistics of impact-ionization. In Geiger mode we are concerned with detection probability. This probability is the product of the quantum efficiency (the probability that the photon will be absorbed in the active region), and the avalanche probability (the probability that the electron or hole will initiate an avalanche that does not terminate prematurely).
Another important difference is that a particular Geiger-mode detection event does not give intensity information. The electrical pulse produced by the detection of a photon is indistinguishable from that produced by the detection of many simultaneously absorbed ones.

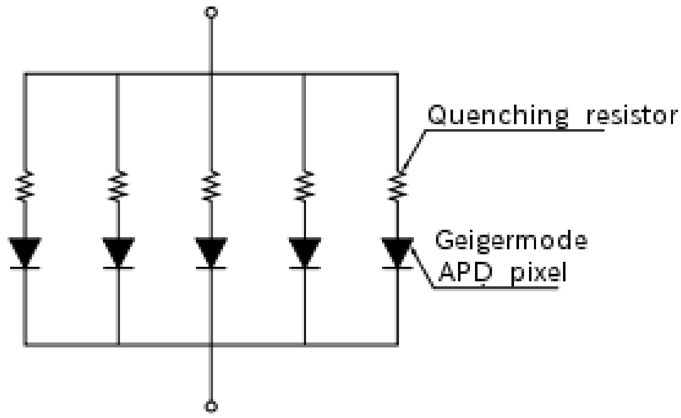

Figure 3.17: Block diagam of an MPPC, consisting of an array (or matrix) of APDs. Image: HAMAMATSU.[46]

An **MPPC** is an array of many Geiger-mode APDs, each one being a pixel (see figure 3.17). Every pixel outputs a pulse at the same amplitude when it detects some number of photons. The pulses generated by multiple pixels are superimposed onto each other, such that the MPPC outputs a signal whose amplitude equals the height of the superimposed pulses.

The emission of photons, while discharging the device, introduces **crosstalk**; the photons from one APD can trigger avalanches in others. Because the number of photons emitted is proportional to the amount of charge traversing the junction during the discharge, the crosstalk can be minimized by minimizing the parasitic capacitance that the APD must discharge.

The MPPC gain is **temperature dependent** (see figure 3.18). As the temperature rises, the crystal lattice vibrations become stronger, which increases the proability that carriers strike the crystal before the accelerated carrier energy has become large enough. This makes it difficult for ionization to occur. To remedy this, the reverse voltage should be increased to enlarge the internal electric field. To keep the gain constant the reverse voltage must

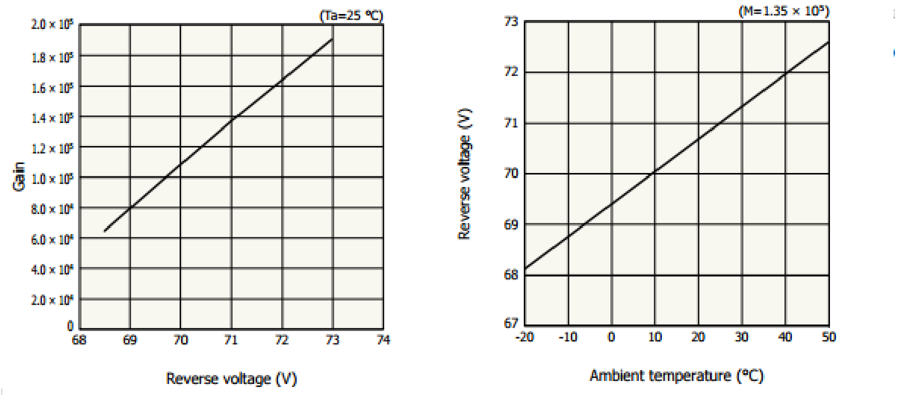

Figure 3.18: Left: gain versus reverse voltage. Right: reverse voltage versus ambient temperature. Image: HAMAMATSU.[46]

be adjusted to match the ambient temperature or the element temperature must be kept constant.
In the experiment, that will be described in chapter 4, it turns out to be difficult to control the temperature and to adjust the gain appropriately. The temperature variations have a considerable influence on the light yield.

4

EXPERIMENTAL OBSERVATIONS OF PHOTON DETECTION

4.1 EXPERIMENTAL SETUP

To get familiar with the SoLi∂ detector, and to optimize its performance, a unit cell of the detector is investigated experimentally. The testbench consists of a scintillating cube that is wrapped in a reflective material (see figure 4.1 insert). A single cladded WLS fiber, with a length of 90cm and widths of 3mm runs through a groove in the cube. At one fiber-end, a Hamamatsu MPPC (S12572-050P) with a breakdown voltage of 65 ± 10 V and a photosensitive area of 3×3mm registers the outgoing photons. At the other fiber-end a mirror is attached.
The MPPC is coupled to an electronics board, which is powered by two power supplies (see figure 4.1). One power supply is used to amplify the signal, while the other one puts a reverse bias of 2,6 V on the MPPC. The power supplies have a resolution of 10 mV and a stability of 5 mV.

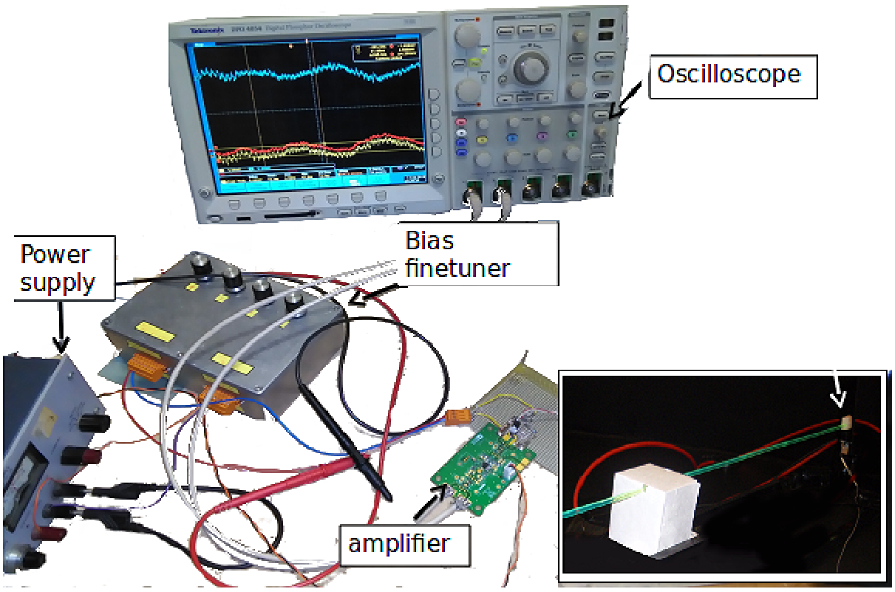

Figure 4.1: The optical testbench, consisting of a unit cell of the SoLi∂ detector, in the form of a wrapped scintillator cube with a fiber, attached to an MPPC and an electronics board.

A radioactive source is placed on top of the scintillator cube, whose emitted gamma rays will trigger the scintillation process. The source ^{60}Co is being used.
After the outputsignal of the MPPC is amplified and shaped, it is displayed by the oscilloscope. The oscilloscope is used to trigger data taking. When a signal above a specified amplitude is registered, the data are stored for processing.

In order to control the different contributions to the noise on the signal, the components of the setup are connected in sequence. A component should not change the kind of distribution of the noise, which is Gaussian. However, the noise will worsen with every added component, i.e. the amplitude of the signal will increase. This corresponds to an increase in the width of the distribution. The mean of the noise distribution always lies on 0 V. However, this is not seen on the measurements, as the oscilloscope could not set this point exactly.
The data that are presented in the following sections are smoothened by taking a running mean of 4 successive points. That is, every datapoint is replaced by the mean of four neighbouring points.

Initially, neither an MPPC or a cable is connected to the amplifier. The noise is due only to the electronics board and the oscilloscope. We take data that does not contain high amplitude peaks - the data is purely noise (see figure 4.2 left, on the next page). The histogram of the amplitudes of the noise follows a Gaussian distribution with a width of $\sigma = 0,36$mV (see figure 4.2 right). The standard deviation on this -and the following measurements of the width is $0,01$mV.

Connecting a cable of $3,5$m to the board, renders a width of $\sigma = 0,48$mV, which is an increase of 33% (see figure 4.3). The shorter the cable, the better the noise, so in the following experiments we will use a cable of 10cm. In the actual SoLi∂ experiment, this will not be free to choose as the data from a lot of MPPCs has to be brought together with cables.
The MPPC was directly connected to the 10cm cable so a measurement without MPPC was not possible for that cable length.

When connecting an MPPC to the cable, high amplitude peaks start to show on the data, due to the firing of pixels in the MPPC. The MPPC is placed in a black box, such that light cannot trigger the MPPC. The counts could be due to thermal agitation, hence referenced to as dark counts. To study the noise on the data, only the data below the treshold of one pixel avalanche are regarded. The reversed bias over the MPPC is initially 1,6V. The width of the noise distribution is then $\sigma = 0,45$mV (see figure 4.4).

The reversed bias on the MPPC is gradually increased to the optimal value of $2,6 \pm 0,01$V. The width is now $\sigma = 0,46 \pm 0,1$ mV (see figure 4.5).

Next, the MPPC is attached to the fiber that runs through the scintillating cube. To begin with, no radioactive source is put on top of the cube. Other ionising particles can give scintillation signals, but in the small time window of 100ns in which the data is taken, this is not very probable; the data are similar to the case where the MPPC was not connected to the fiber. For the noise we get $\sigma = 0,50$ mV (see figure 4.6).

Finally, the radioactive gamma ray source ^{137}Cs is put in the vicinity of the scintillation cube. The noise gets a width of $\sigma = 0,50$ mV (see figure 4.7).

After putting together all the components, the noise increased from $0,36$mV to $0,50$mV. This is an increase of 39%. Connecting a cable of $3,5$m between the electronics and the MPPC, as has to be done for the SoLi∂ detector, adds another $\sim$ 33% to the noise.

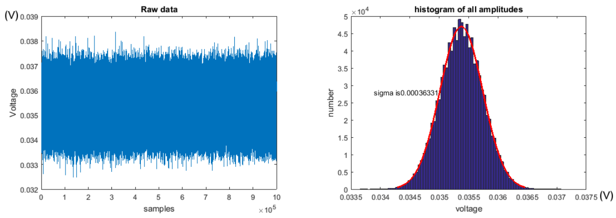

Figure 4.2: without an MPPC or cable.

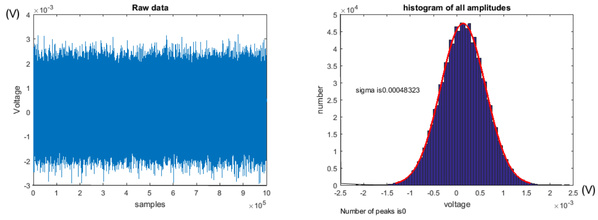

Figure 4.3: without MPPC and with a $3,5m$ cable.

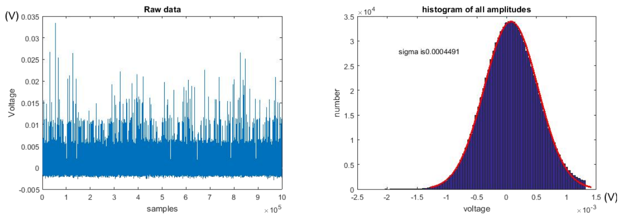

Figure 4.4: with MPPC and 10cm cable, under 1,6V.

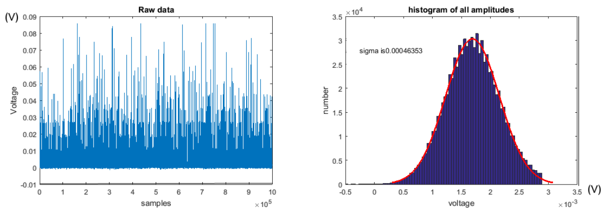

Figure 4.5: with MPPC and 10cm cable, under 2,6V.

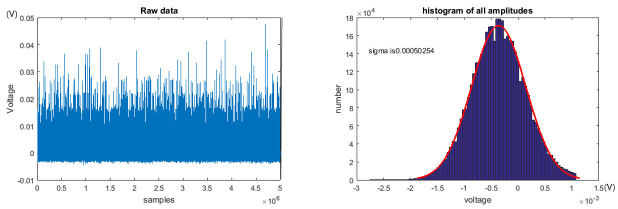

Figure 4.6: with MPPC and 10cm cable, under 2,6V, attached to the fiber in the cube.

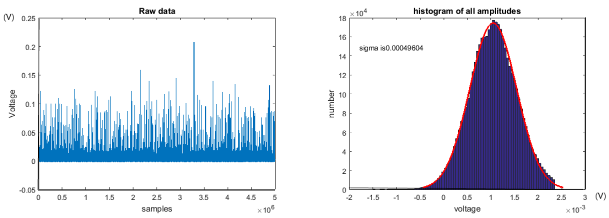

Figure 4.7: with MPPC and 10cm cable, under 2,6V, attached to the fiber and with a radioactive source.

The measurements have to be corrected for crosstalk between the pixels in the MPPC, where the signal in one pixel causes an adjacent pixel to fire as well (see 3.1.4 on page 41). To this end, the dark counts are measured, by putting the MPPC in a black box, isolated from radiation. Signals are triggered with a treshold below one pixel avalanche. An optimal reversed bias of $2,6$V is applied.
Peaks are identified in the data (see figure 4.8 left) and their amplitudes are set in a histogram (right). The consequent peaks in the histogram correspond to more and more pixel Avalanches. At a reversed bias of $2,6$V, the probability for cross talk is 0.3, according to the datasheet from the manufacturer.[49]

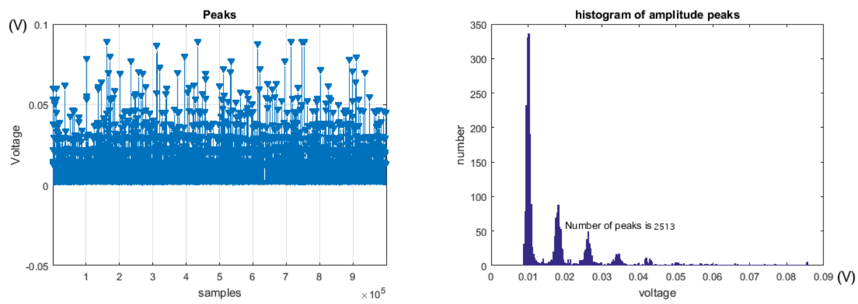

Figure 4.8: Left: identification of peaks in the measured data. Right: histogram of the amplitude of the datapeaks.

A measurement with the oscilloscope takes 1M = 10^6 samples, at a rate of 250M Samples per second. Thus there are 4 milliseconds between consecutive samples. There are about 7000 peaks in one measurement. This means there are 750 000 datapeaks per second that are due to darkcount (we say "datapeaks" to make the distinction with the peaks in the histogram).
Multiplying the number of datapeaks by the probability for cross talk, P_{ct}, gives the number of *at least* 2 pixel avalanches; multiple cross talks could have occured. Multiplying again by P_{ct} gives the number of *at least*3 pixel avalanches (pA), and so on.

$$P_{ct} \times \#_{datapeaks} = \#_{atleast2pA} \tag{4.1}$$
$$P_{ct} \times P_{ct} \times \#_{datapeaks} = \#_{at\ least\ 3pA} \tag{4.2}$$
$$\ldots \tag{4.3}$$

Subtracting the *at least* $3pA$ from the *at least* $2pA$ gives the number of times there are *exactly* $2pA$. This number corresponds to the counts in the second peak of the histogram.

$$\#_{exactly\ 2pA} = \#_{at\ least\ 2pA} - \#_{at\ least\ 3pA} \tag{4.4}$$
$$\ldots \tag{4.5}$$

By applying this reasoning to all the higher number of pixel avalanches, we can calculate how many counts did not end up in the first peak that corresponds to 1 pA. Subtracting this number from the total number of counts gives the number of counts thad did end up in the first peak.

$$\#_{exactly\ 1\ pA} = \#_{datapeaks} - \sum_i \#_{exactly\ i\ pA} \tag{4.6}$$

Now we know how many counts are expected for every peak, at a specific reversed bias.

The reversed procedure is also possible, that is calculating from the number of counts in every peak the probability for cross talk. In the following equation, P_{ct} is the only unknown.

$$\#_{exactly\ 1\ pA} = P_{ct} \times \#_{peaks} - P_{ct}^2 \times \#_{peaks} \tag{4.7}$$
$$\#_{exactly\ 2\ pA} = P_{ct} \times \#_{exactly\ 1\ pA} - P_{ct}^2 \times \#_{exactly\ 1\ pA} \tag{4.8}$$
$$... \tag{4.9}$$
$$\#_{exactly\ n+1\ pA} = P_{ct} \times \#_{exactly\ n\ pA} - P_{ct}^2 \times \#_{exactly\ n\ pA} \tag{4.10}$$

However, these are all quadratic equations. The way out, is to apply a property of an exponential decaying function e^{-x}. Namely, it does not matter whether you compare the value at x_1 with the value at x_2, or all the values above x_1 with all the values above x_2. The ratio stays the same. So to calculate P_{ct}, do

$$P_{ct} = \frac{\#_{exactly\ 2\ pA}}{\#_{exactly\ 1\ pA}} \tag{4.11}$$

Using the previous formulas, we find for the 2513 ± 100 datapeaks in the measurement, the results in table 4.1.

Table 4.1: Comparison between the expected -and measured number of pixel Avalanches in the MPPC.

Number of pA	Expected counts for at least n pA	Expected counts for exactly n pA	Measured counts in n pA	measured P_{ct}
2 pA	753,90	527,73	547±10	0,233±0,011
3 pA	226,17	158,32	215±10	0,393±0,019
4 pA	67,85	47,46	120±10	0,548±0,054
5 pA	20,36	20,356	42±10	0,350±0,089
1 pA		1444,72	1425±50	

The error on the final value is calculated with the error propagation formula

$$s_f = \sqrt{\left(\frac{\partial f}{\partial x}\right)^2 s_x^2 + \left(\frac{\partial f}{\partial y}\right)^2 s_y^2 + ...} \tag{4.12}$$

The sum of the measured counts is 2349 so we still miss some datapoints. They lie at higher values, where peaks of pixel avalanches can't be distinguished anymore. The prediction for 1 pA is very close to the measured value. There are less 2 and 3 pixel avalanches than expected, and more 4 and 5 pA than expected. This is due to the fact that several pixels can fire at the same time, triggered randomly by thermal agitation. The probability for cross talk superimposed on this number.

To get some statistics, we calculated the cross talk for different measurements (see table 4.2).

The total mean of the probabilities P_{ct} in table 4.2 equals **0,2947** $\pm\, 0,0039$. This is very close to the indicated value of the probability for cross talk which is 0,3.

Table 4.2: Multiple measurements to determine the cross talk probability.

P_{ct} from	Data with $s_{data} = \pm 0,015$					mean
1 pA to 2 pA	0,2163	0,2571	0,2649	0,2259	0,2773	$0{,}2483_{\pm 0{,}0067}$
2 pA to 3 pA	0,3276	0,2485	0,2613	0,3153	0,277	$0{,}28594_{\pm 0{,}0067}$
3 pA to 4 pA	0,3516	0,3945	0,3218		0,3263	$0{,}28594_{\pm 0{,}0067}$

4.4 CORRECTIONS FOR THE TEMPERATURE

The temperature (T) has an influence on the gain of the MPPC (see figure 3.18 on page 44). The signal is amplified more, when the temperature is higher. The reversed bias can correct for a shift in the temperature.

$$V_{rev\ bias} = (25°C - T) \times 0,060V/°C \tag{4.13}$$

A thermometer is placed inside the black box. At the beginning of every measurement, the bias is corrected with respect to the temperature. However, some measurements are executed overnight, without intermediate corrections for the temperature variations.

4.5 DATA ACQUISITION

A radioactive source is placed on top of the wrapped scintillator cube. Gamma rays from the source excite the scintillator which emits photons at deexcitation. Some photons are collected in the WLS fiber and transported to the MPPC where they cause bursts of pixel avalanches.
The oscilloscope triggers on peaks of at least 15mV. The acquisition saves 1000 sample points around the peak, which corresponds to 20 microseconds of data (see figure 4.9 right). This is sufficient data since we are only interested in the large peak caused by the gamma ray. Moreover, More sample points are possible but this lengthens the peak finding process.

The amplitudes of the peaks in the measured data are collected in a histogram. The ^{60}Co source has photopeaks at 1173keV and 1333keV, but we cannot distinguish them. This gives the spectrum in figure 4.9, left. 15000 Acquisitions of 1000 points (50 MS/s) were taken with the trigger on 15 mV and a reversed bias of 1,456V.

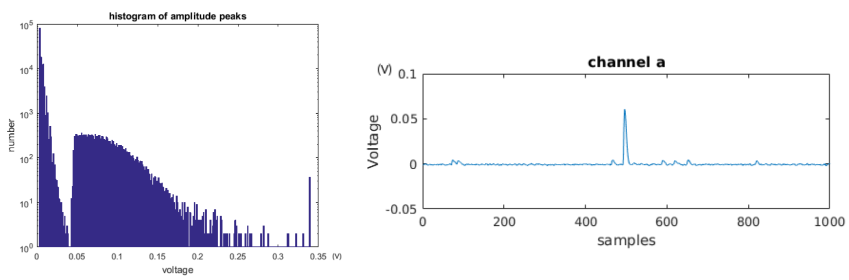

Figure 4.9: Left: Histogram of the amplitudes of the signal peaks, caused by a ^{60}Co source in a scintillating cube and measured by an MPPC. Right: Data acquirement, consisting of 1000 datasamples. The center peak is a signalpeak, while the small peaks are dark counts.

The distribution at higher voltages is due to the the gamma rays of the source. The distribution contains the signal, convoluted with the probabilities for crosstalks.
At lower voltages, dark counts can be distinguished. They are grouped in several equidistant peaks, corresponding to the the different number of pixel avalanches induced by cross talk. The dark counts enter the measurement, as they lie within the 1000 sample point around the signal peak. On average, 3 dark count peaks are introduced with every signal peak.

The signal peak has to be discriminated from the dark counts. The amplitude of the signal should be enlarged, without affecting the darkcounts, or the dispersion on the signal should be narrowed.
The factors that have an influence on these quantities are:

1. collection efficiency: the share of photons that are emitted in the scintillator and reach the MPPC via the fiber. This efficiency turns out to be low; only 2% of the photons reach the MPPC.
2. quantum efficiency: the share of photons that strike the MPPC and effectively induce a signal. This factor can't be adjusted by our means.
3. The conversion efficiency: the dispersion of the number of pixels that will fire when a pixel is triggered. This quantity is influenced by the cross talk. Cooling the setup would improve this efficiency drastically.

To make advantage of the last factor, the SoLi∂ detector will be cooled down to 5°C. This will suppress the darkcounts and the cross talk. It will render the detector single-photon sensitivity. This decision was made after different attempts showed that the dark counts cannot be reduced by statistical means or based on their characteristics. They are indistinguishable from the signal. One of the attempts is described in the following.

4.6 REDUCING DARK COUNTS - COINCIDENCE PEAKS

One of the investigated improvents for the darkcounts, is adding the signals of two independent MPPCs, one at each end of the fiber. This could double the amplitude of the signal, while keeping the amplitude of the darkcounts the same. The number of darkcounts would double, but the distribution of its amplitudes would stay at the far left of the histogram, while the amplitude of the signal shifts to the right. That is, the signal peaks would coincide for both MPPCs, while the peaks of the darkcounts would not.

Comparing measurements of the darkcount from one MPPC with two MPPCs, shows that the number of darkcounts with a certain amplitude not just doubles, as we had hoped. The darkcounts often coincide. New peaks, that correspond to multiple pixels firing, appear (see figure 4.10).

With one MPPC, there are 909 darkcounts above a treshold of 1,5 pA (i.e. 0,015V). For two parallel MPPCs there are 2653 darkcounts above the treshold. We do not just find the double number of peaks, as if the surface of the MPPC doubled, but the result gets even worse; Adding the noise of the two MPPCs can yield new peaks above the treshold. This method is not effective at discriminating the dark counts.

Other ways to eliminate the darkcounts were investigated, but none gave substantial improvements. The dark counts are a drawback of the experiment that have to be taken into account. The darkcounts prevent the experiment to reach single-photon-sensitivity.

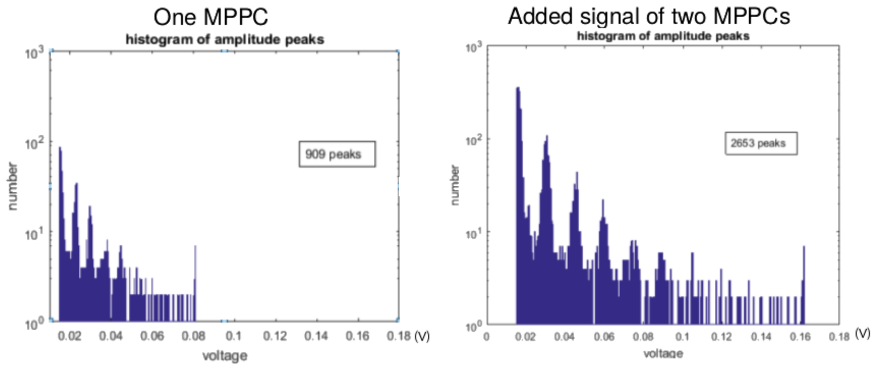

Figure 4.10: Histograms of the amplitude of darkcounts, on the left for one MPPC and on the right when two MPPCs are connected to the fiber. For the latter, the amplitude of the dark counts and their number increases.

4.7 SYSTEMATIC UNCERTAINTIES

The reproducibility of the experiment was studied by repeatedly dismantling and reassembling different parts of the setup. A tedious job that has to be done. We studied

1. Opening and conceiling the black box,
2. Moving the cube inside the box,
3. Moving the gamma ray source on the face of the cube,
4. Attaching the MPPC to the fiber with tape or glue,
5. Resetting the reversed bias voltage,
6. Connecting the cables.

As reference point, the Compton edge (see next section) was chosen. The position of the Compton edge varied with ±10 mV between different measurements.

4.8 THE COMPTON EDGE

A gamma ray that traverses the scintillator cube, will deposit all or part of its energy in the scintillator. When the gamma ray is absorbed completely, the energy of the emitted photons will be equal to the energy of the initial ray. However, part of the energy can escape the detector. In the case of Compton scattering on a particle, the energy transfer will depend on the angle at which the gamma ray is dispersed, from grazing the particle to a head-on collision. Additional Compton scatterings can occur such that more energy is recovered, but part of it will escape the detector. In the histogram of the amplitudes of the photopeaks, a declining flank is generated by the Compton scattering. This is the Comptonedge (see figure 4.9).

As indication on the performance of the light yield, the center of the Compton edge is measured. To this end, a fit with a complementary error function, $erfc$ is performed on the Compton edge.

$$erfc(z) = \frac{2}{\sqrt{\pi}} \int_z^{\infty} e^{-t^2} dt. \tag{4.14}$$

The fit has parameters a, b, c and A and is of the form

$$fit = A \cdot (sqrt(ax) - b) + c. \tag{4.15}$$

The center of the $erfc$ lies on

$$center_{erfc} = b/a. \tag{4.16}$$

For a good light yield, the center has to be as large as possible, since this corresponds to a high signal peak and the best discrimination from the dark-counts.

Cubes of different material, polishing, cutting and size are compared. The measurement is done with the ^{60}Co source. Data taking, consisting of 1000 samplepoints, is triggered on peaks above 30 mV. A fit with a complementary error function is performed and the center of the edge indicated. The measurements contain data from 1000 acquirements (including the peak that triggers data taking and 1000 surrounding samplepoints).

In the following, measurements that are grouped together are taken under approximately the same circumstances. Only graphics from one group ought to be compared.

The reproducibility of the measurements was determined to be $\pm 0,01$ V. This is often in the order of magnitude of the differences we wish to determine.

4.9.1 *Cutting of the cube*

Different procedures are available to cut sheets of scintillating material in cubes. With a water jet that contains small sand grains, the cubes can be frazed out. Different sizes of sand grains, result in different outcomes. The cubes can also be cut out with a cutting machine. Measurements of the different cuttings are shown in figure 4.11.
The watercuts 1, 2 and 3 are slightly worse than the machine cut.

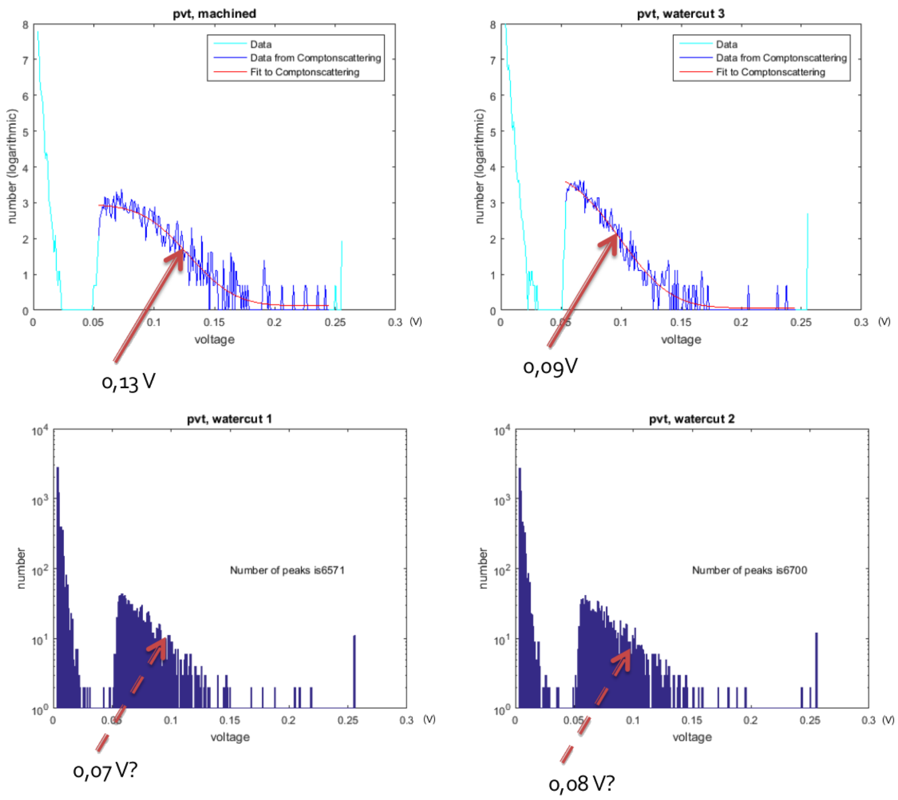

Figure 4.11: Different cutting procedures for the cubes.

4.9.2 *Polishing of the cube*

The faces of the cube can be polished with a rotating wheel, abrasive cloth and polishing paste. The results before and after polishing are shown in figure 4.12. In both cases, the cube is wrapped in tyvek and 1000 acquirements are taken.
The polished cube seems slightly better than the matt cube, with $0,16\text{V}$ to $0,14\text{V}$. But the difference is close to the limit of sensitivity of $0,01\text{V}$.

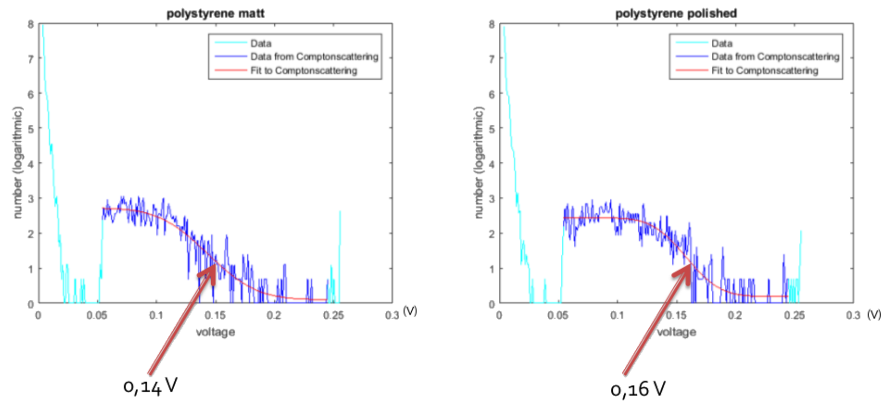

Figure 4.12: Measurement of the cube before and after polishing.

4.9.3 *Coupling of the MPPC to the fiber*

Optical grease is smeared on the fiberend before the MPPC is attached to it. The optical grease increases the coupling from the fiber to the MPPC. However, the light yield does not increase noticeable (see figure 4.13).

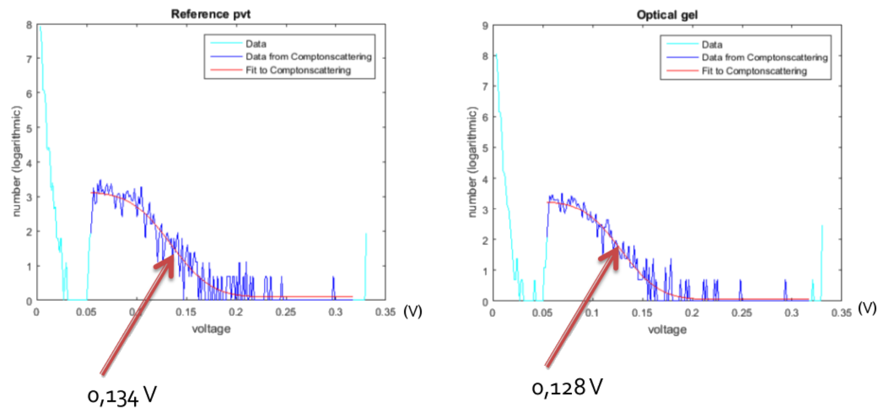

Figure 4.13: Measurements to invstigate the influence of optical gel at the coupling of the MPPC to the fiber.

4.9.4 *Wrapping of the cube*

One and the same cube is put in different wrapping materials. We use tyvek, alufoil and no wrapping at all. Again 1000 acquirements are taken. The tyvek gives better light yield than the alufoil and no wrapping.

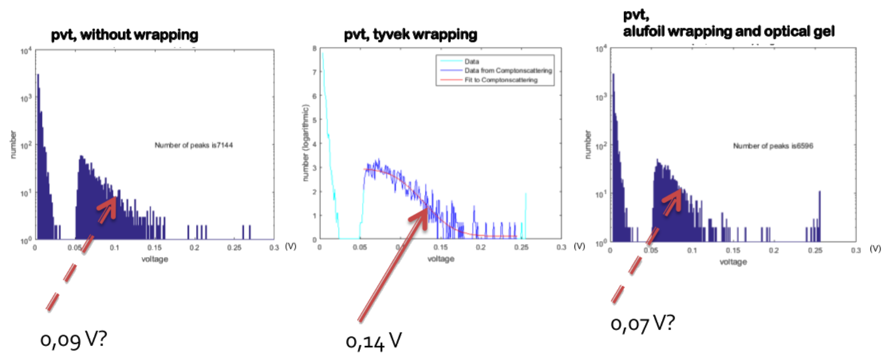

Figure 4.14: Measurements with different wrappings around a cube.

Two different thicknesses of tyvek are compared, namely 75 g/m^2 and 118 g/m^2. We see a distinct increase of the light yield when the thick tyvek is used (see figure 4.15). The signal improves from $0,12$V to $0,22$V, which is confirmed by repeated measurements.

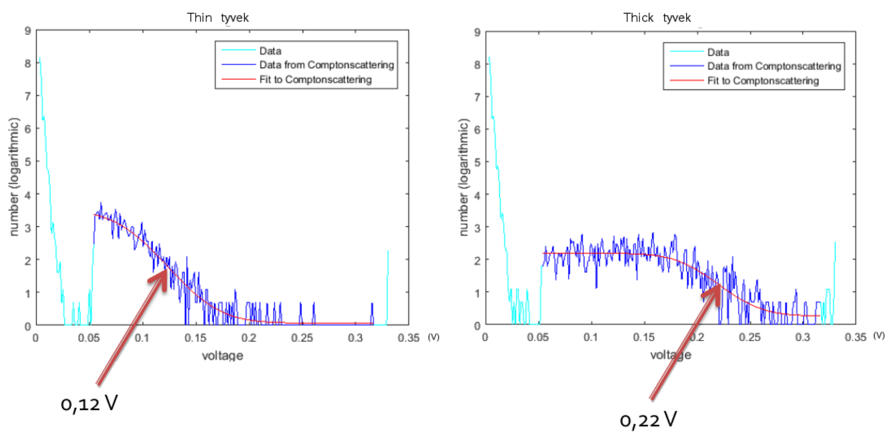

Figure 4.15: Comparing different thicknesses of the tyvek.

4.9.5 *Roughness of the groove*

The roughness of the groove is increased with sand paper. The measurements in figure 4.16 show no significant differences, at best a small decrease in performance.

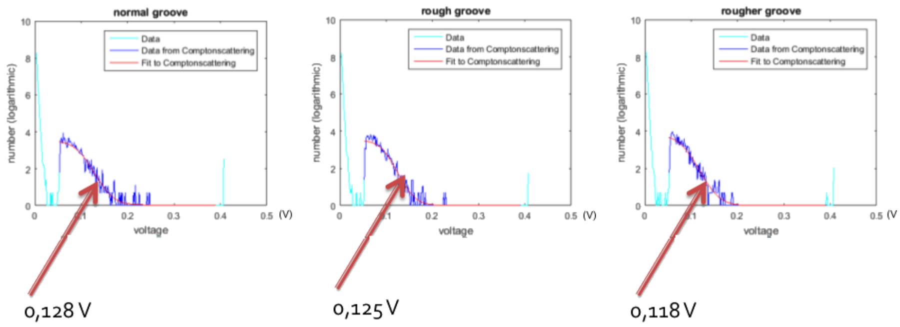

Figure 4.16: Comparing the different roughnesses of the groove in the scintillatorcube.

4.9.6 *Roughness of the hole*

Different drill bits were used to create different holes through cubes with visually different roughnesses. Again, no significant difference was observed between the measurements (see figure 4.17). When comparing these measurements with the measurements of the groove, we see a small increase in performance. However, these changes fall within the limit of sensitivity.
Note: the lightyield is higher for this measurement than for the foregoing, but this is due to the fact that the thick tyvek was used (see section 4.9.4).

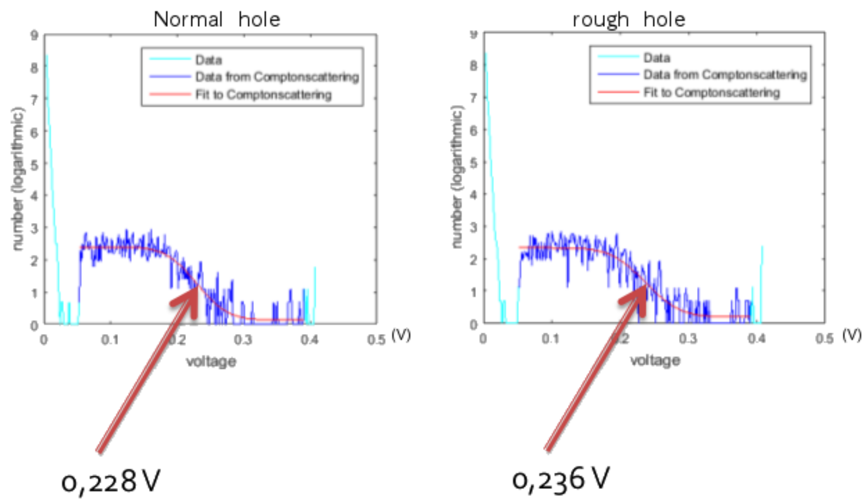

Figure 4.17: Comparing the different roughnesses of the hole through the scintillatorcube.

4.10 CONCLUSIONS ON THE EXPERIMENT

The influence of different parameters on the lightyield of the experimental setup, described in section 4.1 on page 45, were examined. As indication on the performance of the lightyield, the center of the Comptonedge was regarded (see section 4.8, page 52). The standarddeviation on the measurement is 0,015V, due to the constraint on reproducability (see section 4.7), the challenging monitoring of the temperature and the statistical uncertainty. The findings are listed in table 4.3.

Table 4.3: Experimental results for the investigation of different parameters on the light yield of the setup, measuring a ^{60}Co source.

Parameter	Option	Comptonedge (∼ lightyield)	deviation
cutting	machined	0,013 V	0,015 V
	watercut 1	0,09 V	0,015 V
	watercut 2	0,07 V	0,015 V
	watercut 3	0,08 V	0,015 V
polishing	matt	0,14 V	0,015 V
	polished	0,16 V	0,015 V
coupling	aircoupling	0,134 V	0,015 V
	optical gel	0,128 V	0,015 V
wrapping	no wrapping	0,09 V	0,015 V
	alufoil	0,07 V	0,015 V
	thin tyvek	0,14 V	0,015 V
	thick tyvek	0,22 V	0,015 V
roughness groove	normal groove	0,128 V	0,015 V
	rough groove	0,125 V	0,015 V
	rougher groove	0,118 V	0,015 V
roughness hole	normal hole	0,228 V	0,015 V
	rough hole	0,238 V	0,015 V

According to the measurements, a machined cube, with polished faces and wrapped in thick tyvek renders the best light yield. The coupling of the MPPC to the fiber and the roughness of the groove or hole where the fiber runs through, do not have a significant influence.
Especially the tyvek has a worthwhile and cost efficient improvement on the lightyield.

4.11 MEASUREMENTS AT THE LAL-LABORATORIES IN ORSAY

At the Laboratoire d'Acc*é*l*é*rateure L'in*é*aire (LAL), similar studies on the light yield of the optical components from the SoLi∂ detector were performed.[50] They used a more dedicated test bench, being the official lightyield experiment for the SoLi∂ experiment, which makes their results more accurate than mine. That is why they are listed in the following and used to tune the parameters in the simulation of the optical components (see section5.6.2 on page 94).

The testbench at LAL is also composed of a scintillator cube, a reflective wrapping and a WLS fiber with two MPPCs (see figure 4.18). The MPPCs have a reversed bias of $1,5$V.
A Bismuth source, ^{207}Bi, is used to provide a mono-energetic electron signal, which is accompanied by γ-rays. The gamma ray triggers the data taking and the electron deposits 1 MeV in the scintillatorcube. The external trigger is made of a thin BC-400 scintillator of 110 μm, 2 light guides and 2 photo-

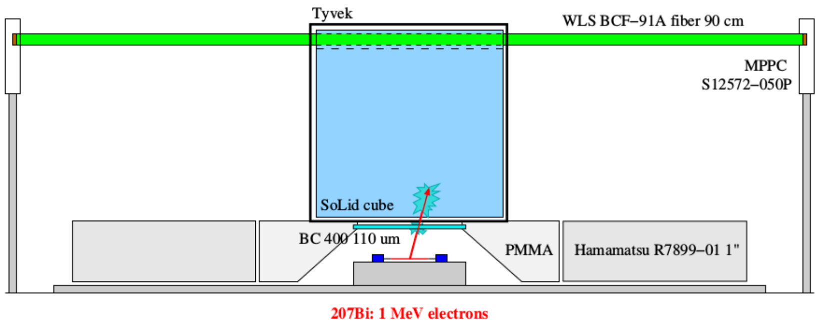

Figure 4.18: Schematic view of the LAL-testbench with the source in pink, the external trigger in darkgreen, the SoLid type scintillator in blue and fiber in light green. Image: LAL.

multiplier tubes (PMT) from Hamamatsu (R7899-01 1), is being used. Data taking is triggered in coincidence between the 2 PMT at -5 mV.

The measurements are corrected for crosstalk, taking a 17% crosstalk probability which is suited for the reversed bias of 1,5V. The lightyield is indicated as the sum of Pixel Avalanches of both MPPCs in the standard setup. In the following, the measurements presented in the same table have been done the same day, at the same temperature and the same voltage to lower the systematic uncertainties. The systematic uncertainty was determined to be 5% of the measured value and will be indicated as subscript.

To start with, a reference measurement of the standard configuration is taken. One thin tyvek wrapping and a multi cladded fiber with two MPPCs at the ends is used.

Table 4.4: Reference measurement of the SM1 configuration.

Measurement	PA in 1 MeV	$\frac{measurement}{reference\ measurement}$
Referece	$21{,}3_{\pm 1{,}1}$	1

The performance of a cube, before and after polishing the faces, is studied. The roughness average is indicated with R_a. This parameter characterizes the surface, based on the vertical deviations of the surface profile from the mean line, y_i, as indicated by the red arrow on figure 4.19.

$$R_a = \frac{1}{n}\sum_{i=1}^{n}|y_i|\,. \tag{4.17}$$

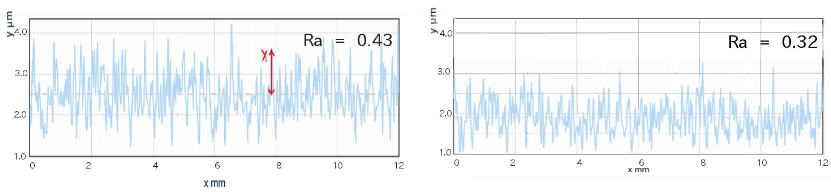

Figure 4.19: Schematic view on the transition of the Roughness Average R_a. Image: Prof. Abbott, online Surface Profile Explorer.

If the deviations are large, the parameter R_a is large and the surface is rough. The roughness of the cube before and after polishing is respectively $0,429\mu$m and $0,321\mu$m. The difference is shown in figure 4.19.
The measurement is done in the standard configuration with 1 multi cladded fiber and a thin tyvek wrapping. The results are shown in table 4.5. Polishing seems to improve the light yield but the results lie within the systematic uncertainties.

Table 4.5: Measurements with different polishing.

	Before polishing		after polishing	
Measurement	R_a (μm)	PA in 1 MeV	R_a (μm)	PA in 1 MeV
Measurement 2	0,449	$21{,}8_{\pm 1,1}$	0,385	$22{,}4_{\pm 1,2}$
Measurement 3	0,429	$11{,}0_{\pm 0,6}$	0,321	$11{,}6_{\pm 0,6}$

Cubes with holes are compared to cubes with grooves. The tests are done in the standard configuration. Results are listed in table 4.6. However, the cubes with holes are more polished than the other cubes, which probably explains the increase in light yield of 10%.

Table 4.6: Measurements on grooves and holes.

Measurement	PA in 1 MeV	$\frac{measurement}{reference\ measurement}$
2grooves	$21{,}8_{\pm 1,1}$	1
1 hole	$23{,}4_{\pm 1,2}$	1,08
2 holes	$24{,}0_{\pm 1,2}$	1,10
4 holes	$24{,}1_{\pm 1,3}$	1,10

At the faces of the cube, scintillating ZnS sheets can be placed that are used to detect the neutrons from the IBD reaction (see chapter 2). The experimental results can be found in table 4.7. We seem to loose around 10% of PA adding one more ZnS sheet.

Table 4.7: Measurements with ZnS sheets

Measurement	PA in 1 MeV	$\frac{measurement}{reference\ measurement}$
no ZnS	$21{,}1_{\pm 1,1}$	1
1 ZnS	$19{,}4_{\pm 1,0}$	0,92
2 ZnS	$17{,}4_{\pm 0,9}$	0,82
3 ZnS	$14{,}3_{\pm 0,8}$	0,6

The light yield from single and multi cladded fibers are compared (see table 4.8). We notice a good improvement of the light yield with multi cladding fibers of about 40 %.

Table 4.8: Measurements with different number of fiber claddings.

Measurement	PA in 1 MeV
single cladded	$15{,}6_{\pm 0,8}$
double cladded	$22{,}4_{\pm 1,2}$
double/single	$1{,}44_{\pm 0,08}$

Different wrappings for the cube in standard setup were tested, like teflon, paper or aluminised mylar (see table 4.9). As it looks like, having a thicker Tyvek would be the best solution (teflon is not easy to wrap thousands of cubes with).

Table 4.9: Measurements with different wrappings.

Measurement	PA in 1 MeV	$\frac{measurement}{reference measurement}$
thin tyvek (75 g/m^2)	$20{,}9_{\pm 1{,}1}$	1
thick tyvek (118 g/m^2)	$27{,}8_{\pm 1{,}4}$	1,33
thin aluminised mylar	$11{,}7_{\pm 0{,}6}$	0,56
thick aluminised mylar	$23{,}1_{\pm 1{,}2}$	1,11
teflon	$29{,}4_{\pm 1{,}5}$	1,41
paper	$13{,}8_{\pm 0{,}7}$	0,66

The impact of the number of Tyvek layers, in which the cubes are wrapped, are tested. The Tyvek is a reflector so adding more Tyvek should improve the reflectivity and thus the light collection. The results in table 4.10 show that adding one layer of Tyvek improves well the light collection but the improvements with more layers is smaller.

Table 4.10: Measurements with different numbers of tyvek layers.

Measurement	PA in 1 MeV	$\frac{measurement}{reference\ measurement}$
1 Tyvek	$20{,}9_{\pm 1{,}1}$	1
2 Tyvek	$25{,}2_{\pm 1{,}3}$	1,21
3 Tyvek	$27{,}9_{\pm 1{,}4}$	1,34
4 Tyvek	$27{,}8_{\pm 1{,}4}$	1,33

In the standard setup sticky mirrors are compared with aluminised mylar mirrors. At one end of the fiber there is an MPPC and on the other one is a mirror. Table 4.11 indicates that the aluminised mylar mirror reflects the light better (21 % more PA) than the sticky mirror. used in SM1.

Table 4.11: Measurements with different mirrors.

Measurement	PA in 1 MeV
sticky mirror	$20{,}8_{\pm 1{,}1}$
aluminised mylar mirror	$24{,}2_{\pm 1{,}3}$

5 SIMULATION OF PHOTON TRANSPORT -AND DETECTION

Next to the actual deployment of the SoLi∂ detector, a detailed simulation of the full-scale SoLid experiment is needed. All steps in the chain of the interaction and detection have to be modeled accurately. Including the antineutrino spectrum, the neutrino interactions with the BR2 reactor core and the detector, the inverse beta decay reaction, the background, the neutron difussion, the propagation and collection of the scintillation light and the response of the MPPC photodetectors. For this purpose a full software framework is being developed as a chain of a number of algorithms; this provides the capability of modifying any of them at any time, unaffecting the rest of the chain.

In the following we will focus on the simulation of the optical processes, using the GEANT4 simulation package. The optical simulation models the propagation of the scintillation photons from the PVT cubes through the WLS fibers to the detection mechanism. The simulation is based on the example of a WLS fiber from the GEANT4 toolkit. [1]

5.1 INTRODUCTION ON GEANT4

GEANT4 stands for **Ge**ometry **a**nd **T**racking and is a toolkit to simulate the passage of particles through matter with help of Monte-Carlo methods.[51] The package provides methods to simulate geometrical structures, including all involved materials with their properties, and to simulate the creation and tracking of most fundamental particles. The visualisation of detector parts and particle trajectories is provided. It is also possible to access data of all particles, interactions, volumes and the response of sensitive detector components at most points of the simulation run. GEANT4 can also perform basic histogramming with the use of external analysis tools.
The GEANT4 framework consists of several categories, which are summed in the following. The subsequent categories always make use of the former.

The **materials -and particles** category implements facilities to describe the physical properties of particles and materials for the simulation of particle-matter interactions.
The **geometry** module offers the ability to describe a geometrical structure and propagate particles efficiently through it.

The **track** category implements classes for tracks and steps, containing the path of the particles through the geometry. A Track is always a momentary representation of the state of a particle, while a step carries the intermediate information between two Track-points.
The **processes** category contains models of physical interactions of the particles.

The **tracking** category invokes the processes and manages their contribution to the evolution of a track's state and provides information in sensitive

[1] http://geant4.web.cern.ch/geant4/UserDocumentation/Doxygen/examples_doc/html/Examplewls.html

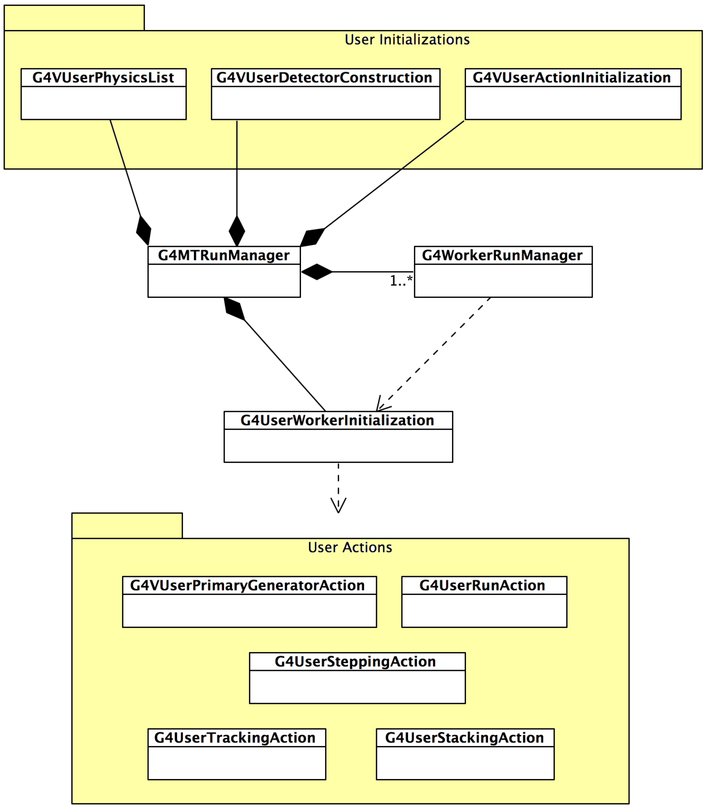

Figure 5.1: Class diagram for main run category classes. Image: Geant4 manual.

volumes for hits and digitization.

The **event** category manages events in terms of their tracks. Whereas the **run** category manages collections of events that share a common beam and detector implementation. A run is the largest unit of simulation. Within a run, the detector geometry, the set up of sensitive detectors, and the physics processes used in the simulation should be kept unchanged.

Finally, A **readout** category allows the handling of pile-up.

The full framework of these categories is implemented in GEANT4, in an object-oriented manner by the use of user classes. In the design of a large software system such as GEANT4, it is essential to partition it into smaller logical units. This makes the design well organized and easier to develop. Once the logical units are defined independent to each other as much as possible, they can be developed in parallel without serious interference. In GEANT4, there are two kinds of user classes, *user initialization classes* and *user action classes*. The former are used during the initialization phase, while the latter are used during the run (see figure 5.1).

All three user initialization classes are mandatory. They must be derived from the abstract base classes provided by GEANT4. GEANT4 does not provide default behavior for these classes. G4RunManager checks for the existence of these mandatory classes when the simulation is executed:

1. G4VUserDetectorConstruction requires the user to describe the experimental set-up, in a derivation of this class.

2. G4VUserPhysicsList requires the user to choose the physics that participate in the interactions of particles in matter.
3. G4VUserActionInitialization requires the initial event state, regarding the kind, number and initial properties of the primary particles (Primaries).

The user action classes include at least one mandatory user action class, namely PrimaryGeneratorAction. GEANT4 provides additionally five optional user action classes, that have several virtual methods which allow the specification of additional procedures at all levels of the simulation application.

4. G4VUserPrimaryGeneratorAction creates an instance of a primary particle generator
5. G4UserRunAction specifies actions that shall be executed at every start and end of every Run.
6. G4UserEventAction does the same as above but for every Event. Here information about the whole event can be gained.
7. G4UserStackingAction can suspend or postpone tracks if there are particle tracks with higher priority. (Mainly used for optimisation.)
8. G4UserTrackingAction Specifies actions at the creation and completion of every Track. Information about the particle track can be extracted here.
9. G4UserSteppingAction customises the behaviour while going from step to step in the simulation. Detailed information from every StepPoint can be obtained here.

Some components of the framework, relevant in the scope of this thesis, are described in the following sections in more detail.

5.2 GEOMETRY DEFINITION AND MATERIAL CHOICES

In the DetectorConstruction class, the user has to define all components of the detector. A detector geometry in GEANT4 is made of a number of volumes, including details about the chemical composition of the materials used, such that quantities like absorption length and energy loss in matter (Bethe-Bloch formula) can be computed. Here, properties for optical processes, like refractive index, attenuation length and reflectivity, can be set.

Regarding the study of the optical processes in the SoLi∂ experiment, the SoLi∂ detector is implemented with a flexible design. By means of several parameters the design can be adjusted to the specific needs of the user, within the range of the predetermined constraints. The basic components determine the flexibility of the final product and will be discussed in the following. The defining parameters will be indicated in *itallics*.

The center component of the detector is a **cube** that consists of a scintillating material. The material is set to G4_PLASTIC_SC_VINYLTOLUENE. The *size* of the cube is due to production constraints minimally 5 cm. The *surface roughness* can be adjusted from 1 (perfectly polished) to 0 (perfectly rough). Up to 6 *grooves or holes* can be put on a specified *position* in the cube. The *roughness of the groove* can be specified separately. The *number of cubes* that will be stacked into a matrix can be chosen, with minimally 1 cube in every direction and all cubes identical.

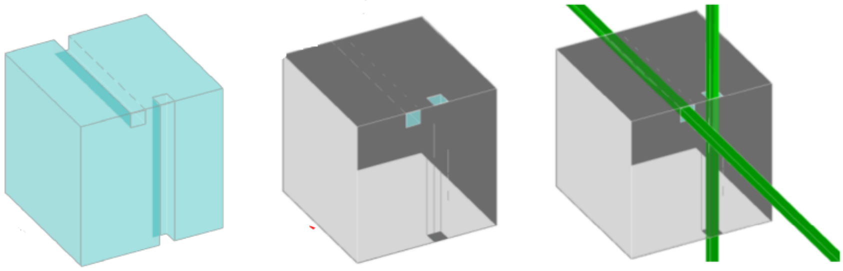

Figure 5.2: A scintillation cell with grooves, wrapped in a reflective tyvek layer, with two WLS fibers. Image: SoLi∂ Collaboration.

The cube can be wrapped in a reflective **tyvek layer**. The properties of the tyvek have been studied intensively (see section 3.1.2 of page 38) and have been incorporated in the GEANT4 toolkit. We use this predefined tyvek and superimpose an additional *transparency, reflectivity and absorption* coefficient, that have to add up to 1. Between the cube and the tyvek is an airgap, with adjustable *thickness*. The *number of tyvek* layers can be chosen.
In the grooves on the cube, **WLS fibers** can be placed that are identical.

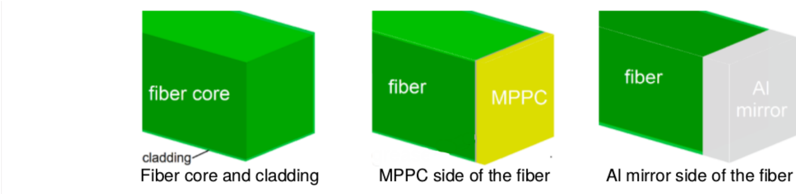

Figure 5.3: WLSfiber with cladding and mirror and/or MPPC on the ends. Image: SoLi∂ Collaboration.

The fiber can be coated with maximally 2 *coatings*, that each have a certain *roughness* and *thickness*. The widths of the groove are set to be the *x -and y size* of the fiber plus the thickness of the coating(s) plus an airgap of 0.1 cm. The *z-size* of the fiber can be chosen as well.

On each outer end of the fiber, a **detector or a mirror** can be placed. A minimum of 1 detector is mandatory. The detector is set on a certain *distance* from the fiber. The mirror has a *reflectivity* and *distance* to the fiber.

To detect the neutrinos, a *number* of ^{6}**LiF:ZnS(Ag) sheets** is placed on top the cube. The *thickness* of the sheets can be chosen.

A volume in GEANT4 has to be defined in three steps: First of all, a *Solid* must be created that contains all the geometrical information, i.e. the dimensions and shape of the volume. Then a *LogicalVolume* has to be defined, where physical characteristics are added to the geometrical solid, like the material of the volume, whether it contains any sensitive detector elements and the surfaceproperties. Finally a *PhysicalVolume* is created by placing the LogicalVolume inside a mothervolume, with a specified rotation and position. All volumes must have a mother volume, except of the world volume which is the basic volume. A short overview is shown in figure 5.4. The geometry information is used by the GEANT4 kernel while tracking particles.

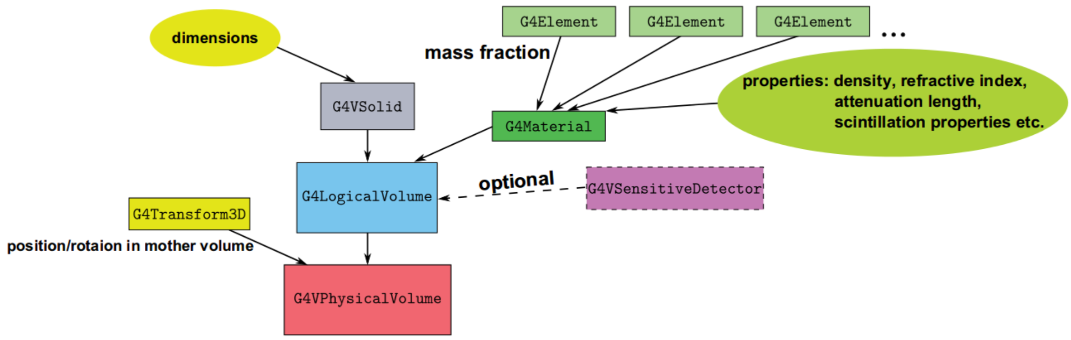

Figure 5.4: Diagram of the volume building in the GEANT4 DetectorConstruction. Image: GEANT4.

5.3 PHYSICAL PROCESSES

Physics processes describe how particles interact with materials. GEANT4 provides seven major categories of processes

1. Electromagnetic processes
2. Handronic processes
3. Transportation processes
4. Decay processes
5. Optical processes
6. Photoleptonhadron processes
7. Parametrisation processes

G4VUserPhysicsList is the base class for a mandatory user class, in which all physics processes and all particles required in a simulation must be registered. All physics processes are derived from the G4VProcess base class. Its virtual methods describe the behavior of a physics process.

In the scope of this thesis, there is special interest for physical processes that create and influence optical photons.

Three processes can **create** optical photons: Transition Radiation, the Cerenkov Process and the Scintillation Process.

The number of optical photons created in *transition radiation* processes is negligibly small.
Cerenkov light occurs when a charged particle moves through a medium faster than the group velocity of light in the medium.[52] Photons are emitted on the surface of a cone (see figure 5.6), and as the particle slows down the cone angle decreases, the emitted photon frequency increases and their number decreases. The number of optical Cerenkov photons N_γ created per length L by a particle that travelled through a dielectric material is

$$\frac{dN_\gamma}{dL} < 49 \sin\theta_C \; per\ mm, \tag{5.1}$$

with $\theta_C = \arccos \frac{1}{n\beta}$ the Cerenkov angle. For a 1 GeV muon traversing a typical scintillator with refractive index n=1.6 this number becomes

$$\frac{dN_\gamma}{dL} \approx 30 \; per\ mm. \tag{5.2}$$

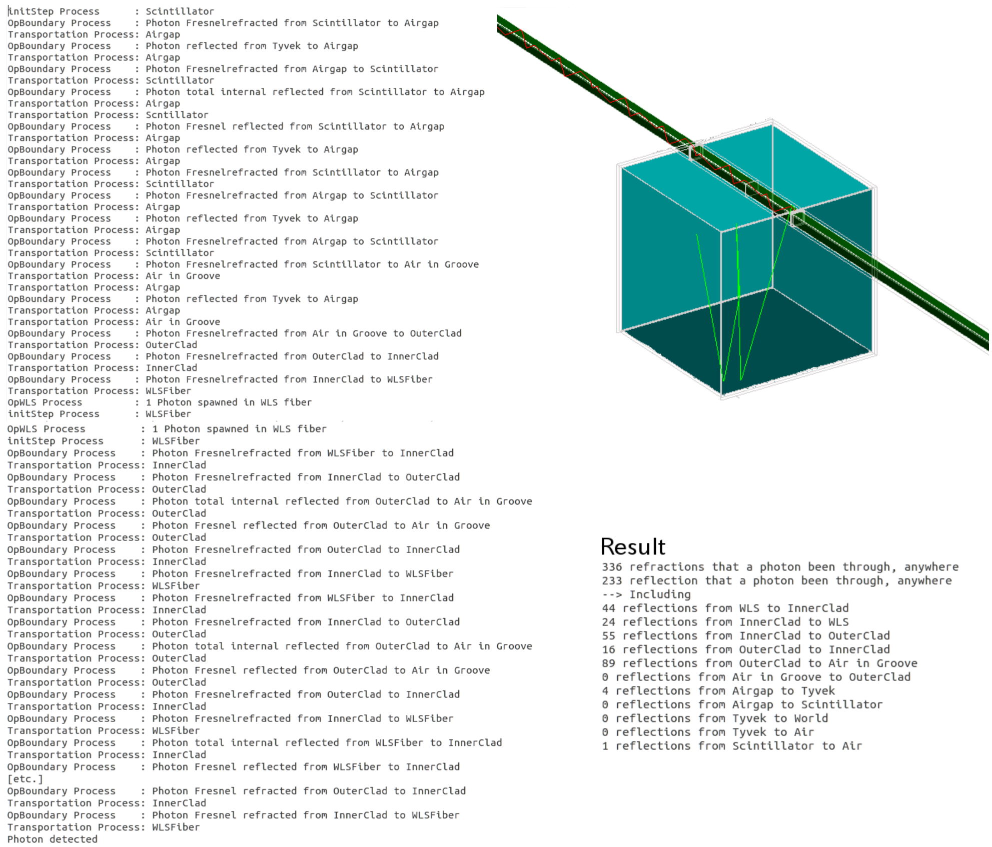

Figure 5.5: Example of an event with mentioning of the optical processes. The photon, after a few bounces in the scintillator-cube, enters the WLSFiber and gets detected.

This is very few compared to the number of scintillation photons that is of the order of 10 000 per MeV for a minimal ionising particle. So the Cerenkov process can be neglected in this case.

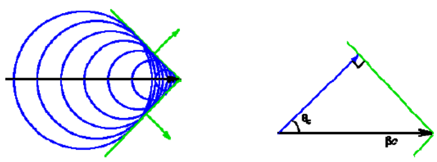

Figure 5.6: A particle, travelling along the black arrow, moves at velocity β_c through a medium. Photons are emitted at sped c/n and angle θ_c. They produce a cone shaped front, shown in green. Image: Dr. Booth, Coherent Effect for Charged Particles.

In regard to the SoLi∂ detector, The prior process for photon creation is the *scintillation* process (see section 3.1.1 on page 32). In GEANT4, the scintillation is primarily characterised by the scintillation yield. This is the mean number of photons generated by -and proportional to the energy deposit of a traversing particle. This number follows a Poisson distribution. With the resolution scale parameter, this distribution can be broadened or narrowed. This parameter is basically interesting for inorganic scintillators. Other important parameters are the fast- and slow exponential decay time constants that describe the decay time of the scintillating material. Finally, an emission spectrum must be provided. The properties of the different scintillators that are used in the optical simulation are given in table 5.1.

Table 5.1: Properties of the scintillating components of the optical simulation.

Scintillator	scintillation yield	resolution scale	time constants	spectrum
PVT	10/keV	1	10 ns	figure 3.7
^{6}LiF:ZnS(Ag	75/keV	1	1 ms	figure 3.8
WLS	$\gamma/\gamma_{absorbed}$	1	12 ns	figure 3.14

The processes that **influence** optical photons are bulk absorption, Rayleigh scattering, boundary processes and wavelength shifting (WLS).

Bulk *absorption* is a trivial process in that it merely kills the photon. For every medium, an absorption length can be specified in function of the particles momentum (see table 5.2). The absorption length is the average distance travelled by a photon before being absorbed by the medium. Note that the absorption length of the ^{6}LiF:ZnS(Ag) sheet is of the order of its own width, which is $0,25$mm. A photon that is generated at the outer face of the sheet can get absorbed in the sheet before even reaching the scintillator cube, let alone the fiber or the MPPC.

Table 5.2: Absorption length of the materials that are used in the optical simulation.

Material	Absorptionlength
PVT	5 m
^{6}LiF:ZnS(Ag)	0.2 mm
WLS	Wavelength dependent, see figure 3.14
OuterClad	20 m
InnerClad	20 m

Rayleigh scattering is the elastic scattering of radiation by particles much smaller than the wavelength of the radiation. Rayleigh scattering just changes the direction of a photon in a well-known way. The cross section is proportional to $\cos^2\theta$, where θ is the angle between the initial and final photon polarization. The scattered photon direction is perpendicular to the new photons polarization in such a way that the final direction, an the initial -and final polarization are all in one plane.

The *WLS* properties of a material are characterized by its photon absorption and photon emission spectrum and by a possible time delay between the absorption and re-emission of the photon. Wavelength Shifting may be simulated by specifying these empirical parameters. In this implementation of the WLS process, only one new photon per absorbed photon can be emitted (see table 5.1).

At surface *boundaries*, the optical photons can undergo one of three processes, namely transmission, absorption and reflection/refraction. The choice between the latter is determined by the quantum mechanical effect whether the photon has to be treated as particle rather than wave. The sum of the three probabilities has to add up to 1. For dielectric-dielectric boundaries (see next section 5.4) only transmission or relfection/refraction can occur. For dielectric-metal boundaries absorption or reflection can occur and for dielectric-black metal boundaries the photon will always be absorbed.

5.4 SURFACE BOUNDARIES

The boundary process that will ultimately affect a particle is, next to the properties of the particle, determined by the properties of the materials that compose the boundary. The boundary is specified by its model, its interface type and its surface finish.[53]

We distinguish three kinds of boundary **models**, namely the GLISUR model the UNIFIED model and the Look-Up-Table model (LUT):

1. The GLISUR model is the most basic model. The surface roughness is parametrised completely by the polish,

$$0 \leq p \leq 1. \tag{5.3}$$

The assumption is that a rough surface is a collection of micro facets. When a photon reflects on the surface, a local surface normal (facet normal) is randomly chosen. In the glisur model, the facet normal for η_{loc}, is computed as

$$\eta_{loc} = \eta_{glob} + (1-p)\eta_{smear}, \tag{5.4}$$

with $\eta_{smear} = (\eta', \eta'', \eta''')$ where the $\eta \in [0,1]$ are uniformly distributed random numbers.

2. The UNIFIED model was developed to reach results that are better compatible with measurements than the GLISUR model [53]. The assumption is that the angle α between the facet normal and the average surface is normally distributed with a standard deviation σ_α. The micro facets are regarded to be smooth at scales comparable to the considered photon wavelength (see figure 5.7, right).

In addition, an incoming photon under the angle θ_i to the average surface can be subject to different boundary processes (see figure 5.7,

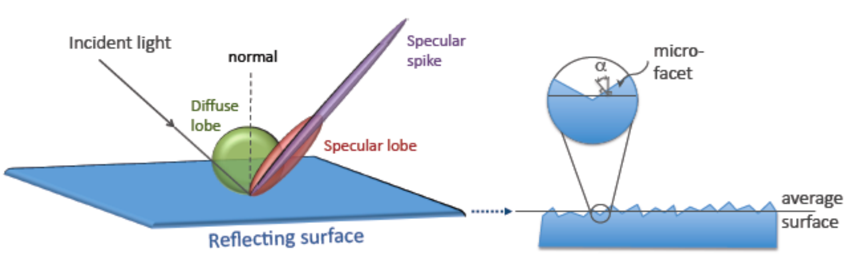

Figure 5.7: Recapitulation of figure 3.12. Left: Light reflection types, used in the calculation of the BRDF function and in GEANT4. Right: A ground surface is composed of micro-facets where alpha is the angle between a micro-facet normal and the average surface normal. Image: opengatecollaboration.

left): It can be reflected **specularly** with the same angle, it can be reflected at the micro facets resulting in a **spread** of the distribution dependent on σ_α, it can be subject to internal Lambertian reflection with a **diffuse** lobe as result, it can be reflected backwards in the same direction where it came from (because of several reflections within a deep groove), i.e. **backscattered** or it can be **transmitted** under the refraction angle θ_r. The probabilities for the different processes are respectively $C_{ss}, C_{sl}, C_{dl}, C_{bs}$ (which all contribute to the reflection coefficient R) and T (the transmission coefficient with T= 1-R).
The value of σ_α and the other coefficients have to be determined experimentally.

3. The LUT model is used to incorporate data from dedicated experiments as modified look-up-tables into GEANT4. The modified codes allow the user to specify the surface treatment and angular distributions directly from the experiment. A list of surfaces, with in some cases attached reflectors via different bondingtypes, are already available. The experiment to make such a LUT table for tyvek is illustrated in section 3.1.2 on page 38.

The boundary is further specified by one of three *interface types*:

1. The dielectric - dielectric type: The reflection (R) -and transmission (T = 1-R) probability is determined with help of the classical description of electromagnetic waves and the photon properties, i.e. the photons wave length, the angle of incidence, (linear) polarization and refractive index on both sides of the boundary. This results in the well-known Fresnel equations including, Fresnelrefraction, Fresnelreflection and total internal reflection. For the simple case of a perfectly smooth interface, all the user needs to provide are the refractive indices of the two materials
2. the dielectric - metal type: In this case it is not possible for the photon to be transmitted. It can be reflected with respect to the local normal of the medium boundary or absorbed according to the specified absorption probability of the material. Any material, independent of its composition, can be specified to have a metal-like surface, it only affects the reflection properties and not the material properties.
3. The dielectric- LUT type: The boundary is determined at one side by the dielectric type and on the other side by a Look-Up-Table, where reflection, transmission -and absorption for all angular distributions are defined.

Finally, a *surface finish* pinpoints the boundary down. When the GLISUR model or a dielectric-metal interface is chosen, the only surface finish options available are polished or ground. For the UNIFIED and LUT model, there is a wide range to choose from, in the form of combinations of the following: • polished or ground or etched,
and (optionally)
◦ front -or backpainted,
or
◦ a reflector of tyvek or dvm2000lumirror or TiO or teflon,
◦ where the reflector is air -or gluecoupled.

The program defaults to the GLISUR model and polished surface finish when no specific model and surface finish is specified by the user. For dielectric-metal surfaces, the default is also set to unit reflectivity and zero detection efficiency. In cases where the user specifies the UNIFIED model, but does not otherwise specify the model reflection probability constants, the default becomes diffuse lobe reflection. For some surface finishes, he LUT model is required.

The following table 5.3 lists the optical components that are used in the simulation, with their optical properties and surface definitions.

Table 5.3: Optical boundary properties of the materials that are used in the optical simulation.

Volume	Material	refractive index	Model	interface type	surface finish	SM1 polish
Scintillator	PVT	1,60	glisur	diel.-diel.	polished	0,98
Sheet	^{6}LiF:ZnS	1,43				
Airgap	Air	1	glisur	diel.-diel.	polished	
Groove	Air	1	glisur	diel.-diel.	polished	
Tyvek			LUT	diel.-LUT		
OuterClad	Fluorinated Polyethylene	1,42	glisur	diel.-diel.	polished	0,8
InnerClad	Polyethylene	1,49	glisur	diel.-diel.	polished	0,8
WLSCore	PMMA	1,59	glisur	diel.-diel.	polished	0,35
Mirror	Aluminium	1,097	glisur	diel.-metal	polished	1

Most surfaces are specified with the GLISUR model. Although it is more rudimentary than the UNIFIED model, it speeds the simulation up while rendering sufficient information on the boundary processes. The specific kind of reflection (spike-, lobe-,...) is subordinate to the overall refraction, reflection and absorption rates, that are respectively calculated with use of the Fresnel equations, the absorptionlengths (see table 5.2) and refractive indices (see table 5.3). In addition, the GLISUR model provides a simple range of surface roughnesses through the polish, $p \in [0, 1]$, which allows to investigate the influence of the polishing of the different materials on the outcome of the detector.

The reflection of the tyvek is simulated in more detail with the LUT-model, since it is of major importance in the light collection in the detector. A photon encounters the tyvek hundreds of times, while it bounces around the cube. The specific type of reflection determines the direction of the outgoing photon, which in turn will alter the probability for entering the fiber. The weight of the reflection types is given by the coefficients in table 3.1, that were determined as explained in section 3.1.2.

The optical simulation incorporates many parameters that have an impact on the light yield. A list of the relevant parameters is given in table 5.4.

Table 5.4: List of the parameters that are used in the optical simulation, with their ranges.

component	parameter	range
cube	material	set to PVT
	size	$0 < x <$world
	surfaceroughness	$0 \leq x \leq 1$
	number of cubes	$0 < x$
groove	number of grooves	$0 \leq x \leq 6$
	grooveroughness	$0 \leq x \leq 1$
tyvek	transparency	$0 \leq x \leq 1$
	reflectivity	$0 \leq x \leq 1$
	absorption	$0 \leq x \leq 1$
airgap	thickness	$0 < x$
fiber	number of fibers	$0 \leq x \leq$ number of grooves
	x size	$0 < x <$cube
	y size	$0 < x <$cube
	z size	$0 < x <$world
	number of clads	$0 \leq x \leq 1$
	roughness core	$0 \leq x \leq 1$
	roughness innerclad	$0 \leq x \leq 1$
	roughness outerclad	$0 \leq x \leq 1$
	thickness clad1	$0 < x$
	thickness clad2	$0 < x$
mirror	reflectivity	$0 \leq x \leq 1$
	distance	$0 \leq x <$ world
detector	distance	$0 \leq x <$ world

The relative influences of the parameters on the light yield will be investigated. To this end, a matrix of $3 \times 3 \times 3$ cubes is generated. For every event, a monoenergetic photon of $2,9$ eV is isotropically generated in the central scintillator cube. This configuration allows to investigate whether photons stay confined within their cube of generation, and if not, to investigate how they leaked to neighbouring cubes.
By default, the parameters are set to the following: the cubes edges are 5cm, fibers of $0,3$cm $\times$ $0,3$cm $\times$ 1m run through the cubes, at the ends of the fibers are two MPPC detectors, each cube is wrapped in one tyvek layer, between the cube and the tyvek is an airgap of $0,2$cm (see figure 5.8).

The number of detected photons, $\#_{detected}$, can be regarded as a product of many probabilities P_n with respect to the generated photons $\#_{generated}$

$$\#_{detected} = P_{tyvek} \times P_{not\ absorbed} \times P_{entered\ fiber} \times P_{not\ lost\ in\ fiber} \times \#_{generated}, \quad (5.5)$$

with P_{tyvek} the probability that the photon was always reflected by the tyvek and not transmitted, and with $P_{not\ absorbed}$ and $P_{entered\ fiber}$ self explaining.

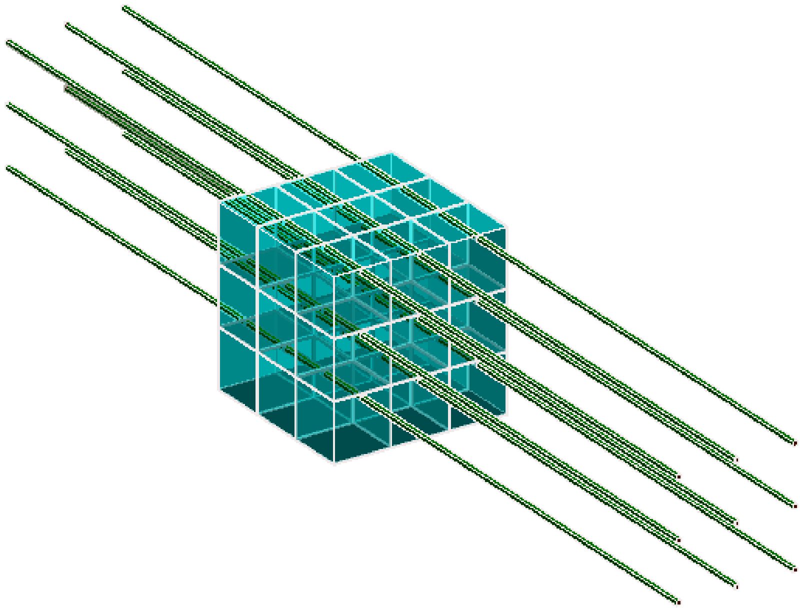

Figure 5.8: Setup of the simulation for the study of the parameters (the tyvek is transparent for convenience of viewing the tracks).

By varying one parameter at a time - ceteris paribus - the influence of this parameter on the light yield can be studied. Even if some other parameter isn't set properly, since all measurements will be influenced the same by the aberrant parameter. For example, when the probability to escape the fiber is too big, the impact of the tyvek reflectivity on the light yield is still apparent since measurements suffer the same loss.

The stepping action keeps track of what happens to the photon, i.e. on one hand where the photon terminates its track and on the other hand what happens if the photons enter the fiber. Both categories are divided in several contributions (explained below), which are shown in histograms in the upcoming sections.

The processes that terminate the photon track are denoted as *endstages*. The photons that are detected by an MPPC are depicted by **Detected Photons**. Some photons are **absorbed**, be it in the Scintillatorcube, the reflector, the airgap, or the groove where the fiber is placed in. Photons that went through the tyvek and got into another cube than the central cube are **Leaked through Tyvek** (the photon is then stopped and killed). Finally, the photon could get **lost in the fiber** (this does not include the photons that get detected or absorbed in the fibergroove).

In addition, the different scenarios that can happen to a photon after it entered the fiber, are compared relative to each other. This includes all the processes that render the photon 'lost in the fiber':**WLSProcess Died** means that the photon did not have enough energy to generate a new photon in the WLS fiber, thus terminating the photon chain in the fiber. **Escape Mid-Fiber** designates the photons that escaped from the fiber to the world. The photons that escape the fiber and get into another cube than the central cube are called **Leaked through Fiber**. **Absorbtion in Fiber** can occur as well. Next to processes that loose the photons in the fiber, the photon can also escape the fiber back to the central cube, where it continues its run. **Leaked from Fiber back to Cube** keeps track of these events. The track is allowed to continue, since the photon still has a solid change to be detected. Finally, the **detected** photons are also shown in relation with all photons that entered the fiber, as is the case for the photons that were **absorbed in the groove**.

The obtained results are shown in the histograms of the following sections. On the x-axis the variation of the parameter is set. The different contributions, that were listed earlier in bold face, are set out in separate histograms, as fractions of the total number. And the lot of them is also shown as a stacked histogram, where the different contributions are stacked on top of another. The total bar then equals 100%.
Errors are indicated on the bars under the form of

$$Error = \sqrt{N} \tag{5.6}$$

with N the number of entries in the bin.
Whenever possible in a significant way, a fit is performed on a histogram. The fits are of the forms that can be found in table 5.5.

Table 5.5: Function that are used to fit the histograms in the upcoming sections.

Fit	Function	Parameters
Polynomial	$y = p_n x^n + \cdots + p_2 x^2 + p_1 x + p_0$	p_n
exponential	$y = cst + A.exp(slope.x)$	cst, A, slope
exponentia decay	$y = cst + A.exp(-slope.x)$	cst, A, slope
logarithmic	$y = cst + A.log(slope.x)$	cst, A, slope

The parameters that were fitted to a specific histogram, can be found in the statistics box at the top of the histogram. As is the case for the χ^2 value, which is calculated as

$$\chi^2 = \sum_i^{bins} \frac{(E_i - O_i)^2}{O_i}, \tag{5.7}$$

with O_i the observed frequency for bin i and E_i the expected frequency for bin i. The number of degrees of freedom is shown as ndf.

5.5.1 *Study of the cubesize*

The Cubesize varies from $2,5$cm to 10cm, with increments of $0,5$cm.
Note that the range of the y axis is adapted to the data. To get an idea of the overall importance of a contribution, turn to the stacked histogram at the bottom right. In the separate histograms, the shape of the distributions can be studied.

The number of detected photons decreases as the cube size gets bigger (see figure 5.9). The portion that the fiber occupies inside the cube decreases as the cubesize increases, thus less photons will enter the fiber. On the other hand the number of photons that is absorbed in the cube increases, as the pathlength inside the scintillator gets longer. The photons will reach the edges of the cube and therefore the reflector less, which explains the decrease in absorption in -and leakage through the tyvek.

The number of detected photons decreases with a factor $\sim 0,4$ when the size is quadrupled. For the test construction of the SoLi∂ detector, the cube size is chosen to be 5cm. Other considerations had to be taken into account as well, like the neutron capture efficiency, the cost and the resolution.

In figure 5.10 is shown what happens to the photons that enter the fiber. 85 to 90% of these photons leave the fiber again to the cube; the photon has to enter the fiber under the right angle to be able to continue its way down to the detector. The increase in photons that leak back to the cube is compensated by the less photons that escape the fiber to the world and to other scintillatorcubes. This makes sense, regarding the increase of the cube size.
However, once inside the fiber, the cube size has no influence on the fraction of photons that is detected, absorbed, 'WLSdies' or escapes. Fitting these distributions would not be significant.

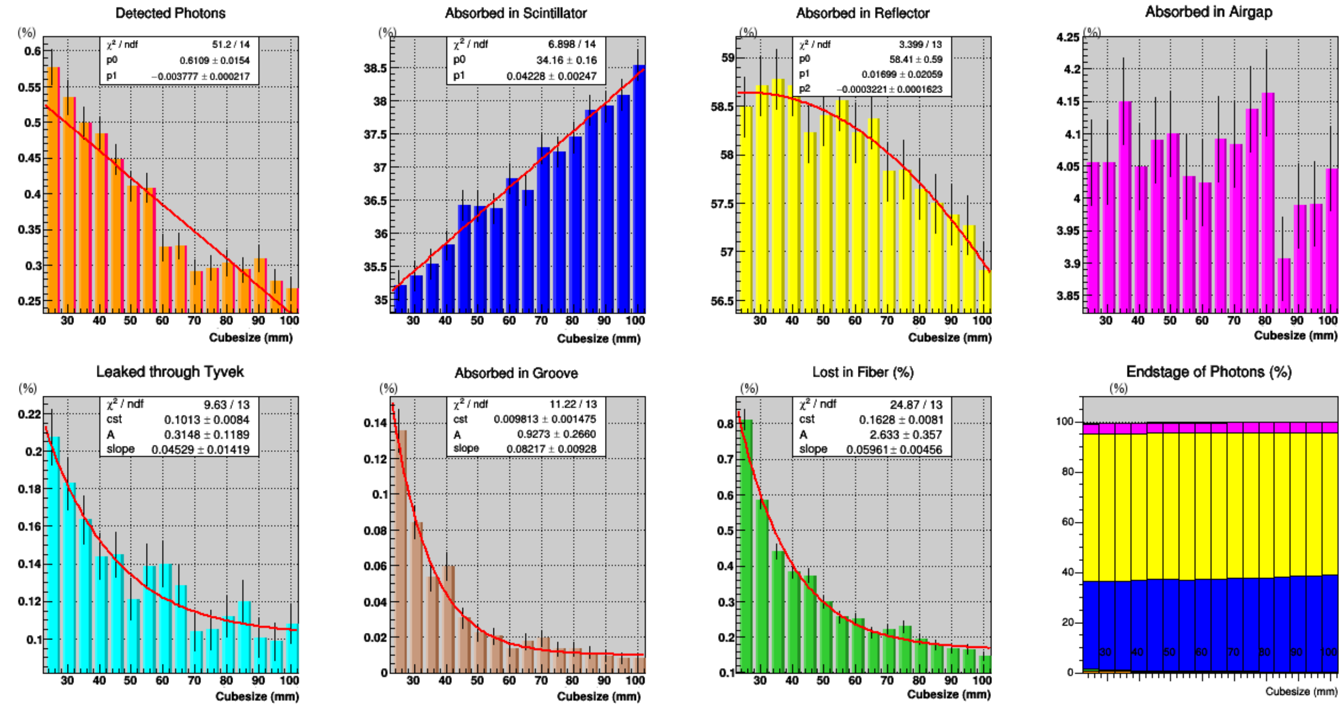

Figure 5.9: Endstages of the photons under variation of the cubesize.

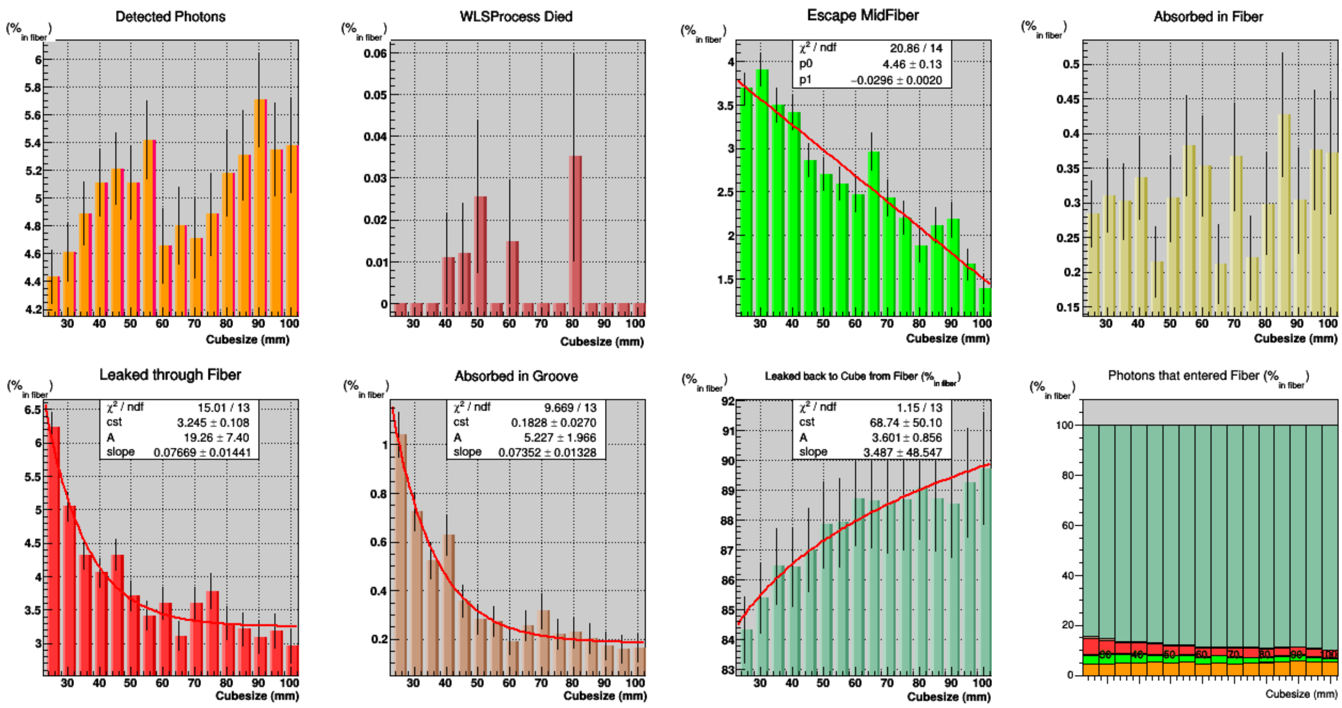

Figure 5.10: Destination of the photons that entered the fiber under variation of the cubesize.

.

5.5.2 *Study of the Reflectivity of the Mirror*

At one fiber end, the MPPC is replaced by a mirror. Instead of being detected by the MPPC, the photon can be reflected by the mirror and get detected by the other MPPC. The reflectivity of the mirror is varied from 100% reflective to not reflective at all. In the latter case, a photon could still be reflected at the fiberend by the small boundary of fiber and aircoupling, but photons will be absorbed by the mirror as well. The absorbed photons end up in the category 'Absorbed in Groove'. The results are shown in figure 5.11.

The mirror reflectivity has a linear relation to the number of detected photons. The 'Absorbed in Groove' has the inverse shape. The absorptions in the scintillator, airgap and tyvek and transmission through the tyvek are independent of what happens inside the fiber. Their variations Δ are small in comparison to their mean value, which is expressed by the relative variation

$$var_{rel} = \frac{\Delta}{mean}. \tag{5.8}$$

The relative variation is for the absorption in the scintillator 0.015%, in the airgap 0.014% and in the tyvek 0.038% and for transmission through the tyvek 0.044%.

Figure 5.12 tells us that the extra reflected photons are either detected, escape the fiber or are absorbed in the fiber. For a more reflective mirror, no extra photons will leak back to the cube or to adjacent cubes. This is probably due to the fact that the photons that reach the mirror, travelled at angles for which the photon is easily reflected by the fiber such that the photon stays confined in the fiber. The reflected photon moves on under the same angles which keeps it trapped in the fiber.

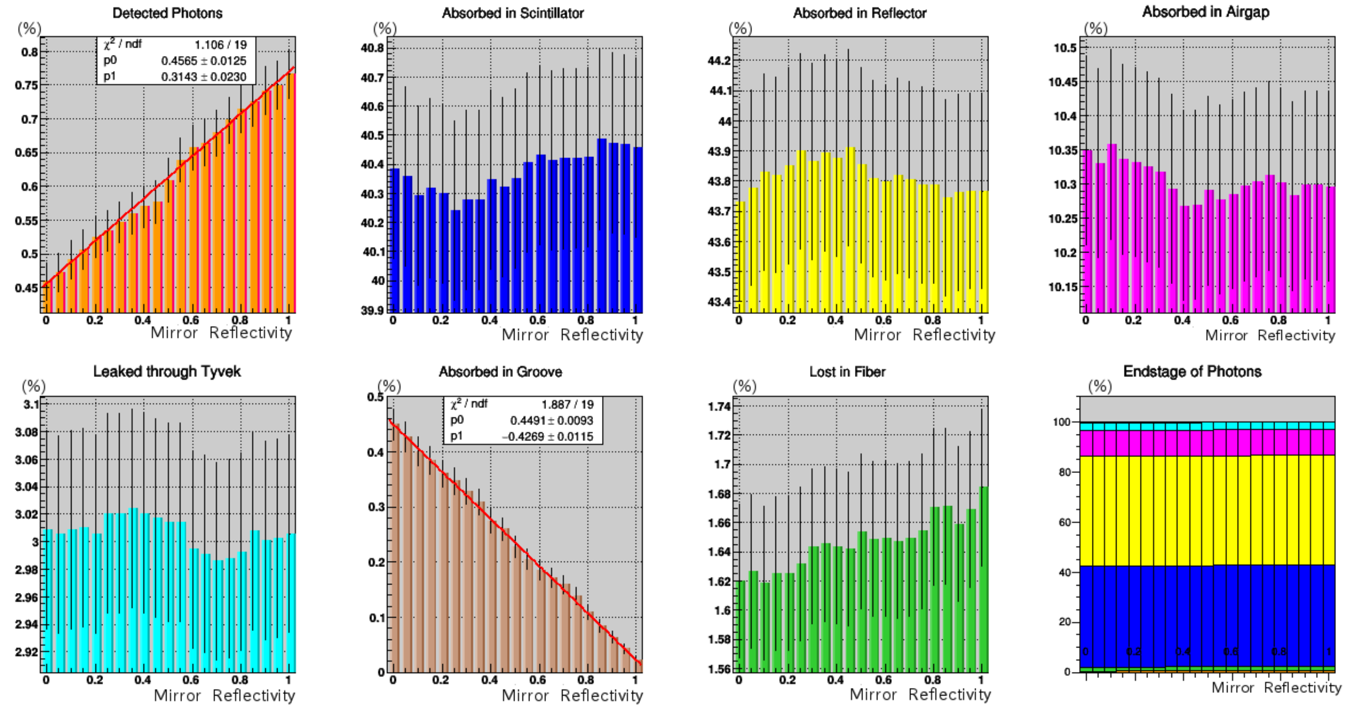

Figure 5.11: Endstages of the photons under variation of the reflectivity of the mirror.

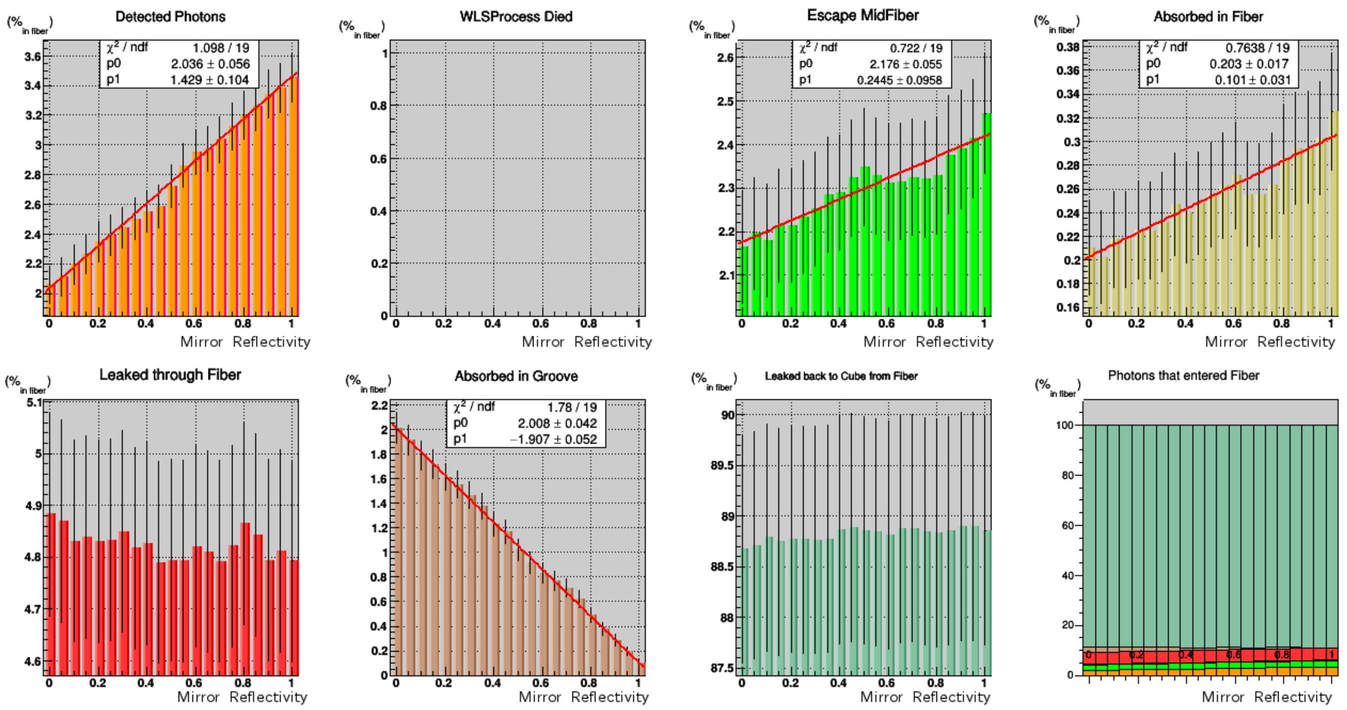

Figure 5.12: Destination of the photons that entered the fiber under variation of the reflectivity of the mirror.

.

5.5.3 *Study of the Fiber position*

The position of the fiber is varied from one corner to the diagonally opposing corner, in 20 steps. The fiber describes a diagonal movement through the bulk of the cube. The position is described relative to the extremal positions. At fraction 1, the fiber is at the starting corner, at 0 it is in the center of the cube and at -1 it is in the opposite corner.

Figure 5.13 show that the number of detected photons increases with $\sim 30\%$ when the fiber is at the center, in comparison to being at the corner. Overall, more photons enter the fiber. Therefore the contributions from losses in the fiber increase in the same manner.

In figure 5.25 we see that what happens to the photons that enter the fiber, also changes. Apparently, less photons will leak back to the center cube, when the fiber lies in the middle of the cube. This could be due to the fact that photons that can enter the fiber when it lies in the corner, arrive generally under a large angle to the fiberaxis, for which escaping is more probable. The decrease in photons that leak back, is compensated by the contributions from detection, escaping midfiber and leaking to other cubes, which all increase.

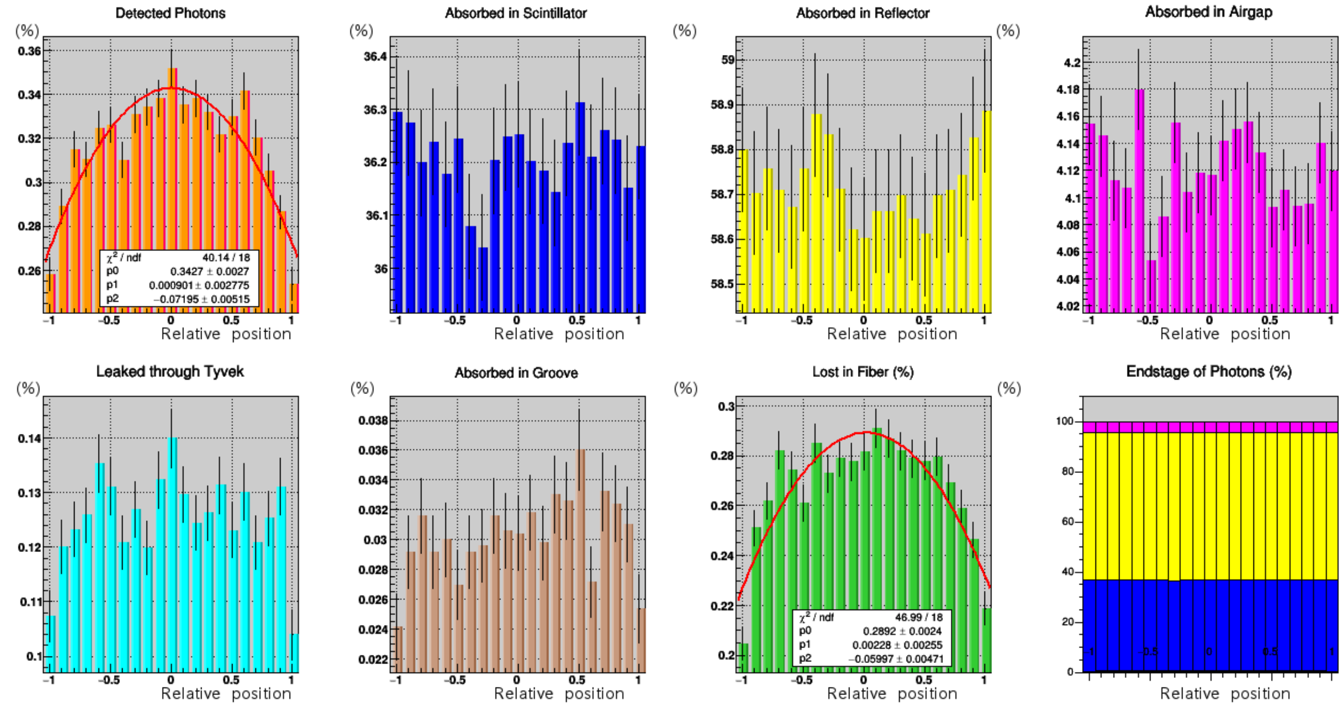

Figure 5.13: Endstages of the photons under variation of the position of the fiber.

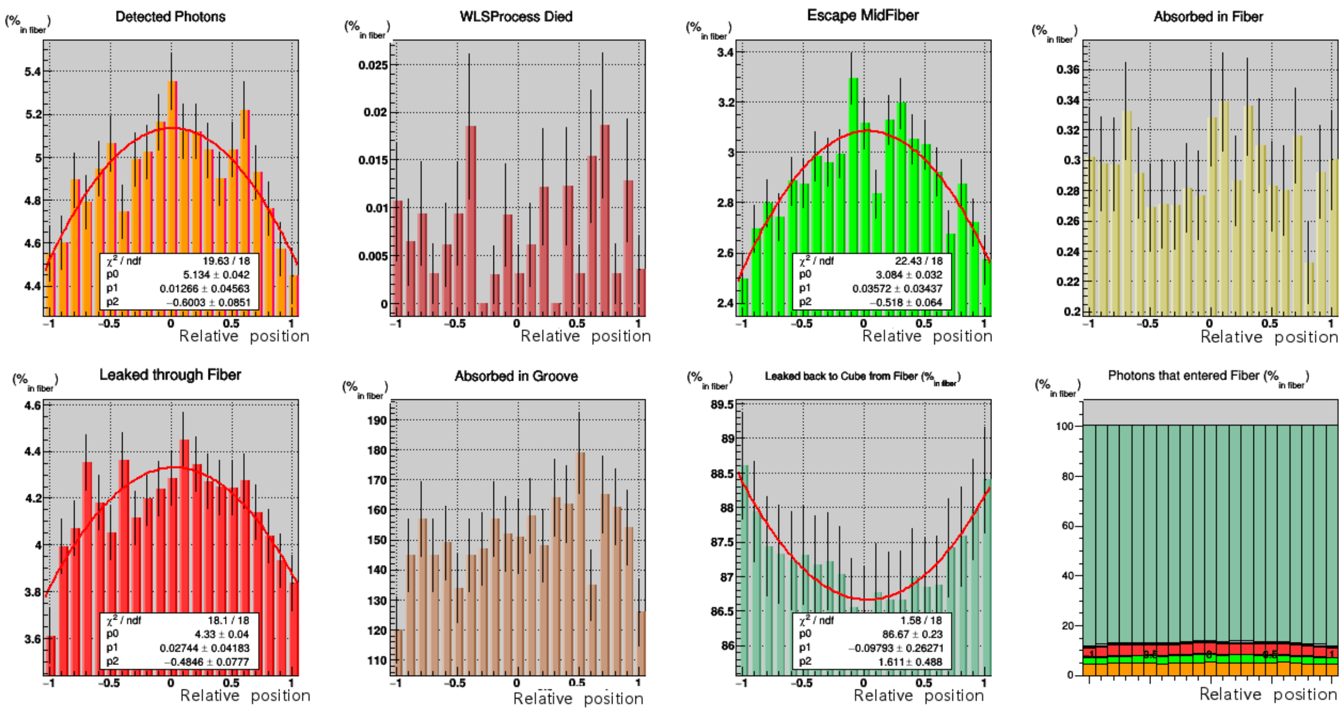

Figure 5.14: Destination of the photons that entered the fiber under variation of the position of the fiber.

5.5.4 *Study of the ScintillatorRoughness*

The roughness of the cube faces is varied within the glisur-model (see section 5.4), from 0 to 1, the latter corresponds to perfectly polished. The groove of the scintillator, where the fiber is placed in, is not affected.

As the faces are better polished, we notice a decrease in photon detection (see figure 5.16). Between a polishing of 0 and $0,95$, there is a decrease of $\sim 37\%$.

The case of perfect polishing, at a value of 1, is exceptional and unrealistic. The angle of the incident light ray on the face will be equal to the angle of the reflected ray. The trajectory of the photon can become a geometric pattern, as in figure 5.15. In these cases, the number of reflections at the cube faces increases drastically. For 0 polishing, the average photon reflects ~ 10 times at a face, while for a polishing of 1 this becomes ~ 50 times (average taken over 500 photons). In the latter case, the photon stays confined within the cube, which increases the probability for absorption in the scintillator.

Figure 5.15: When the faces of the scintillator are perfectly polished, the photon often describes geometric trajectories. Some patterns are shown, with a perpendicular view to the scintillator face.

From figure 5.17 we know that the scintillator roughness has no more influence on the proceedings of the photon, once it has entered the fiber. This implies that the overall decrease in photondetection in figure 5.16, is due to the decrease in photons that enter the fiber.
Instead, the photons are absorbed in the reflector and airgap more often when the faces are better polished, reinforced by absorption in the scintillator for polishing $> 0,85$.

Note, that the histogram for photons that leaked to an adjacent cube through the fiber is empty. This is because the simulation was now done for only 1 cube, instead of for a matrix of $3 \times 3 \times 3$ cubes. This happened for no particular reason. The photons that would have leaked through the fiber, now escaped the fiber to the world. These photons are now integrated in the 'escape midfiber' histogram. The photons that leaked through the tyvek, now escaped to the world instead of to an adjacent cube so this histogram is still filled.
Some of the following simulations have also be done for the configuration with only 1 cube.

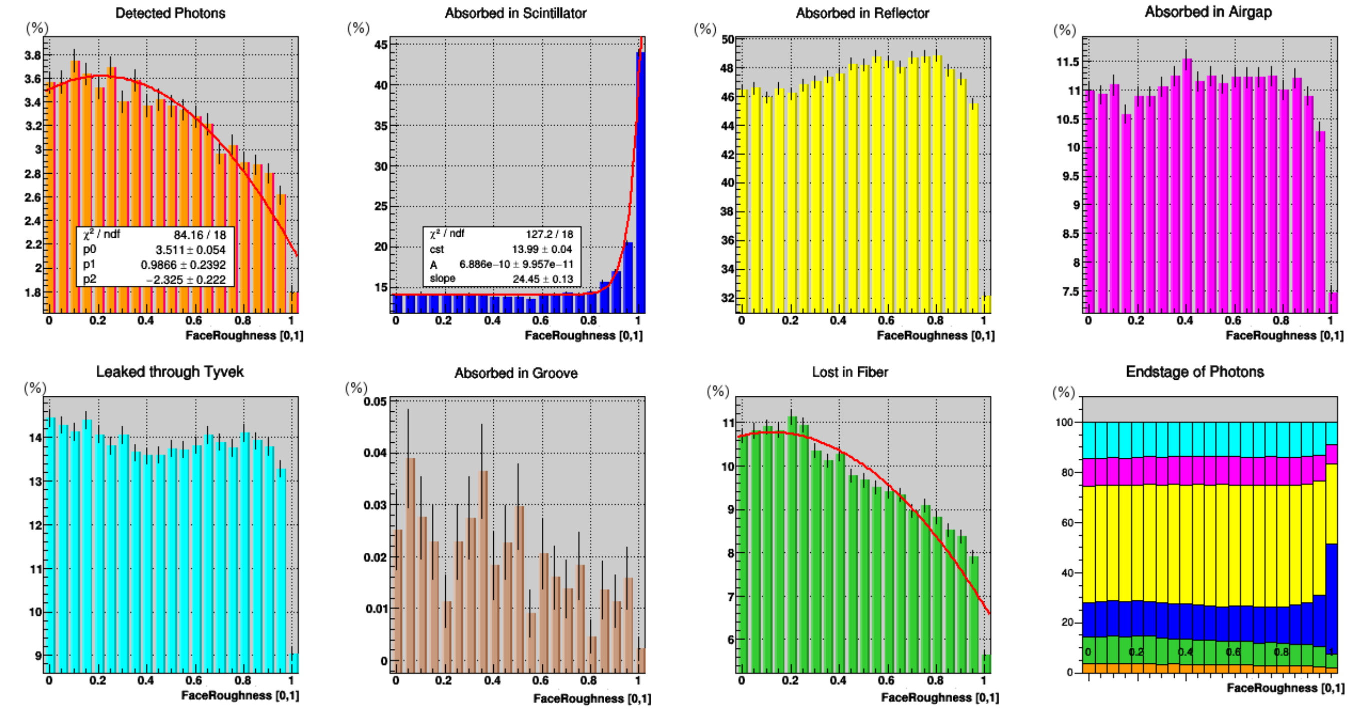

Figure 5.16: Endstages of the photons under variation of the roughness of the faces of the cube.

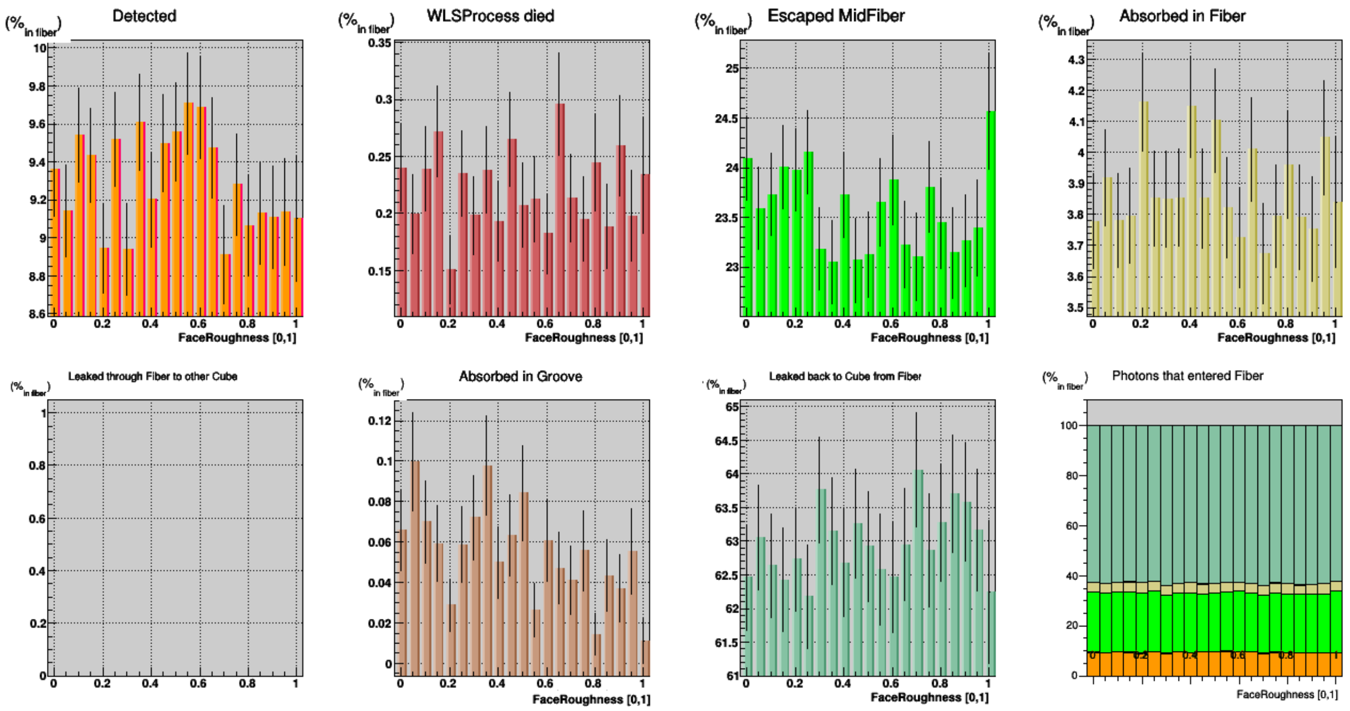

Figure 5.17: Destination of the photons that entered the fiber under variation of the roughness of the faces of the cube.

5.5.5 *Study of the Airgap Thickness*

Between the scintillator cube and the tyvek wrapping is an airgap. The thickness of this airgap is varied from $0,5$mm to 10mm, with increments of $0,5$mm.

Figure 5.18 shows that the detection efficiency does not change for different roughnesses. However, the place of absorption changes. From all photons, $2,25\%$ less photons are absorbed in the scintillator, while $0,65\%$ more photons are absorbed in the airgap, and 2% more are absorbed in the reflector. In addition $0,4\%$ more photons leak through the tyvek. The difference of 0,03% in absorption in the groove is negligible. It seems as if the photons are more often or longer in the airgap. From there they are more frequently terminated by the tyvek (leaking and absorption) or the airgap (absorption).

Within the fiber (see figure 5.19), 1,5% less photons escape the fiber to the world, while $\sim 1\%$ more photons escape the fiber back to the cube. The photons that escape the fiber to the airgap around the cube, are also included in this last category, so this phenomenon is easily understood.
In addition, $\sim 1,3\%$ more photons are detected, once the photon has entered the fiber. The fiber is placed at the top of the cube (see figure 5.8 on page 73). By increasing the width of the airgap, the reflective tyvek is further away from the fiber. But I do not see how this would increase the light yield.

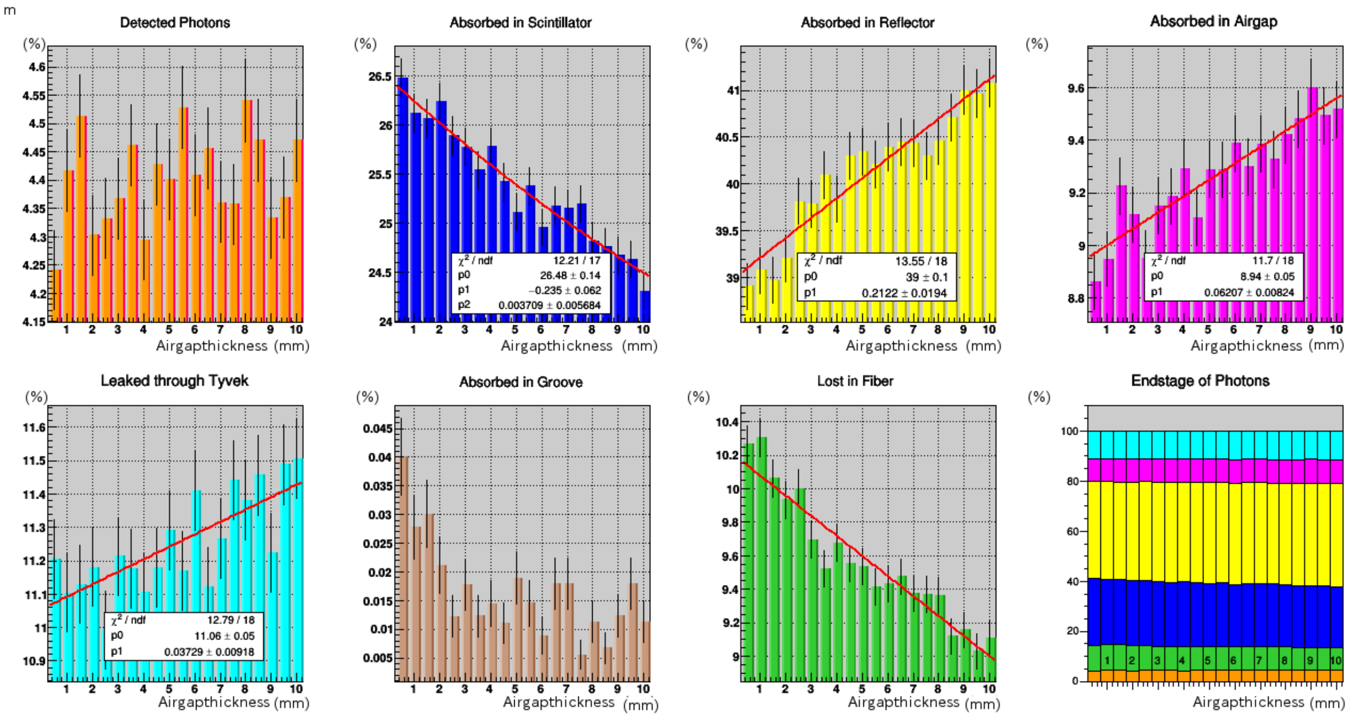

Figure 5.18: Endstages of the photons under variation of the width of the airgap.

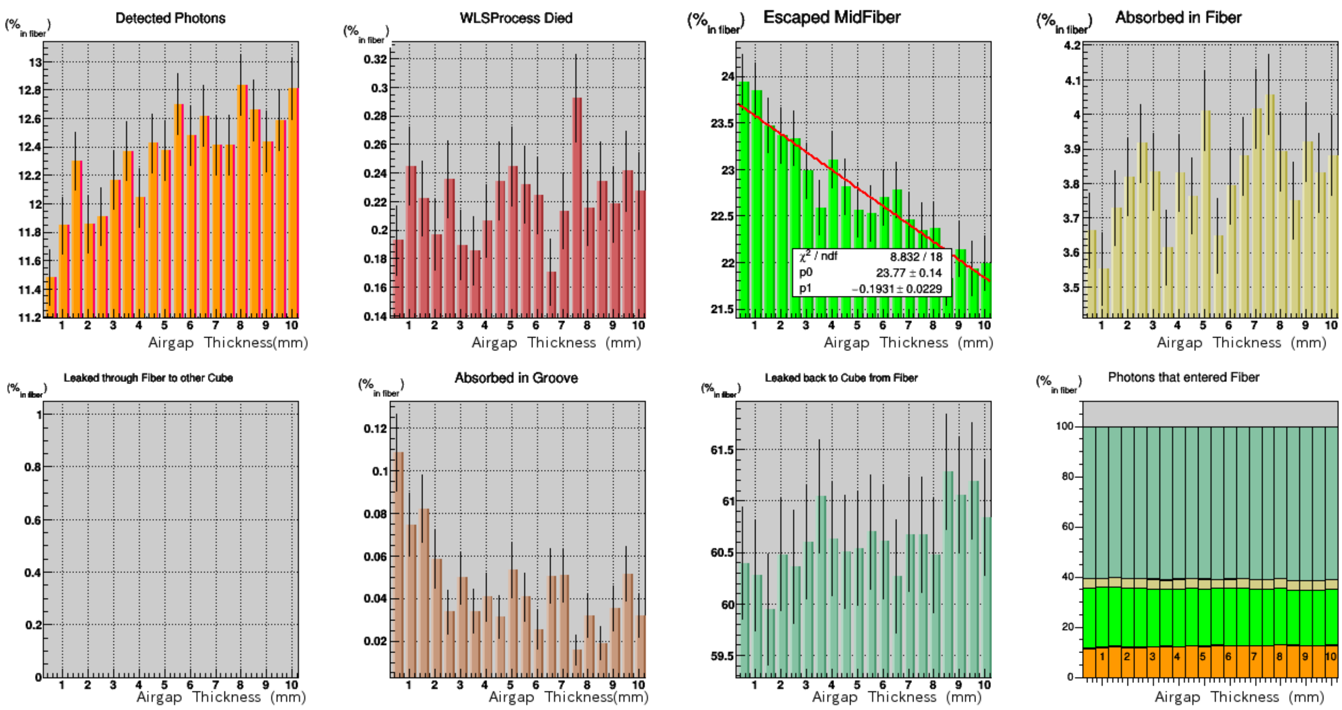

Figure 5.19: Destination of the photons that entered the fiber under variation of the width of the airgap.

5.5.6 *Study of the Tyvek transmission*

The scintillator is wrapped in tyvek to optimise the light collection. The light that is incident on the tyvek wrapping is either reflected, transmitted or absorbed. The sum of the three options is equal to 1. The ratio of absorption is chosen to be 0,05%. Figure 5.20 shows the impact of increasing the transmission rate from 0% to 95%.

As the transmission is increased, all other contributions to the endstage decrease exponentially. The number of detected photons decreases from $4,5\%$ to $0,6\%$, which is a decrease of 87%. This is a huge difference, but its taken between two extremal cases.

The photons that have entered the fiber, also take different paths when the transmission of the tyvek is changed, as can be seen in figure 5.21. The fiber is placed at the top face of the cube. This makes that right above the fiber, lies the tyvek wrapping. When the photon escapes the fiber, it can be reflected at the tyvek, which sends the photon back in the fiber or to the scintillator cube. When the transmission of the tyvek is increased, less photons will be send back to the cube and more will escape through the tyvek to the world. However, the latter is counted as 'escaped midfiber'.

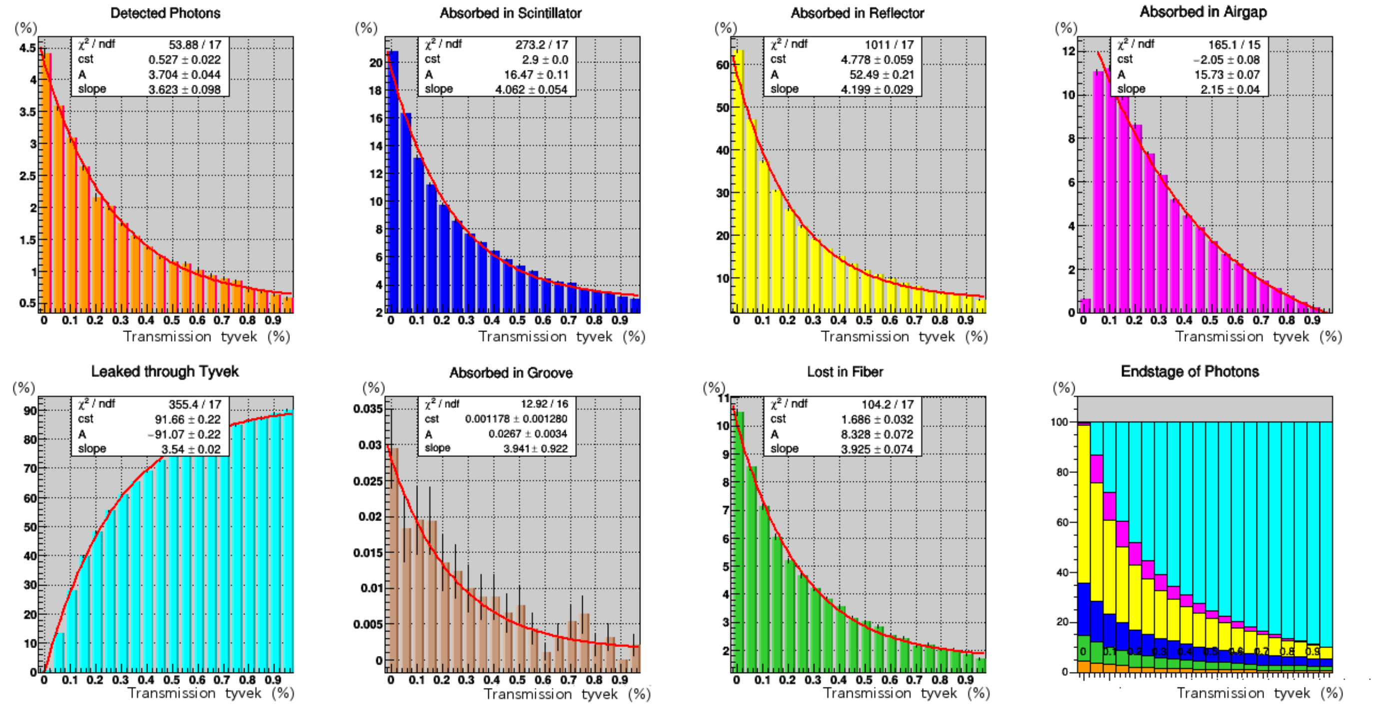

Figure 5.20: Endstages of the photons under variation of the transmission of the tyvek.

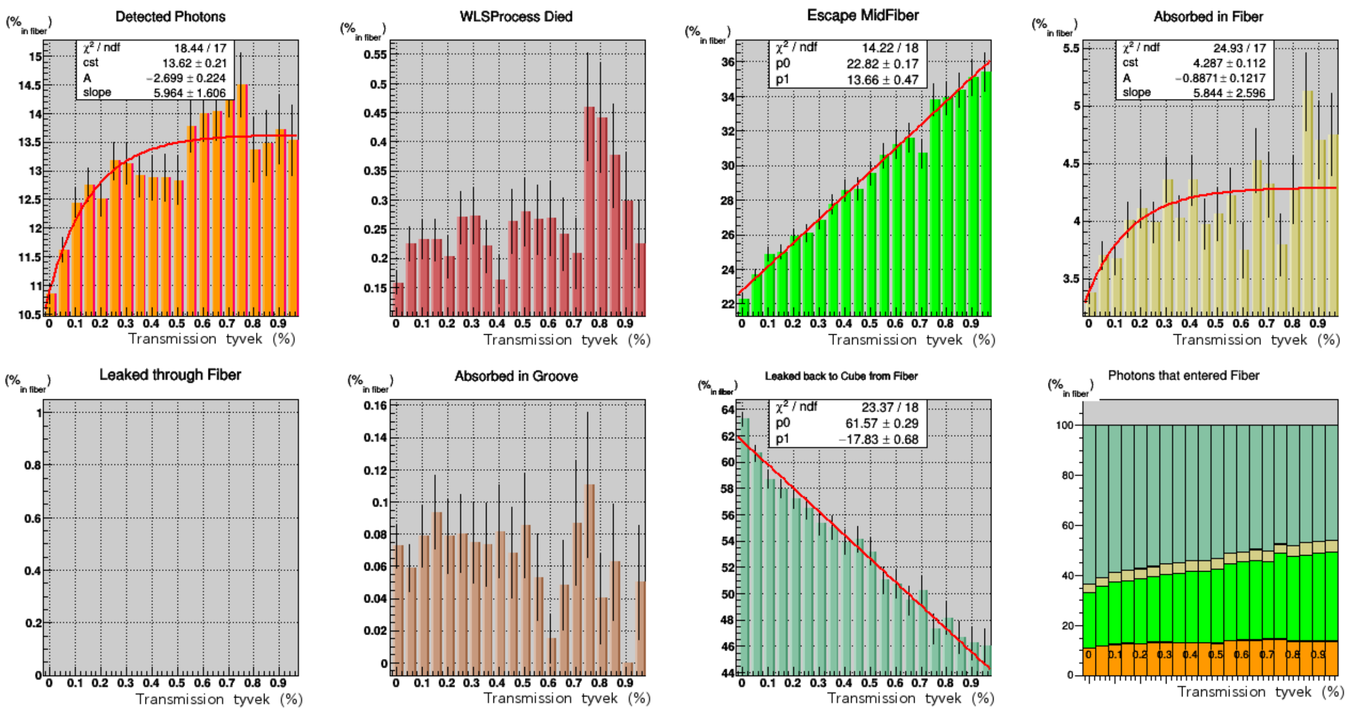

Figure 5.21: Destination of the photons that entered the fiber under variation of the transmission of the tyvek.

.

5.5.7 *Study of the Roughness of the WLS Core*

The fiber that transports the photons to the photodetector consists of three layers; a core and 2 claddings. The refractive index of the consequent materials decreases, to achieve optimal light confinement. In this and the following sections, the influence of the roughness of each layer is investigated. We start with the roughness of the core.

Figure 5.22 indicates that the light yield increases linearly as the core is better polished. An improvement of 45% is observed. The increase in photo detection is compensated completely by a decrease in loss in the fiber. That is, from all photons $1,4\%$ less are lost in the fiber whereas $1,4\%$ more are detected.

Turning to figure 5.23, we see that less photons are able to escape the fiber when the core is smoother. The core fullfills its purpose optimally when polished. As side effect to confining the photons better, more photons are absorbed in the fiber.

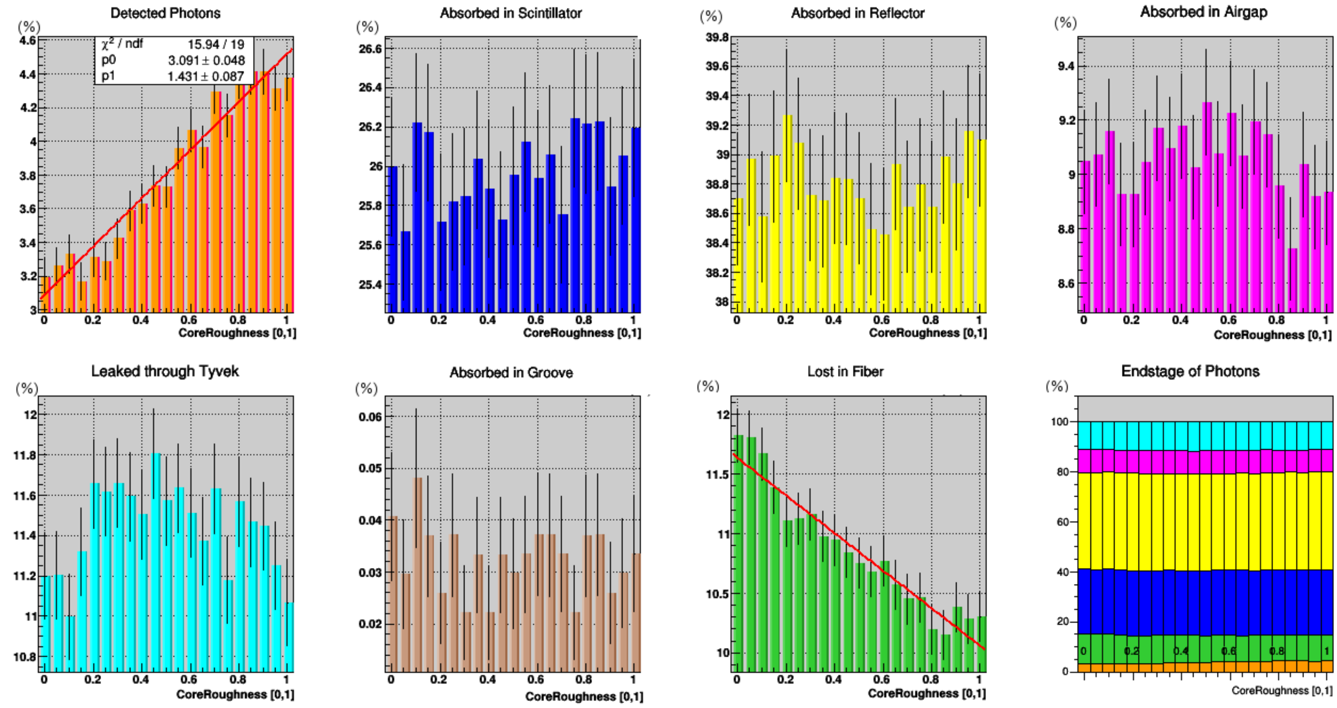

Figure 5.22: Endstages of the photons under variation of the roughness of the fiber core.

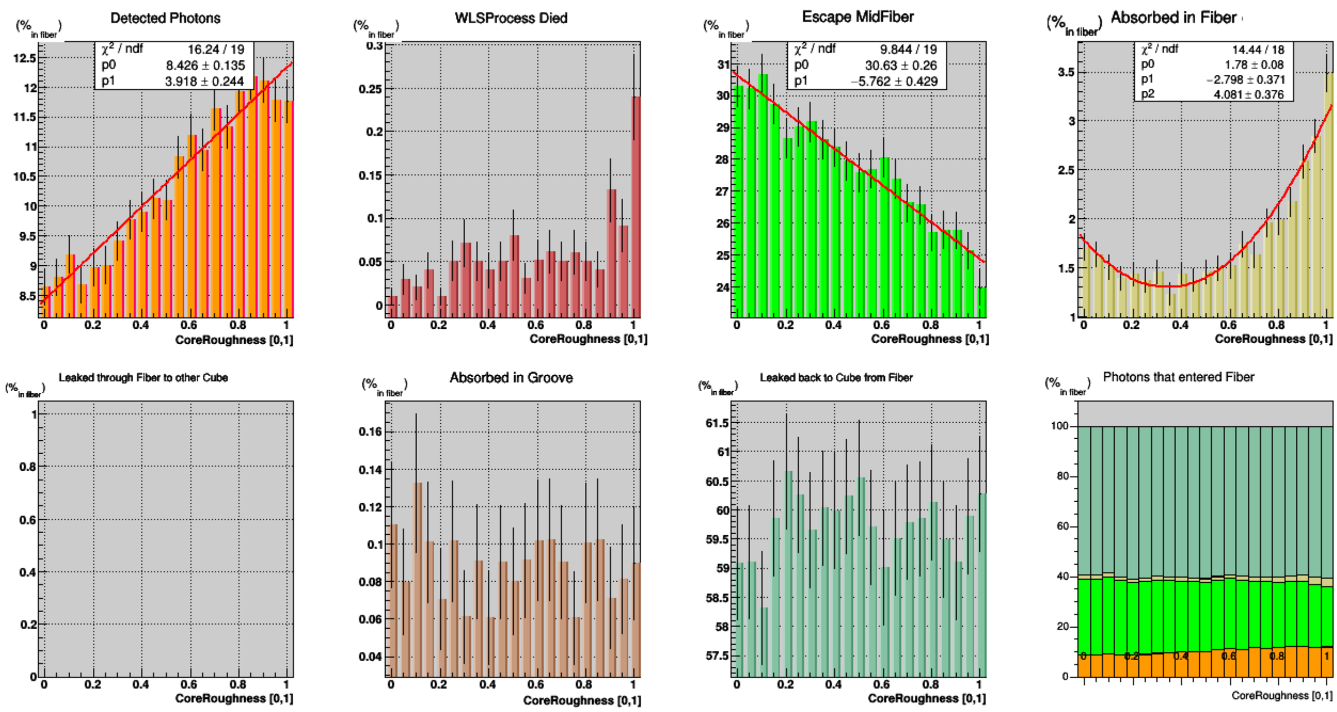

Figure 5.23: Destination of the photons that entered the fiber under variation of the roughness of the fiber core.

.

5.5.8 *Study of the Roughness of the Inner Clad*

The roughness of the boundary between the innerclad and the outerclad is investigated. The roughness is again specified in the GLISURmodel and ranges from 0 to 1(perfectly polished).
There is little to no effect from this roughness on the outcome of the experiment.

Using equation 5.8 we get the following for the relative variations of the different contributions:

- Detected: 3,5%
- Absorbed in scintillator: 1,9%
- Absorbed in tyvek: 12%
- Absorbed in airgap :3,3%
- Leaked through tyvek: 2,2%
- Absorbed in groove: 46% (on small values around 0,028)
- Lost in fiber: 1,5%

Destination of photons that entered the fiber

- Detected: 3,4%
- WLS process died: 38% (on small values around 0,2)
- Escaped Midfiber: 2,9%
- Absorbed in fiber: 9,0%
- Absorbed in Groove: 40% (on small values around 0,07)
- Leaked back to cube from fiber: 1,1%

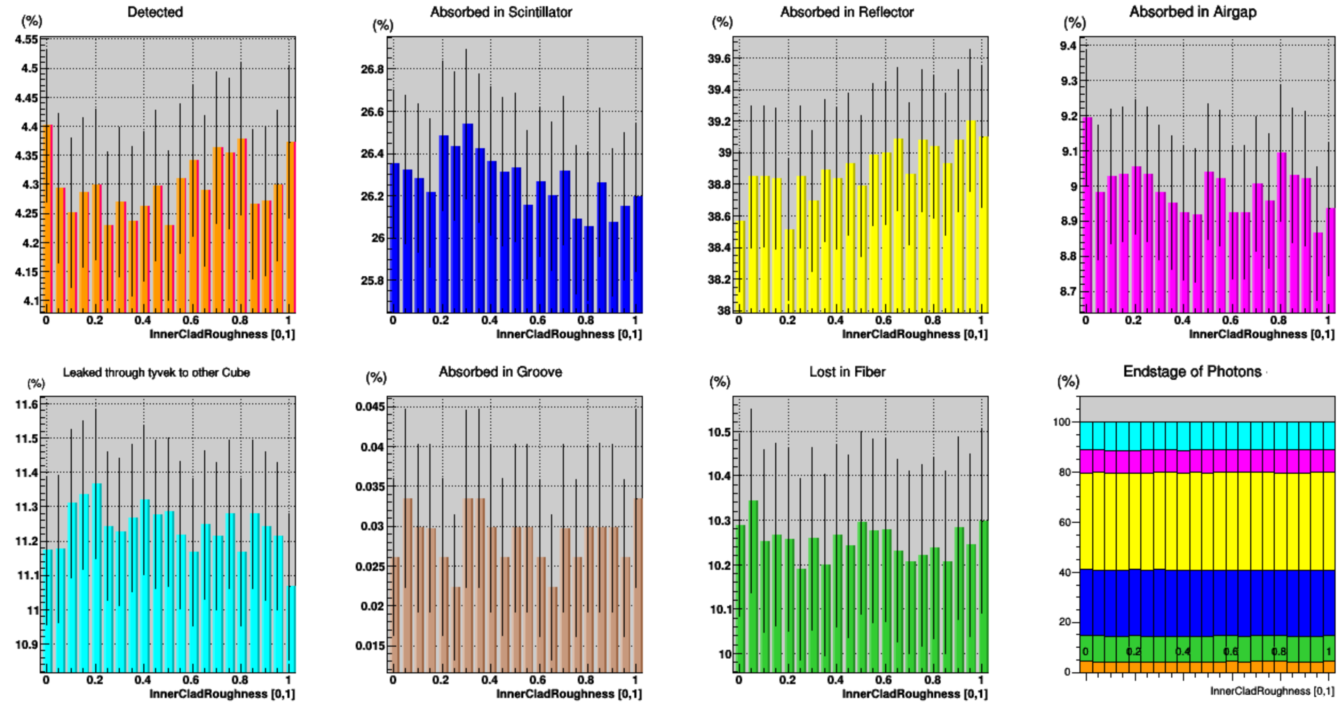

Figure 5.24: destination of the photons that entered the fiber under variation of the roughness of the inner cladding on the fiber.

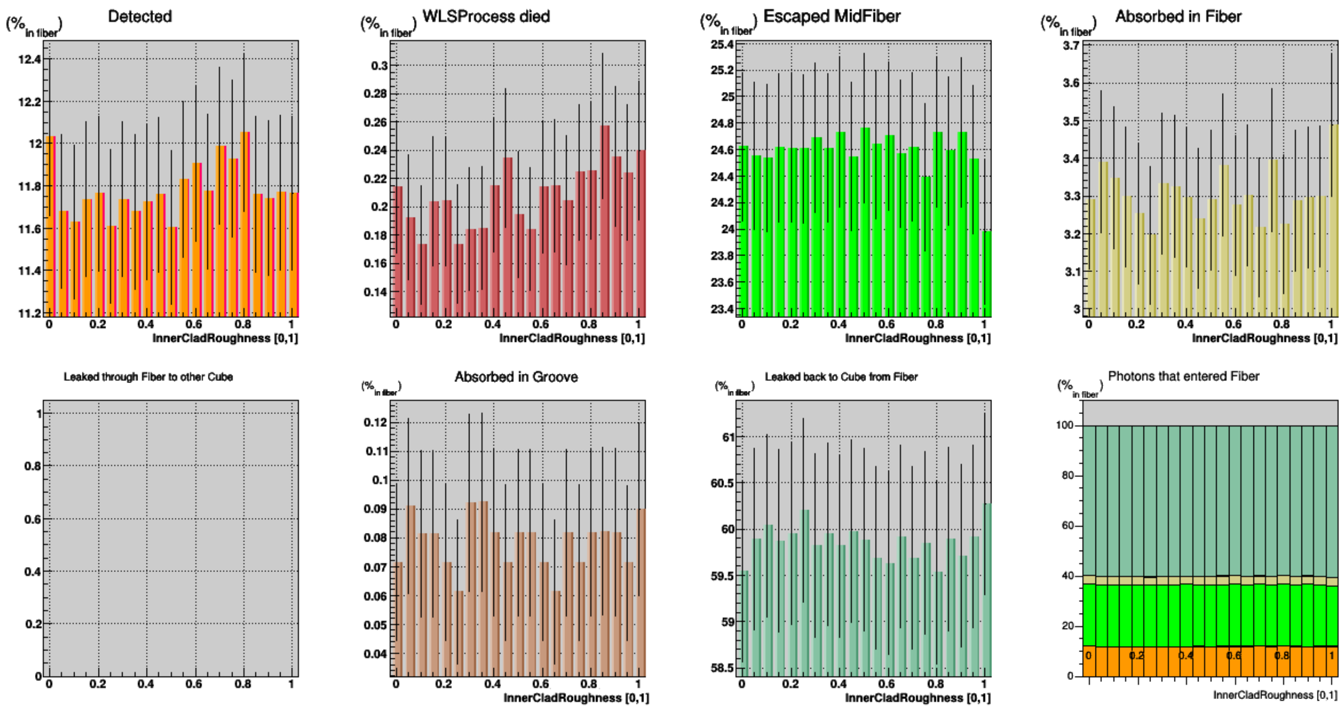

Figure 5.25: destination of the photons that entered the fiber under variation of the roughness of the inner clad on the fiber.

.

5.5.9 *Study of the Roughness of the Outer Clad*

For the study of the roughness of the outerclad we obtain the results that are shown in figure 5.26.

A large increase in lightyield is found for a smooth outer cladding. That is, an increase of 125%. However, this increase is primarily noteworthy above a polishing of $0,8$, which is probably in the range of the impossible in regard to the real experiment.

For polishings between 0 and $0,8$, there is no significant change in detection of the photons. However, in this range, there is a decrease in absorptions in the scintillator, airgap and tyvek. This is balanced by an increase in losses in the fiber. The foregoing indicates that more photons enter the fiber, when the outer cladding is better polished, but an equal amount of photons reaches eventually the detector.
Indeed, figure 5.27 shows that in the range from 0 to $0,8$ polishing, the number of photons that escape midfiber to the world increase while the number of photons that leak back to the cube decreases. This keeps the number of photons that reach the detector steady over this range.
As it seems, the photons stay trapped longer in the cube, such that by the time they escape, they escape to the world and not back to the cube.
Figure 5.27 shows that above $0,8$ polishing, the ratio of absorbed photons in the fiber increases drastically, as is the case for the WLS processes that ended. But this is again in the unphysical range.

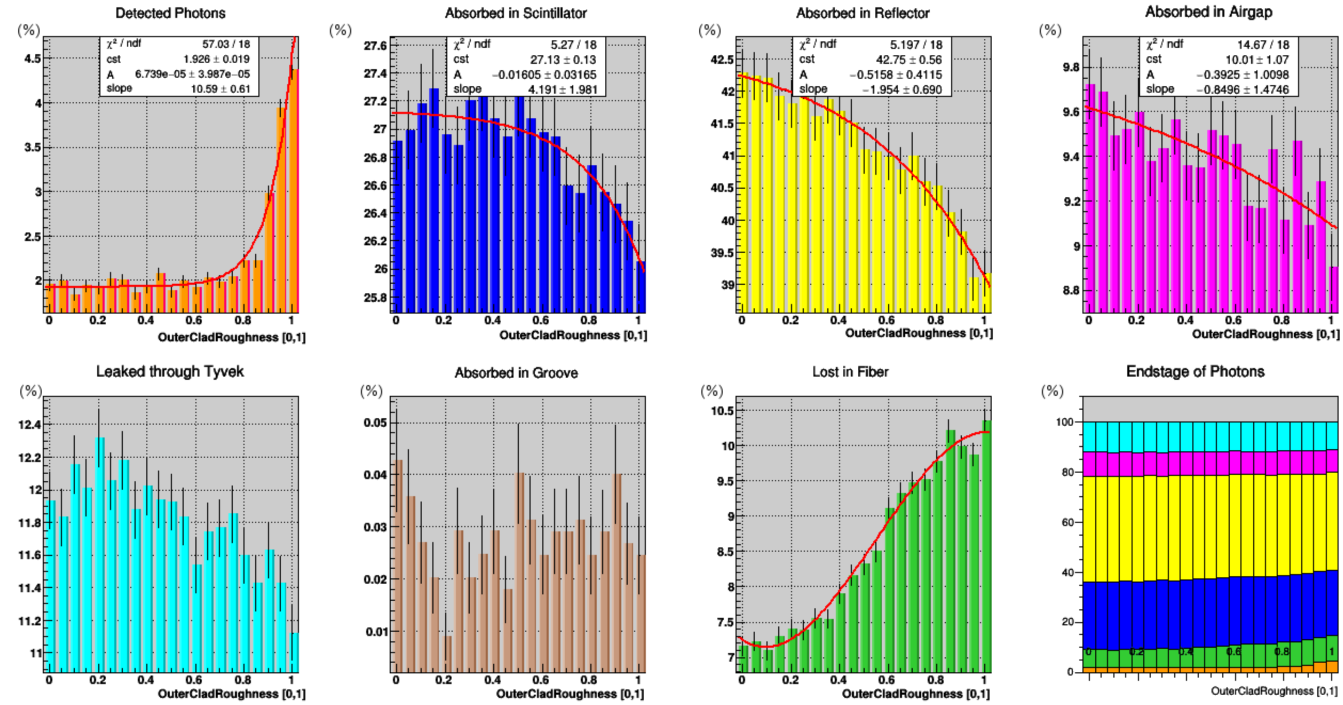

Figure 5.26: destination of the photons that entered the fiber under variation of the roughness of the outer cladding on the fiber.

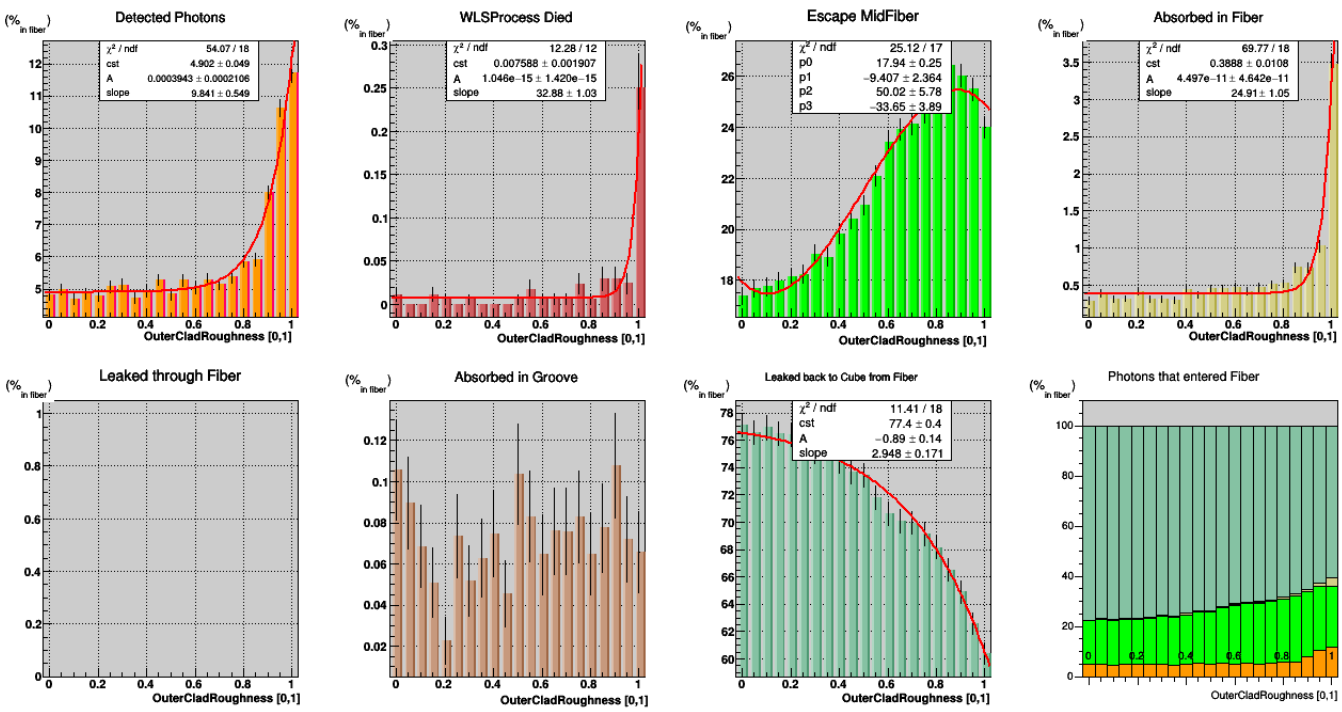

Figure 5.27: destination of the photons that entered the fiber under variation of the roughness of the outer cladding on the fiber.

5.6 TUNING THE PARAMETERS

The influence of the different parameters on the light yield is known from the dissertation in the foregoing section. The parameters can now be adjusted such that the simulated light yield approximates the light yield that is detected experimentally. The results on the experimental light yield can be found in chapter 4.

5.6.1 *The SM1 configuration: experiment vs. simulation*

The SM1 configuration consists of a PVT-cube with edges of 5cm, that is wrapped in a single tyvek layer. A fiber runs through a groove at the upper face of the cube. The fiber is double cladded and two MPPCs are placed at the ends of the fiber (see figure 5.28 for the experimental -and simulation setup).

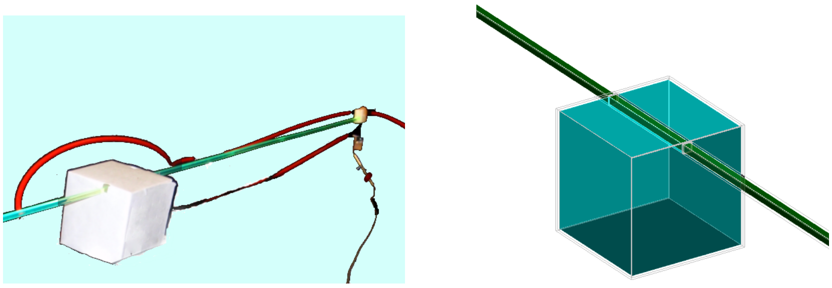

Figure 5.28: SM1 setup of the experiment (left, image: LAL) and SM1 setup of the simulation (right). At the fiberends that are not visible on the image, are also MPPCs.

Experimentally, for an energy deposit of 1MeV in the scintillator cube, the detected light yield was $\#_{exp}$:

$$\#_{exp} = 21,3\ pA. \tag{5.9}$$

An energy deposit of 1MeV corresponds to the generation of 10 000 photons in the cube. An incident photon on the MPPC causes one pixel avalanche. The number of avalanches is increased slightly because of darkcounts (about $+2pA$) and cross talk (about $+17\%$ for the data from LAL). The MPPC has a conversion factor of $\sim 33\%$.

In the **simulation**, 10 000 photons are generated isotropically inside the cube. The number of detected photons is the absolute number of photons that impinge on the MPPC. The MPPC is perfect, i.e. without darkcounts, crosstalk and conversion loss.
Taken these considerations into account, we wish to detect the following number of photons in the simulation, $\#_{sim}^{goal}$:

$$\#_{sim}^{goal} = \frac{21,3 \times 3}{1,17} - 2 = 52,6\ photons \tag{5.10}$$

The multiplication reverses the conversion loss, whereas division has to account for the probability on cross talk, the subtraction eliminates the darkcounts.

5.6.2 *The SM1 configuration: tuning the simulation*

To get an idea of the simulation light yield, a **first test** is simulated with an ideal SM1 configuration. The ideal properties from table 5.6 are used:

Table 5.6: Parameter values for an indicative simulation of the SM1 configuration.

component	parameter	range
cube	size	5 cm
	roughness	0.98
Tyvek	Reflectivity	0.9
	Transmission	0, 05
	Absorption	0, 05
fiber	size	$0,3 \times 0,3 \times 90$ cm^3
	roughness core	1
	thickness inner clad	0, 005 cm
	roughness inner clad	1
	thickness outer clad	0, 005 cm
	roughness outer clad	1
Airgap	thickness	0,1 cm

The simulation with 10 000 generated photons, results in a number of detected photons of

$$\#_{sim}^{test1} = 226,2 \; photons. \tag{5.11}$$

To equal the number of experimentally detected photons, only **23,2%** of this number should be kept. By tuning the parameters, according to the results of section 5.5, photon losses can be introduced.

The only parameters that can accomplish losses for the SM1 configuration are the roughness of the fiber core, the roughness of the outer clad of the fiber and the transmission of the tyvek.

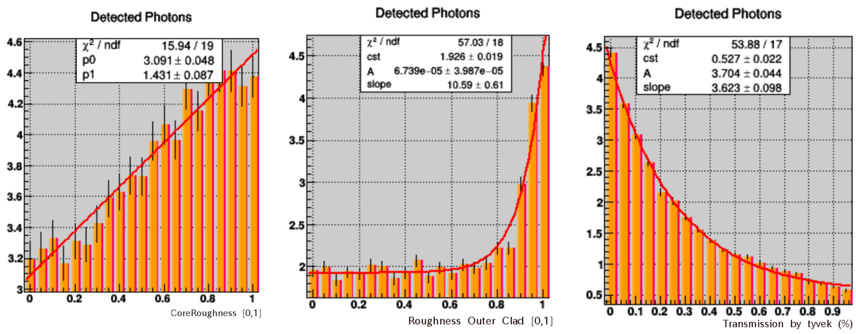

Figure 5.29: Recapitulation of the influences of the roughness of the fiber core (left), roughness of the outer clad (center) and the transmission of the tyvek (right) on the rate of detected photons.

The function fits on the histograms are given below. The ratio of detected photons, R_i, is calculated in function of x_i, which is:

1. x_c is the roughness of the core

$$R_c = 3,01 + 1,43\ x_c \tag{5.12}$$

2. x_{cl} is the roughness of the outer cladding

$$R_{cl} = 1,93 + 0,000067\ e^{(10,6\ x_{cl})} \tag{5.13}$$

3. x_t is the transmission of the tyvek

$$R_t = 0,53 + 3,70\ e^{(-3,62\ x_t)} \tag{5.14}$$

The 'coreroughness', 'outercladroughness' and 'tyvektransmission' have to be chosen such that their combined decreases, with respect to their old values, keep an overall light yield of 23,2%. We wish to obtain the following

$$0,232 = \frac{R_{c,new}}{R_{c,old}} \cdot \frac{R_{cl,new}}{R_{cl,old}} \cdot \frac{R_{t,new}}{R_{t,old}}, \tag{5.15}$$

with R_{ij} the rate of detected photons at a specific value j of the parameter i (see figure 5.29). This gives a minimization problem with three variables, namely x_c, x_{cl} and x_t.

$$\frac{3,01 + 1,43\ x_c}{3,01 + 1,43\ \cdot\ 1} \cdot \frac{1,93 + 0,000067\ e^{(10,6\ x_{cl})}}{1,93 + 0,000067\ e^{(10,6\ \cdot\ 1)}} \cdot \frac{0,53 + 3,70\ e^{(-3,62\ x_t)}}{0,53 + 3,70\ e^{(-3,62\ \cdot\ 0,05)}} - 0,232 = 0$$

$$\Longleftrightarrow \frac{3,01 + 1,43\ x_c}{4,44} \cdot \frac{1,93 + 0,000067\ e^{(10,6\ x_{cl})}}{4,619} \cdot \frac{0,53 + 3,70\ e^{(-3,62\ x_t)}}{3,617} - 0,232 = 0 \tag{5.16}$$

The surface of solutions to this minimization is shown in figure 5.30.

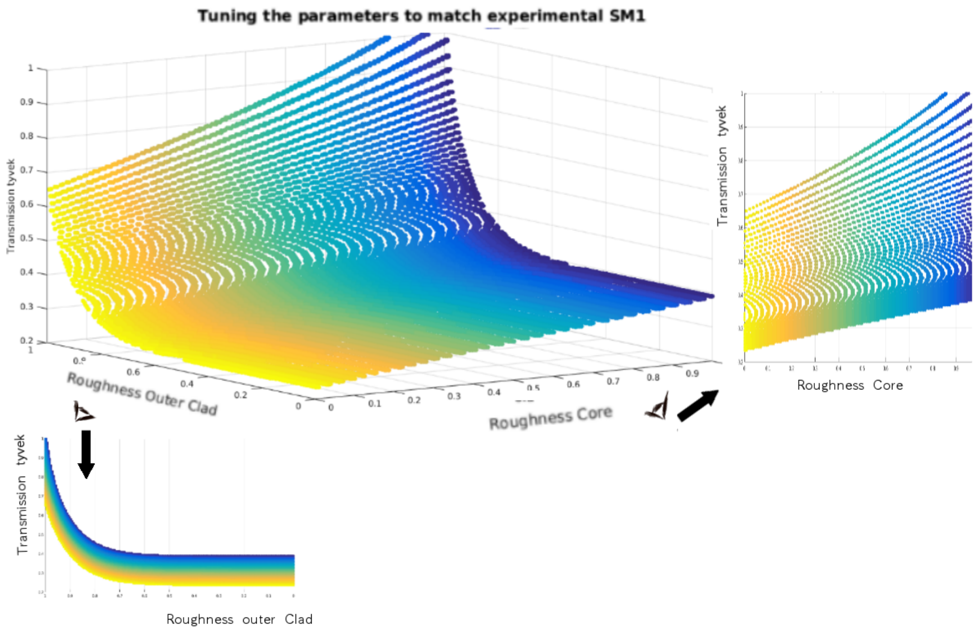

Figure 5.30: Solutions to the minimization problem 5.16, with a tolerance of 0,0005. On the axes are the parameters that can decrease the lightyield.

The tolerance on the solution is 0,0005, so the indicated solutions will result in a relative light yield of $23,2_{\pm 0,0005}\%$. The color of the graph has the sole purpose of giving some depth to the surface. The 2D-projections along two axis are also shown in the figure.
There is a whole set of solutions to get the correct light yield for the SM1 configuration out of the simulation, with respect to the experiment. To narrow the range of the solution, we make use of additional information from the experiment.

5.6.3 *The SM1 configuration: Narrowing the range of the parameters*

Pinpointing the tyvek properties

The experiments from section 4.11 on page 58 show what happens when the number of tyvek layers is increased. The results are repeated as a graph in figure 5.31. The increments between the different light yields are indicated on the figure. Their errors are calculated using the error propagating formula 4.12.

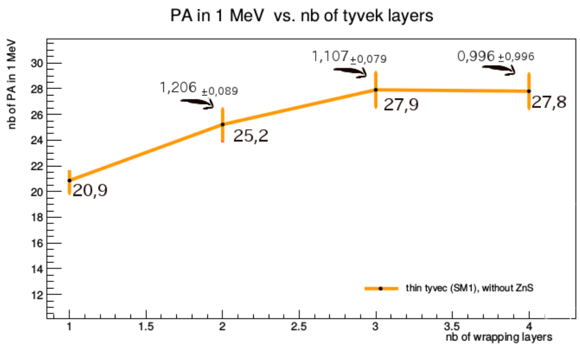

Figure 5.31: Light yield for different number of SM1 tyvek layers. The error bars correponding to the 5% systematic errors. Image: LAL.

With this information, the properties of the tyveklayer can be approximated more accurately.
Simulations are done with different values for the transmittance. For every transmision, the cube is simulated with 1 to 6 tyvek wrappings. The number of detected photons (*det.*) and the relative increase with respect to one tyveklayer less (*inc.*) are shown in table 5.7. An absorption-rate of 1% is taken, as this gave the best results (results for other absorption-rates are shown later).

The *difference* between the increments that were experimentally measured, inc_{exp}, and the increments from the simulation, inc_{sim}, is expressed as

$$difference = \sum_i \sqrt{(inc^i_{sim} - inc^i_{exp})^2}, \tag{5.17}$$

with i an increase for adding a new tyvek layer. The error on the difference is calculated with the error propagation formula 4.12, starting from an error on the detected Number of photons of $s_N = \sqrt{N}$. The measurements show that the tyvek, that corresponds the most with the results from the experiment, has a transmission of **15%**.

Table 5.7: The number of detected photons in function of the number of tyvek sheets and the transmission rate of the tyvek.

$\%_{trans}$ / $\#_{tyvek}$	0,05		0,1		0,15		0,2		0,25		0,3	
	det	inc	det	inc	det	inc	det	inc	det	inc	det	inc
1	216		186		145		126		121		74	
2	229	1,06	221	1,19	163	1,12	159	1,26	129	1,07	143	1,93
3	256	1,12	199	0,90	176	1,08	163	1,03	127	0,98	136	0,95
4	226	0,88	216	1,09	196	1,11	181	1,11	165	1,30	140	1,03
5	246	1,09	27	0,13	185	0,94	181	1,00	137	0,83	130	0,93
6	256	1,04	218	8,07	191	1,03	168	0,93	169	1,23	115	0,89
difference	$0{,}19_{\pm0{,}13}$		$0{,}23_{\pm0{,}12}$		$0{,}14_{\pm0{,}15}$		$0{,}151_{\pm0{,}15}$		$0{,}355_{\pm0{,}17}$		$0{,}744_{\pm0{,}29}$	

These measurement were also done for other values of the absorption. All results are listed in table 5.8. For every pair of transmission and absorption, the *difference* with the experimental measurement is given in the table.

Table 5.8: Differences between the simulated -and measured increases in light yield, for adding tyvek layers, in function of the absorption -and transmision rate.

$\%_{trans}$ / $\%_{abs}$	0,05	0,1	0,15	0,2	0,25	0,3
0	$0{,}07_{\pm0{,}11}$	$0{,}18_{\pm0{,}12}$	$0{,}24_{\pm0{,}15}$	$0{,}21_{\pm0{,}14}$	$0{,}35_{\pm0{,}16}$	$0{,}46_{\pm0{,}23}$
0,0001	$0{,}20_{\pm0{,}15}$	$0{,}19_{\pm0{,}14}$	$0{,}17_{\pm0{,}17}$	$0{,}19_{\pm0{,}16}$	$0{,}32_{\pm0{,}22}$	$0{,}24_{\pm0{,}19}$
0,001	$0{,}29_{\pm0{,}12}$	$0{,}15_{\pm0{,}12}$	$0{,}23_{\pm0{,}16}$	$0{,}29_{\pm0{,}14}$	$0{,}21_{\pm0{,}16}$	$0{,}57_{\pm0{,}26}$
0,01	$0{,}19_{\pm0{,}13}$	$0{,}23_{\pm0{,}12}$	$\mathbf{0{,}14}_{\pm0{,}15}$	$0{,}15_{\pm0{,}15}$	$0{,}36_{\pm0{,}17}$	$0{,}74_{\pm0{,}29}$
0,02	$0{,}22_{\pm0{,}13}$	$0{,}17_{\pm0{,}14}$	$0{,}32_{\pm0{,}18}$	$0{,}21_{\pm0{,}16}$	$0{,}22_{\pm0{,}19}$	$0{,}332_{\pm0{,}15}$
0,03	$0{,}25_{\pm0{,}14}$	$0{,}24_{\pm0{,}14}$	$0{,}31_{\pm0{,}16}$	$0{,}17_{\pm0{,}17}$	$0{,}57_{\pm0{,}25}$	$0{,}10_{\pm0{,}19}$
0,04	$0{,}20_{\pm0{,}15}$	$0{,}19_{\pm0{,}14}$	$0{,}18_{\pm0{,}17}$	$0{,}19_{\pm0{,}17}$	$0{,}32_{\pm0{,}22}$	$0{,}24_{\pm0{,}19}$

The tyvek is known to have splendid optical properties. That is why the transmission -and absorption rate are kept quite low. We see again that the combination of 1% absorption and 15% transmission appoximates the measurements the best. That is, apart from the combination of 0% absorption and 5% transmission. But this is an unrealistic configuration.

Pinpointing the fiber properties

Some specific properties of the cladding of the fiber have been investigated by the laboratory of LAL. They measured the increase in lightyield by going from a single cladded to a double cladded fiber (see section 4.11 on page 58). The results are repeated here in table 5.9.

Table 5.9: Measurements of the light yield for different claddings.

Measurement	PA in 1 MeV
single cladded	$15{,}6_{\pm0{,}8}$
double cladded	$22{,}4_{\pm1{,}1}$
double/single	$1{,}44_{\pm0{,}08}$

There is an improvement of the light yield of about 44% by going from a single -to a double cladded fiber. We wish to obtain the same result from the simulation.

First of all, the SM1 configuration is simulated with a single cladded fiber. The roughness of the cladding is varied over all the values within the GLISURmodel, that is from 0 to 1 (perfectly polished). For every value, 100000 photons are simulated. The obtained light yield can be found in figure 5.32.

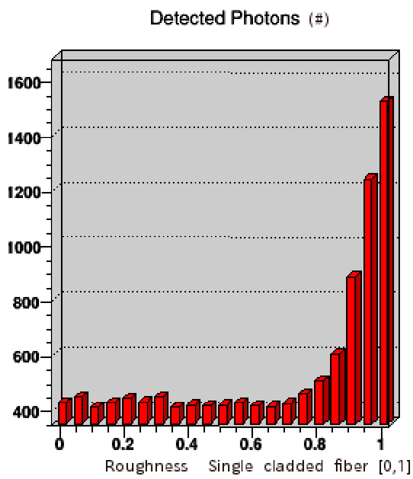

Figure 5.32: The number of detected photons for a SM1 configuration with a single claddded fiber, under variation of the surface roughness.

Subsequently, the SM1 configuration is simulated with a double cladded fiber. The combinations of all possible roughnesses of the inner cladding and the outer cladding are simulated. Again with 100000 photons for every combination. The absolute results for the light yield are shown in figure 5.35

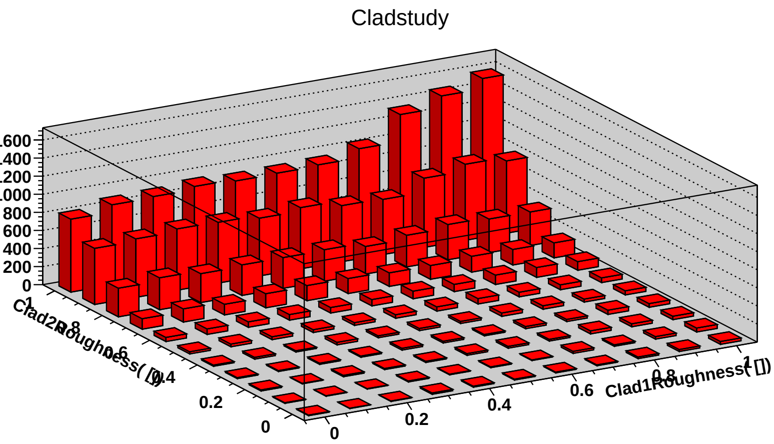

Figure 5.33: The number of detected photons for a SM1 configuration with a double cladded fiber. The roughness of the inner- and the outer cladding are varied against each other.

The ratio of the light yield of the double cladded -versus the single cladded fiber is calculated. Every row of bins, according to a specific value of the roughness of the inner cladding, is divided by the light yield of the single cladded configuration with that specific roughness. The ratios are indicated in figure 5.34.

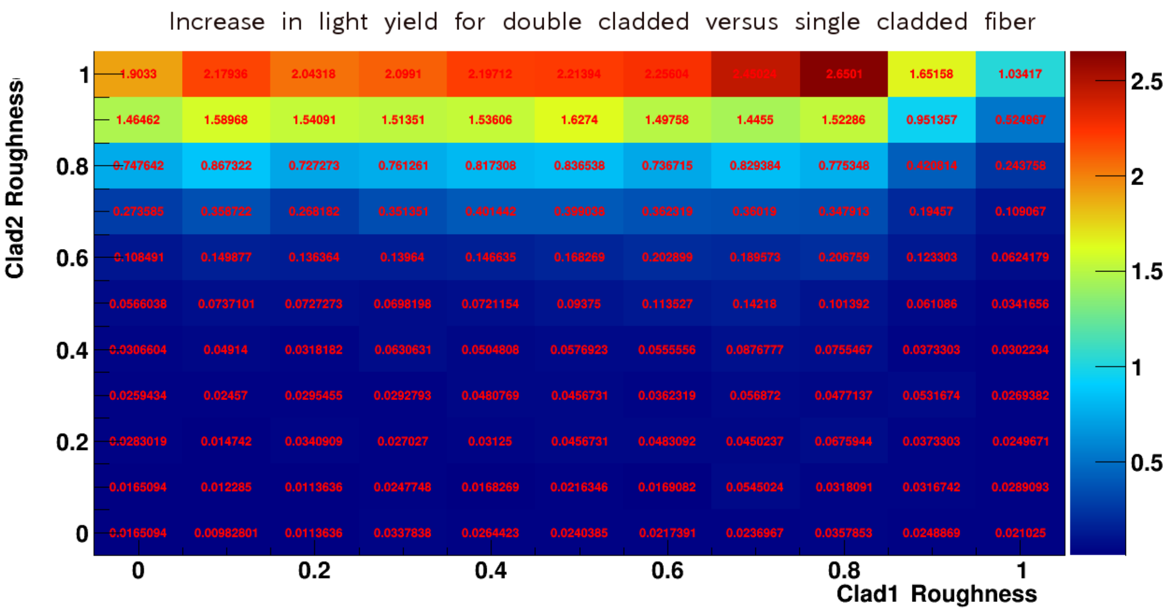

Figure 5.34: The increase in light yield for going from a single cladded fiber to a double cladded fiber, for all combinations of roughnesses for the inner -and outer clad.

The light increase that accords best with the measured values, is found in the second row, where the roughness of the outer cladding is 0,9. We are looking for an increase in light yield of 44%. The configuration with a roughness of the inner -and outer clad of respectively**0,7** and **0,9**, gives the best result with an increase of 44,55%. However, we presume from figure 5.32 that the variations over the roughness of the inner clad from 0 to 0,7 are rather statistical.

5.6.4 *The SM1 configuration: Determination and discussion of the parameters*

With the knowledge from the experiments of the SM1 configuration, the properties of the tyvek wrapping and the fiber claddings were qualified more precisely.

Turning back to the tuning of the parameters in section 5.6.2 on page 94, we can now delimit the range of the solutions for the minimization problem (whose solutions were shown in figure 5.30).
However, during the discussion on the tyvek properties, we found that an absorption rate of 0,01% gave a better result than the absorption rate of 0,05%. The minimization problem is adjusted for this change. The variation of the light yield, R_t under the change of the transmission of the tyvek, x_t is now slightly different, namely

$$R_t = 0,55 + 5,27\ e^{(-5,07\ x_t)}. \tag{5.18}$$

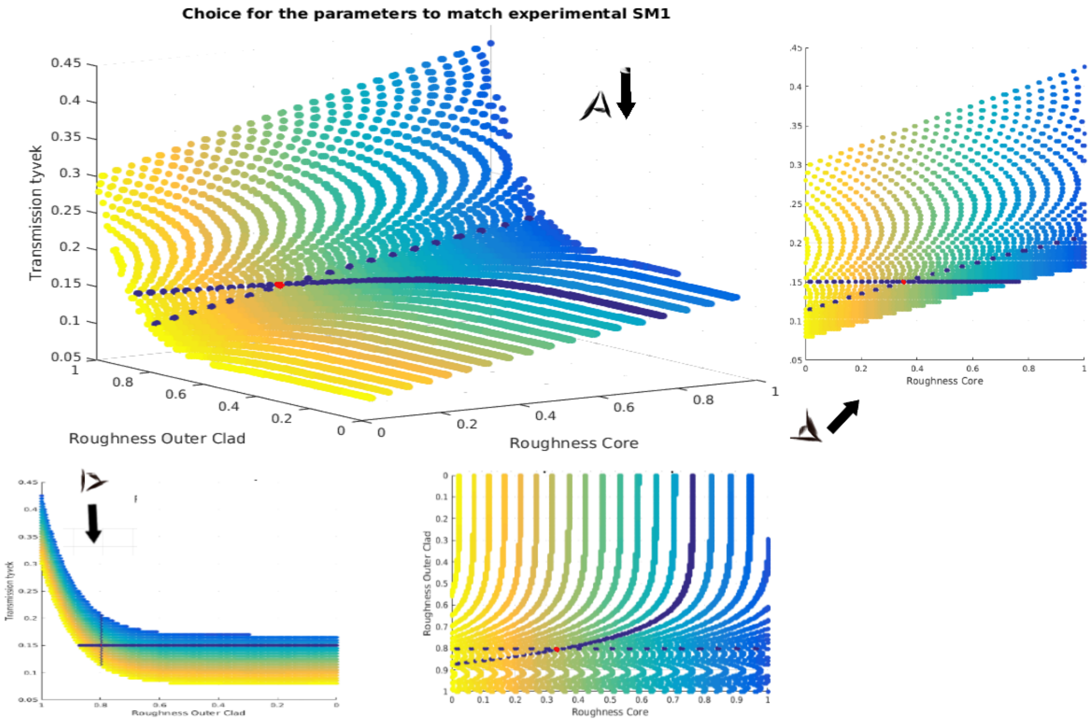

Figure 5.35: Solutions to the minimization problem 5.16, with a tolerance of 0,0005. In blue, the solutions are indicated that are favoured by comparing the simulated data to the experimental data, namely a tyvek transmission rate of 15% and a roughness of the outer cladding of 0,08.

The ranges for the tyvek transmission rate and the roughness of the outer cladding give an exact solution in their intersection. At the intersection, the roughness of the core has a value of $0,35$. Along with the transmission rate of $0,15\%$ and the roughness of the outer clad of $0,8$ this constitutes the solution to the minimization problem.

I would like to stress that it is by no means the objective of this analysis to determine exact material properties for the tyvek and the WLS fiber. The goal of the research is to find values for the simulation parameters, that allow to reconstruct the experimental results from the LAL-laboratories. Henceforth, the simulation can be used to cross check and interpret the experimental results. Moreover, it can make additional predictions for the SoLi∂ experiment.

In the literature, source [54] indicates a transmission rate of $4,9 \pm 0,9\%$ for tyvek (Dupont, 1073B). In source [55] Dupont tyvek of High Opacity was determined to have a transmission rate of $< 0,1\%$. Our value of $0,15\%$ falls indeed in this range. However, seen the high experimental demands for the SoLi∂ detector, a tyvek with good opacity has been chosen. A lower light transmission had been aimed for. In regard to the experiment, we see that the tyvek wrapping does not cover the entire cube. At the edges, and especially at the vertices, of the cube, the light can escape the wrapping through the gaps that were left open by the glueing.

Note that the roughness of the outer clad is slightly lowered, within the margins of its error, to 0.8% in order to get a better solution. At a roughness

of $0,9\%$, the roughness of the core would become very low, almost 0, which is not favourable.
As can be seen in figure 5.35, the roughness of the outer cladding has a major impact on the light yield, independently of the roughness of the inner cladding. This is supported by the experiences from the experiments. Touching the fiber creates spots where the photons have the opportunity to escape the fiber. The fibers have to be handled with the utmost care to achieve the best light yield. This is also the reason of applying the double cladding to the fiber; it postpones the risk of contamination to the second boundary that the photon encounters.

Furthermore, note that there can also be other ways to loose a fraction of the light. Ways that aren't parametrized in the current simulation. Turning the efficiency of those parameters down, could for example improve the performance of the tyvek.

5.6.5 *Cross check on the SM1 configuration*

The simulated light yield for the SM1 configuration is tested with the parameters that were found in the previous section and that are repeated in table 5.10.

Table 5.10: Simulation parameters as determined with experimental measurements of the tyvek and the fiber cladding.

component	parameter	range
cube	size	5 cm
	roughness	$0,98$
Tyvek	Reflectivity	$0,84$
	Transmission	$0,15$
	Absorption	$0,01$
fiber	size	$0,3 \times 0,3 \times 90$ cm^3
	roughness core	0.35
	thickness inner clad	$0,005$ cm
	roughness inner clad	$0,8$
	thickness outer clad	$0,005$ cm
	roughness outer clad	$0,8$
Airgap	thickness	0,1 cm

With these setting, $53,0$ photons were detected in the simulation. This is close to value that was aimed for of $52,6$ photons (see equation 5.10).

The roughness of the fiber core is rather low. It can be increased at the expense of the tyvek or the roughness of the outer clad. Additional cross checks with the experiment could tell us more about the properties. In addition, the other parameters, that induce an increase in the light yield, could be altered as well. In that case, the parameters that can decrease the light yield will get worse to meet the experimental results.

CONCLUSION

A highly efficient and finely segmented neutrino detector, known as the SoLi∂ detector, is momentarily under construction, to be installed near the Belgian BR2 research reactor. It will investigate the anomalous results concerning the neutrino oscillations. The experiment will probe the short-baseline regime, i.e. at close proximity (5-10m) to the reactor core, which previous experiments could not cover.

The deployment of the SoLi∂ detector requires an extensive knowledge of the different components in the production-, interaction- and detection chain of the neutrinos. To this end, an experimental testbench was constructed and a full simulation framework was developed. This Master's thesis is dedicated to the optical aspect of the detection mechanism.

The experimental proceedings and observations are elaborated in chapter 4. A unit cell of the SoLi∂ detector, consisting of a scintillator cube in a reflective wrapping, a wavelength shifting fiber and a photodetector were investigated. Comparative measurements for different wrappings, polishings, fibers, etc. were performed. The results are listed in table 4.3 and in the tables on pages 60-61. In particular, we found a distinct increase in light yield, of about $40_{\pm 10}\%$, when using a thick tyvek. Also, extra cladlayers on the fiber with a lower refractive index, to improve the internal reflections, proved themselves very useful. A double cladded fiber improved the light yield with $40_{\pm 8}\%$.

During the construction and testing of the experimental setup, we observed that the separate components do not add much to the noise (see section 4.2). The noise increased from $0,36$mV (only electronics board and oscilloscope) to $0,50$mV (full setup), which is an increase of 39%. Connecting a cable of $3,5$m between the electronics and the MPPC, adds another 33% to the noise. The latter has to be done for the SoLi∂ detector, to transport the signals from the 3200 MPPCs to the electronic processor.
The dark counts and cross talk in the MPPC were also investigated, in section 4.3. It is not possible to eliminate the dark counts by statistical means. In order to achieve single photon sensitivity, the SoLi∂ detector will be cooled down to avoid thermal agitation that induces dark counts.

In the scope of this Master's thesis, the simulation of the photon transport -and detection was constructed as well. The simulation reconstructs the trajectory of the photons, from the production site in a scintillator cube, until its point of detection or elimination.
The first step in the approach was to implement the detector geometry and the necessary physical processes within the framework of the GEANT4 library. The setup was implemented with a flexible design; by means of several parameters the design can be adjusted to the specific needs of the user, within the range of the predetermined constraints. The optical components -and boundaries were studied closely in section 3.1 and their properties were incorporated in the simulation, in section 5.2-5.4.
The relative influences of the parameters on the light yield were investigated. The results are displayed in section 5.5. The parameter variations induced relative changes in the destiny of the photons, that could be explained in terms of the physical properties.

With the knowledge of the influence of the parameters, the light yield of the experiment was approximated. The transmittance of the tyvek, the roughness of the fiber core and the roughness of the outer cladding can be used to decrease the light yield to meet the experimental results. A three dimensional minimization problem was performed, specified by the information that could be extracted from the experiments. In the end, a transmission rate of $0,15_{\pm 5}\%$ for the tyvek and a roughness for the core and the outer clad of respectively $0,35_{+20}$ and $0,8_{\pm 20}$ were found to approximate the experimental demands the best. This result is discussed in more detail in section 5.6.4.

Now that the optical simulation is on point and I am able to work with the simulation and the GEANT4 library more fluently, I want to extract the full potential of it. First of all I want to turn on and fine tune the scintillation processes and generate a particle source that can trigger the scintillation process. The ZnS sheets are implemented in the current simulation as well, but they still need some adaptation. Once this has done, I want to connect the optical simulation to the full simulation chain of the SoLi∂ detector. The simulation chain already incorporates the neutron detection and the signal processing.
The optical simulation has the disadvantage of being dependent on many parameters and processes. Elaborate cross checks with experimental results are in order. The full software framework will allow to interpret and adjust the SoLi∂ detector to obtain its maximal capacitance.

BIBLIOGRAPHY

[1] J. Beringer et al., "Review of Particle Physics". Physics Review D86 (2012).

[2] M. Gell-Mann, P. Ramond, and R. Slansky in Sanibel Talk (1979) and Yanagida during the proceedings of the Workshop on Unified Theory and Baryon Number of the Universe, KEK, Japan (1979)

[3] W. Pauli, "Open letter to the group of radioactive people at the Gauverein meeting in Tbingen" (1930)

[4] J. Chadwick, "The Intensity Distribution in Magnetic Spectrum of β-Rays of Radium", Verhandlungen der Deutschen Physikalischen Gesellschaft 16 (1914)

[5] E. Fermi, "Tentativo di una teoria dei raggi ", La Ricerca Scientifica 2 12 (1933)

[6] W. Yao et al., "Review of Particle Physics: Quarks", Journal of Physics G 33 (2006)

[7] Georgia State University, "Coupling Constants for the Fundamental Forces", HyperPhysics (2011)

[8] C. Cowan, F. Reines et al., "Detection of the Free Neutrino: A Confirmation", Science 124 (1956)

[9] Y. Fukuda et al. (Super-Kamiokande Collaboration), "Evidence for Oscillation of Atmospheric Neutrinos", Physics Review Letters 81 (1998)

[10] Q. Ahmad et al. (SNO Collaboration), "Measurement of the Rate of $\nu_e + d \to p + p + e$ Interactions Produced by ^{8}B Solar Neutrinos at the Sudbury Neutrino Observatory", Physics Review Letters 87 (2001)

[11] E. Konopinski and H. Mahmoud, "The universal Fermi interaction", Physics Review 92 (1953)

[12] M. Goldhaber, L. Grodzins and A.W. Sunyar, "Helicity of neutrinos", Phyics Review 109 (1958)

[13] P. Ade et al, "Planck 2013 results. XVI. Cosmological parameters", Astronomy and Astrophysics 571 (2014)

[14] B. Cleveland et al, "Measurement of the Solar Electron Neutrino Flux with the Homestake Chlorine Detector", Astrophysical Journal 496 (1998)

[15] B. Pontecorvo, "Inverse beta processes and nonconservation of lepton charge", Journal of Experimental and Theoretical Physics 34 (1957)

[16] Z. Maki, M. Nakagawa, S. Sakata, "Remarks on the Unified Model of Elementary Particles", Progress of Theoretical Physics 28 (1962)

[17] M. Doi et al , "CP violation in majorana neutrinos", Physics Letters B102 (1981)

[18] V. Gribov and B. Pontecorvo, "Neutrino astronomy and lepton charge", Physics Letters B28 (1969)

[19] Kearns, Kajita, Totsuka, "Detecting Massive Neutrinos", Scientific American (1999)

[20] A. McDonald, J. Klein, D. Wark, "Solving the Solar Neutrino Problem", Scientific American 288 (2003)

[21] S. Bravo, "First observation of high-energy neutrino oscillations by DeepCore and IceCube", Physical Review Letters (2013)

[22] J. Conrad, "Neutrino Experiments", lectures Columbia University (2008)

[23] J. Formaggio, G. Zeller, "From eV to EeV: Neutrino Cross Sections Across Energy Scales", Review of Modern Physics 84 (2012)

[24] M. Kos, "Method of fission product beta spectra measurements for predicting reactor anti-neutrino emission", Nuclear Instruments and Methods in Physics Research V776 (2015)

[25] G. Vidyakin et al., "Limitations on the characteristics of neutrino oscillations", JETP Letters 59 (1994)

[26] M. Apollonio et al. (Double Chooz Collaboration), "Limits on neutrino oscillations from the CHOOZ experiment" Physics Letters B466 (1999)

[27] A. Gando et al. (KamLAND Collaboration), "Constraints on θ_{13} from a three-flavor oscillation analysis of reactor antineutrinos at KamLAND" Physical Review D83 (2011)

[28] G. Mention et al., "Reactor antineutrino anomaly", Physical Review D83 (2011)

[29] J. Abdurashitov et al. (The SAGE Collaboration), "Measurement of the response of a gallium metal solar neutrino experiment to neutrinos from a $^{5}1Cr$ source", Physysical Review C59 (1999)

[30] W. Hampel et al., "Final results of the $^{5}1Cr$ neutrino source experiments in GALLEX", Physics Letters B420 (1998)

[31] C. Giunti and M. Laveder, "Statistical significance of the gallium anomaly", Physical Review C83 (2011)

[32] R. Battye and A. Moss, "Evidence for Massive Neutrinos from Cosmic Microwave Background and Lensing Observations", physical review letters 112 (2014)

[33] A. Vacheret et al., "A novel solid segmented scintillator antineutrino detector", draft manuscript (2016)

[34] F. Yermia et al., "SoLi∂ - Search for Neutrino Oscillation with Lithium-6 Detector", application pour ANR (2015)

[35] K. Nakamura et al., "Review of Particle Physics", Journal of Physics G37 (2010)

[36] G. Knoll, "Radiation Detection and Measurement", Wiley & Sons (2000)

[37] J.Birks, D. Fry, L. Costrell, K. Kandiah, "The theory and practice of scintillation counting", Pergamon Press (1964)

[38] Saint-Gobain Crystals, "Organic scintillation materials" (2015)

[39] Kirchhof Institut f*ü*r Physik, "Scintillation Detectors, Particle Detection via Luminescence" (2011)

[40] Eljen Technology, "EJ-426 thermal neutron detector sheet" (2012)

[41] "Nuclear Instruments and Methods in Physics Research", Section A. Volume 550 (2005)

[42] E. Siciliano et al., "Comparison of PVT and NaI(Tl) scintillators for vehicle portal monitor applications", (2005)

[43] L. Nozka, "BRDF profile of Tyvek and its implementation in the GEANT4 simulation toolkit", optics express 4209 19 5 (2011)

[44] J. Stover, "Optical scattering : measurement and analysis", SPIE Press (1995)

[45] Saint-Gobain Crystals, "Scintillation products: scintillating optical fibers" (2011)

[46] hamamatsu photonics, "Technical Information MPPC and MPPC modules" (2013)

[47] B. Aull et al., "Geiger-Mode Avalanche Photodiodes for Three-Dimensional Imaging", Lincoln Laboratory Journal (2002)

[48] G. Barbarino et al., "Silicon Photo Multipliers Detectors Operating in Geiger Regime", INTECH Open Access Publisher (2011)

[49] hamamatsu photonics k.k., "MPPC(R) (multi-pixel photon counter)", Catalogue KAPD1043E03 (2013)

[50] D. Boursette and M. Bongrand, "Light yield studies with LAL test bench", (2016)

[51] J. Allison, "Geant4 - a simulation toolkit", Elsevier Science(2003)

[52] K. Kleinknecht., "Detektoren f˙· ur Teilchenstrahlung", Teubner Verlag, (2005)

[53] A. Levin and C. Moisan, "A More Physical Approach to Model the Surface Treatment of Scintillation Counters and its Implementation into DETECT, TRIUMF" Preprint TRI-PP-96-64 (1996)

[54] A. Chavarria, "A study on the transmittivity of Tyvek" Duke University (2005)

[55] DuPont, "Tyvek Vivia High Opacity" (2012)